AN OBSERVATIONAL STUDY OF SLOPE AIR AND FREE AIR WINTERTIME TEMPERATURES IN WHISTLER VALLEY, BRITISH COLUMBIA, CANADA

by

Lisa N. Erven

B.Sc., University of Waterloo, 2008

A THESIS SUBMITTED IN PARTIAL FULFILLMENT OF
THE REQUIREMENTS FOR THE DEGREE OF

MASTER OF SCIENCE

in

THE FACULTY OF GRADUATE STUDIES

(Atmospheric Science)

THE UNIVERSITY OF BRITISH COLUMBIA

(Vancouver)

June 2012

Abstract

Temperature structure within complex terrain is fundamental to determining stability, thermally-induced circulations, and mountain weather, all of which impact those living, working, and recreating within it, as well as those external to it that depend on water from snowmelt. While numerous studies and text books outline many factors affecting slope air and free air temperatures, the interactions of these factors with the complex terrain makes predictability of temperature structures very difficult. This is further compounded by sparse observational data that has limited representativeness due to numerous localized effects. In preparation for the 2010 Olympic and Paralympic Winter Games, temperature sensors were placed along the west slope of Whistler Mountain, and radiosondes were launched twice daily, creating a rare opportunity to investigate slope and free air temperature structure and evolution within a mountain valley.

Daytime and nighttime temperature profiles are categorized by cloud cover, and very consistent lapse rates are found within categories. Profiles are compared for slope and free air within each category, and between categories. Case studies provide further detail in describing temperature structure evolution. Clear days give rise to the least uniform slope air temperature structure, but a consistent, fairly representative, linear lapse rate is nonetheless found. Overcast conditions effectively eliminate microclimates, producing a relatively linear slope air temperature structure. Additionally, consistent free air lapse rates are defined for each cloud cover category. While the majority of slope and free air lapse rates are statistically indistinguishable, significant slope-free air temperature differences still exist.

Lastly, linear regression is used to develop an equation that successfully determines slope air temperatures from a given free air temperature, or vice versa. Together with the representative lapse rates, one is able to construct slope and free air temperature profiles given a single slope or free air temperature measurement. These results show that by separating profiles by weather condition, consistent temperature structures and relations can be extracted from a seemingly incoherent collection of complex mountain slope and free air profiles. In doing this, it becomes feasible to accurately predict these profiles, providing great utility to those impacted by mountain temperatures.

Table of Contents

List of Tables

List of Figures

Acknowledgements

When enrolling at The University of British Columbia I was determined to be involved in Olympic forecasting research and I have my supervisor, Dr. Ian McKendry, to thank for encouraging me to pursue a project that I was passionate about. Additionally, Ian supported my participation in numerous conferences across Canada and the United States. Dr. Ian Okabe also played a key role in my Olympic research endeavours by sponsoring me as a Visiting Scientist at the Vancouver Weather Office and guiding me through the bureaucracy of joining the Olympic forecasting services. Being part of an event that filled Canadians with pride and brought people from all different nationalities together to cheer on their favourite athletes is a memory I will cherish forever.

My involvement in the forecasting operations of the Vancouver 2010 Olympic and Paralympic Winter Games gave me the opportunity to work alongside many talented scientists and forecasters including SNOW-V10. A special thank you goes to George Isaac and to the members of SNOW-V10 for sharing data from the Automated Olympic Network weather stations and Whistler Valley radiosondes. Paul Joe encouraged my participation in numerous workshops and produced multiple 3-D maps of my study area. The helpful discussions on local mountain effects with Mark Barton were invaluable. Ivan Heckman provided technical support and ensured that I obtained all Environment Canada weather data as needed.

There are many individuals at the Vancouver Weather Office who contributed to the success of my research, including Chris Doyle, who graciously offered me the use of the Visiting Scientist room during my years of study. Brad Snyder and Trevor Smith enabled me to access satellite and web cam imagery for use in this thesis and provided assistance in acquiring such data.

This document has undergone much improvement thanks to the thoughtful critiques of my committee members, Dr. Ian Okabe and Dr. Douw Steyn, and external examiner, Dr. Roland Stull. I am also indebted to Dr. Dan Moore for providing the initial programming code and for spending considerable time helping me overcome the steep learning curve of R Statistics.

Many thanks are owed to Whistler Blackcomb Mountain operations manager, Doug MacFarlane, ski lift maintenance manager, Wayne Wiltsie, and the staff at Whistler Blackcomb for permitting temperature sensors to be installed along the west slope of Whistler Mountain. Wayne also provided transportation up and down the mountain during the off-seasons. I thank Bill Scott, Drew Pawley and Robert Reed of Environment Canada for allowing UBC temperature sensors to be temporarily mounted on the VOA operational weather station for calibration purposes.

My field work would not have gone as smoothly if it wasn't for my field assistant, John Gallagher, who was an integral part of installation, maintenance, and dismantling. Together, we braved the slopes of Whistler in a variety of weather conditions and kept the temperature sensors operating at their finest.

This research could not have been completed without funding from The Natural Science and Engineering Research Council of Canada (NSERC) Discovery Grant, which covered the cost of instrumentation, ski lift tickets to access field sites, and numerous conferences. Additionally, an NSERC Postgraduate scholarship provided financial support during my program. Both the

To my family and friends,

for their endless support and encouragement

Chapter 1

Introduction

Mountain weather is determined by the intricate juxtaposition of synoptic-scale ambient conditions and local variations from terrain and surface characteristics (Barry, 2008; Whiteman, 2000). The resulting temperature structure along mountain slopes and within the free air (FA, defined here as the column of air over the centre of the valley as observed by radiosonde ascent) is accordingly complex. Slope air (SA) undergoes radiative and turbulent heat exchanges with the mountainside, producing horizontal temperature gradients between SA and adjacent FA. Thermally-induced circulations arise from these temperature gradients producing irregular precipitation distributions and phase transitions (Whiteman, 2000), challenges that operational forecasters deal with daily.

It can be argued that establishing a more accurate description of temperature patterns in complex terrain remains the single most important meteorological aspect of mountain climate research (Barry, 2008), and has a wide range of societal applications. For example, air temperature is highly correlated to avalanche activity and is a primary factor in snowpack evolution (Baggi and Schweizer, 2008; McClung and Schaerer, 2006). Additionally, with 40% of the world's population dependent upon watersheds of rivers fed by mountains, accurate temperature values for input into snowmelt models are crucial for resource management (Barnett et al., 2005). Alpine temperatures have been previously estimated using the standard atmospheric lapse rate (Martinec and Rango, 1986), or a historically derived lapse rate for a given area (Daly et al., 2002). None of these approaches account for daily fluctuations in vertical structure (Lundquist and Cayan, 2007).

In British Columbia, understanding SA temperature structure and its connection to the FA has significant implications for the numerous ski areas including Whistler Blackcomb, the largest ski resort in North America, and the surrounding Coast Mountains which are heavily used for a variety of recreational activities. Specifically, this could improve prediction of low-level vertical temperature structure, and precipitation type. Moreover, hydroelectricity makes up over 90% of

BC Hydro power generation with its operations extending to the Cheakamus watershed which Whistler lies within (BC Hydro, 2012). Accurate lapse rates for input into their snowmelt model have the potential to minimize errors caused by the currently parameterized lapse rates (Quick and Pipes, 1977).

Unfortunately, temperature measurements in complex terrain are subject to a myriad of local influences making temperature structure difficult to study. Recent technological advances, such as the development of inexpensive temperature sensors and data loggers (Whiteman et al., 2000), have eased the cost of creating spatially-dense data collection networks; the benefit of which allows sites dominated by microclimates to be filtered or averaged out. They have also essentially eliminated the issue of non-concurrent observations (e.g., Wagner, 1930; Samson, 1965). However, field experiments with co-located SA-FA measurements are still rare. The remainder of this chapter first looks at factors influencing SA and FA temperature, then overviews past methods used to estimate their altitudinal variation, and lastly concludes with a description of the research objectives.

1.1 Factors Affecting SA and FA Temperature

The work of de Saussure (1779-96) is considered to be the earliest research to explain temperature minima in the mountains, and the diurnal variation of lapse rates (summarized in Carozzi and Newman [1995]), garnering him the title as the first mountain meteorologist. However, it was not until the twentieth century that intensive observational work revealed temperature differences between summits (measured by weather stations) and the summit-level FA (measured by sondes carried aloft by balloons or kites) (Schmauss, 1907; Hildebrandt, 1912; Ficker, 1913; Hann, 1913; Whiteman and Dreiseitl, 1984; Barry, 2008). Statistical analyses by Peppler (1931), Schell (1934), and Ekhart (1939) established systematic temperature differences, and, as an extension of their work, Wagner (1938), Ekhart (1944, 1948), and Defant (1949) theorized the processes of differential heating of near-surface air masses, and the resulting circulation systems of slopes and valleys. This formed the basis of our current understanding of temperature patterns in mountainous regions (Richner and Philips, 1984).

Additionally, their work pioneered the effects of cloud cover, vegetation, topography, season, and snow cover on SA temperatures, and the subsequent heat transfer to the FA.

Insolation is responsible for driving almost all meteorological processes on Earth, one of which is the heating of SA. During daytime, incoming shortwave radiation warms mountain slopes (Aguado and Burt, 2003; Mahrt, 2006). This energy is then transferred by conduction to a thin layer of near-surface air. Convective processes subsequently direct this more buoyant air away from the surface, warming the FA (Ahrens, 1994). Insolation increases with altitude as there is less atmospheric absorption and backscatter (ACIA, 2005). Based on this alone, one would expect that summits experience a higher daytime maximum temperature in comparison to lower elevations. However, increased insolation received near mountain peaks has little effect on air temperature (Whiteman, 2000). Instead the reduced land surface area at higher elevations leads to less heat transferred to the atmosphere during the day, and thus the diurnal temperature cycle amplitude decreases with altitude (Whiteman, 2000).

As the sun dips below the horizon, radiative cooling occurs when outgoing longwave radiation starts to exceed the incoming shortwave radiation. Once the surface is colder than the adjacent air, energy transfers to the ground by conduction, and thus the bottom layers of air become cooler than the air a few metres above (Ahrens, 1994). Snow, a better longwave emitter than bare ground, enhances radiative cooling (Wilber et al., 1999). When this occurs on dry, cloud-free, calm nights, a strong nocturnal radiative inversion can form (Ahrens, 1994). In the FA above the inversion, a neutral or weakly stable layer exists, left over from the previous day's mixed layer (Oke, 1978).

Slope angle and aspect are both fundamental to determining the amount of intercepted radiation and the associated localized mountain climate (Chapman, 1952; Barry, 2008). The most noticeable differences occur between shade-dominated north-facing slopes, and sun-exposed south-facing slopes in the Northern Hemisphere. Barry and Chorley (1987) show that for mountainous terrain in Trier, West Germany (50°N), the intensity of direct insolation increases as slope angle increases on south-facing slopes during wintertime, whereas the opposite is true for north-facing slopes. The contrast is large, decreasing from approximately 800 W m^{-2} on south-facing slopes, to 200 W m^{-2} on north-facing slopes (Barry and Chorley, 1987). Whiteman

(2000) illustrates similar findings at 40°N, showing similar insolation maxima occurring in the morning on east-facing slopes, and in the afternoon for west-facing slopes. Both aspects show an increase in radiation intensity with slope angle.

As with slope aspect and angle, shading caused by topographical projections significantly modifies the instantaneous and daily total radiation received by a surface (Muller and Scherer, 2005; Whiteman et al., 1989). Microclimatic differences can be produced over very short distances, with higher temperatures on sunny slopes and lower temperatures on slopes shaded by terrain (Whiteman, 2000; Howard and Stull, 2011). Colbeck (1994), for example, observed a 4°C temperature difference between sunny and shaded snow-covered surfaces. Additionally, shading can have secondary effects, such as delaying local sunrise, which can then delay the development of upslope flows and the break-up of inversion layers (Whiteman, 2000). Topographic shading effects are more significant for north-south oriented valleys than east-west (Colette et al., 2003).

Albedo is the fraction of incoming short-wave radiation that is reflected by a surface (Stull, 1988), and typically ranges from 0.5 to 0.98 for snow-covered surfaces (ACIA, 2005). New, dry snow has the highest albedo values of 0.9 to 0.98 (Grenfell et al., 1994). As snow ages, its grain size increases, regardless if melting has occurred, causing a reduction in albedo over time (Wiscombe and Warren, 1980). Albedo of snow also changes with angle of incidence (based on solar zenith and slope angle), and with physical changes in the state of the snow which occur if conditions conducive to melting are present (Oke, 1978). Higher albedos occur during the early morning and evening when the surface is frozen and zenith angles are high. In the afternoon, production of a thin film of melt water on the snow surface can reduce the albedo to a value close to that of water (Oke, 1978). Any decrease in albedo increases the amount of energy absorbed at the surface, thereby enhancing the heating of SA.

During the daytime, SA becomes warmer than FA over the centre of a valley, and buoyancy drives upslope flow (Oke, 1978). As air from the bottom and sides of the valley is removed, compensatory subsidence occurs over the centre of the valley. This adiabatically warms the FA, effectively distributing the energy absorbed by the slope throughout the entire valley atmosphere (Whiteman, 2000). As the temperature of the valley atmosphere increases throughout the day,

the mixed layer deepens (Whiteman, 2000). At night, radiative surface cooling results in SA becoming cooler than the FA at the same elevation (Whiteman, 2000). This colder, negatively buoyant air can then drain down slope through cold air drainage, collect in the valley below, and further contribute to the formation of a temperature inversion. Commonly seen in mountainous terrain, inversions can appear at night or at all times during the day over a snow-covered surface. Additionally, this cold air can drain down the gently-sloping valley floor in a process known as down-valley drainage (De Wekker and Whiteman, 2005). Removal of air from the valley bottom allows for compensatory subsidence from aloft. This adiabatic warming can decelerate the cooling of the FA within the valley (De Wekker and Whiteman, 2005; Whiteman et al., 2004).

Diurnal temperature cycles and associated valley circulations that occur under quiescent conditions can be disrupted by synoptic systems (Oke, 1978). While these systems and their associated cloud cover, wind, and temperature advection are partially responsible for spatial and temporal changes in SA and FA temperatures (Lundquist and Cayan, 2007), valleys with steeper slopes are more protected from the overlying ambient flow (Mahrt, 2006). Under certain conditions, strong, synoptic-scale influences dominate local valley effects, resulting in close agreement between SA and FA temperature profiles, and even distant radiosondes. Conversely, there are situations in which the local valley processes dominate weaker synoptic-scale effects resulting in dramatically different SA and FA profiles. Examples of both are illustrated using Whistler-specific data and surrounding radiosondes (Fig. 1.1). In Fig. 1.1a, similar lapse rates are found in all profiles despite the >100 km distances between the four radiosonde launch sites. Alternatively, Fig. 1.1b shows dramatic differences in lapse rates for the same four profiles.
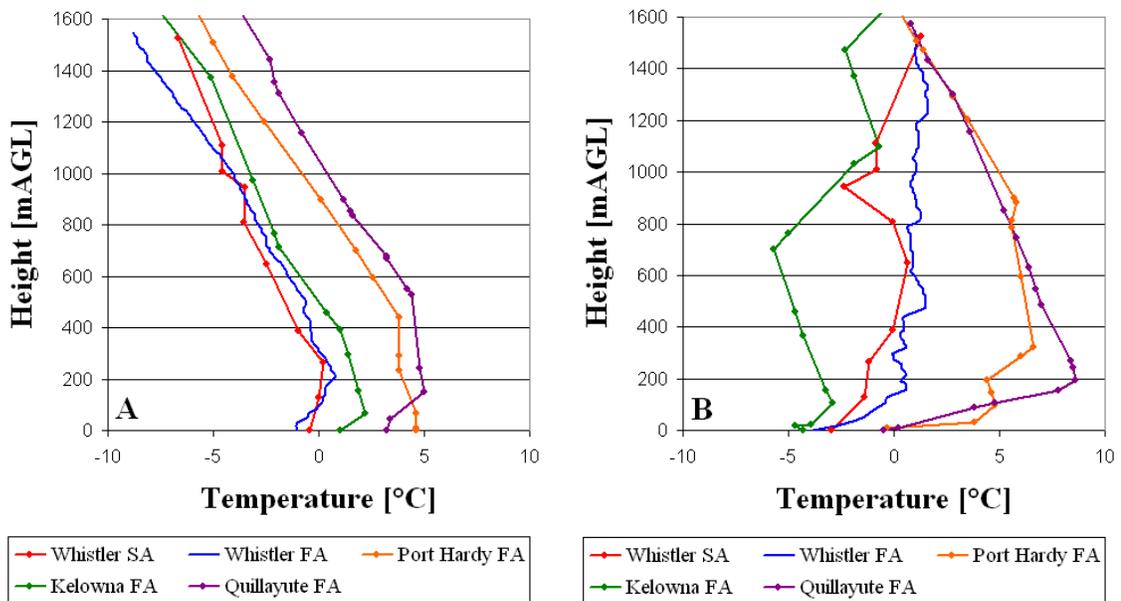
Figure 1.1: Example temperature profiles of Whistler Valley (SA and FA), and FA temperature data from nearby radiosondes illustrating a) agreement between profiles for 1515 PST 10 Mar 2010, and b) dramatic differences at 0315 PST 22 Feb 2010. In both cases, profiles have been plotted in metres above ground level.

Locally, wind strongly influences the relation between SA and adjacent FA temperature profiles. Strong winds flowing perpendicular to the mountain chain can "flush" away the modified mountainside boundary layer air, which increases the flux of moisture and heat away from the surface, preventing large SA-FA temperature differences from forming (Barry, 2008; Ahrens, 1982). In a comparison of summit-level SA and FA temperatures, Richner and Philips (1984) demonstrated that maximum daytime SA-FA temperature differences were markedly reduced as wind speed increased. Alternatively, light winds associated with weak pressure gradients and/or high pressure, provide optimal conditions for the development of large temperature differences between the SA and FA (Barry, 2008).

Significant modification of Earth's energy budget is caused by cloud cover (Stull, 1992). Clouds predominantly exert two competing daytime affects on surface temperatures: 1) they reflect a significant portion of insolation before it reaches the ground (Freedman et al., 2001), and 2) they absorb outgoing longwave radiation and emit radiation back towards the surface (Liou, 2002). At night, this latter process significantly reduces radiative cooling at the surface, inhibiting the formation of surface-based inversions (Barry and Chorley, 1992). The net contribution (positive or negative) of clouds depends on their horizontal extent, elevation, time of day, thermodynamic phase, liquid/ice content, and particle size distribution (Liou, 2002).

Aside from the aforementioned effects, there are also seasonal considerations. Decreased daylight hours in winter mean shorter periods of shortwave radiation absorption. Additionally, the tilt of the Earth away from the sun causes insolation to pass through a larger portion of the atmosphere with greater chance of being absorbed or scattered (Ahrens, 1994). Winter nights allow for longer periods of radiative cooling, providing the best conditions for strong surface-based inversions to form (Ahrens, 1994).

1.2 Methods for Estimating SA Temperature and SA-FA Relationships

Lapse rate is defined as the rate of temperature decrease with height (Whiteman, 2000). Although lapse rates are usually positive, they can vary considerably, and even negative lapse rates (inversions) are common in winter (Barry, 2008). Many studies simply use linear lapse rates to interpolate weather station data to other elevations where SA measurements do not exist (e.g., Martinec and Rango, 1998; Régnière, 1996; Running et al., 1987; Thornton et al., 1997). As Harlow et al. (2004) state, this is a problem because SA temperatures are influenced by the variable underlying land surface characteristics, yielding microclimates and irregular lapse rates (e.g., McCutchan, 1984; Mayr, 2000). This is particularly problematic in the quiescent, clear-sky conditions that many of these studies investigate, where radiation-driven local effects tend to dominate. Overcast conditions, which have largely been neglected in this area of research, can significantly reduce radiation-driven small-scale variations. Under these conditions, interpolating SA temperatures using a linear lapse rate could significantly reduce the magnitude of temperature errors.

Mean monthly lapse rates from slope stations have also been used to estimate SA temperature (e.g., Paul, 1976; Cortemiglia et al, 1989; Carrega, 1995). Averaging weather station data in this manner, however, provides limited useful information, as the timescale over which the data is averaged is orders of magnitude larger than that over which they fluctuate. Averaging all SA

temperature data to obtain monthly mean lapse rates regardless of synoptic conditions causes unique and important temperature structures to be smoothed out (e.g., Richardson et al., 2004).

Another approach for estimating SA temperatures uses a second order autoregressive model. Furman (1978) derived a SA temperature dependence relationship for a station based on the previous day's temperature. While this persistence-based equation may work reasonably well for quasi-stationary conditions, it would likely perform poorly in rapidly changing conditions.

Several statistical studies (e.g., Douguédroit and de Saintignon, 1970; Peilke and Mehring, 1977) have examined the variation of SA temperature with elevation and have attempted to partition the influences of aspect or surface-based inversions. McCutchan and Fox (1986), for instance, analyzed temperature data on an isolated peak in New Mexico during the Falls of 1981 and 1982. Sensors were placed at the base and mid-mountain on northeast-, northwest-, southeast-, and southwest-facing slopes, as well as at the peak. Data were stratified by day and night with light winds (peak winds <5 m s^{-1}) and strong winds (peak winds >5 m s^{-1}) to highlight influences on temperature due to elevation, wind speed, and aspect. Results from linear regression analysis determined that elevation was a significant predictor without exception, and that the effect of aspect was significant except at 0000 LST when winds were strong. Likewise, Pielke and Mehring (1977) used five years of temperature data collected from weather stations in West Virginia and Virginia, finding that mean monthly temperatures correlated best to elevation during summer as nightly inversions induced larger standard errors in the winter months. Polynomial functions may provide a better fit to winter data (Barry, 2008).

Early work (e.g., Ekhart, 1948) argued for the independence of SA from FA temperatures, but more recent literature (e.g., Barry, 2008) has found a strong link, suggesting that under certain synoptic conditions, FA temperatures can be used to estimate SA temperatures, or vice versa. In support, Mahrt (2006) explains that SA-FA temperature differences are bounded by a maximum value, restricted by thermally-driven circulations that redistribute excess heat. Despite these concepts of interconnected SA-FA temperatures, surprisingly few linear regression studies have used FA temperature as a predictor for SA.

McCutchan (1983) compared temperatures from radiosonde soundings (0400 and 1600 LST) to temperatures measured on the slopes of the San Bernadino Mountains in California for 19 days spread over 3 June–23 October, 1975. Temperatures were measured on various slope aspects and elevations. The SA was generally warmer (0.5–2.9°C) than the FA during the day, and colder (-2–-4.8°C) at night, but topographical influences produced microclimates at certain stations. This resulted in non-linear SA temperature profiles, yet the averaged SA lapse rates were found to be almost identical to that of the FA, even during afternoon. FA temperature at station elevation, mixing ratio, u-component and v-component wind, and total cloud cover were all examined as potential predictors in a stepwise linear regression, but most were discarded, leaving FA temperature as the best predictor for SA at given time and elevation. It was then determined that a single equation (instead of one for each station) could be used to model SA temperature. Here, FA temperature, elevation, and cloud cover were found to be statistically significant predictors. The resulting daytime and nighttime equations, however, produced considerable standard errors of 1.52°C and 1.32°C, respectively.

Aside from aforementioned studies, few attempts have been made to describe SA temperature variation using general statistical models (Barry, 2008). This is perhaps because past attempts have suffered from sizeable standard errors (on the order of 2°C), and have not proven transferable to other regions (e.g., Thompson, 1981; McCutchan, 1983). Some studies use an alternative approach, employing short-term (on the order of a few days), intensive field programs, with the aim of finding stronger SA-FA relationships that are specific to certain weather conditions. Whiteman et al. (2004), for example, compared high-resolution SA (on varying aspects) and FA temperatures in an enclosed alpine basin, under clear, quiescent conditions. In general, nighttime SA temperatures were cooler than the FA above the cold air pool, however, temperatures were more or less horizontally homogeneous within the cold pool. Hence, SA temperatures (independent of aspect) can provide suitable proxies for the FA temperatures within a cold pool under strong stability and weak winds. Whiteman et al. (2004) also speculated that basins or valleys enclosed by sheltering topography provide the best configuration for this SA-FA proxy. While short-term studies such as Whiteman et al. (2004) provide considerable insight into the evolution of temperature structure in alpine terrain, they are unable to establish whether these results are reproducible on other nights with similar synoptic conditions.

Studies in this subject area generally fall into two categories: 1) those with fine-resolution spatial data (e.g., Whiteman et al., 2004; Mayr, 2000) that are able to provide details on temperature structures and processes, but only span a few days at most, and 2) those with annual or multi-decadal observational datasets (e.g., Cortemiglia, 1988) but only a small number of weather stations. Few studies (e.g., Lundquist and Cayan, 2007; Dreiseitl, 1988) have attempted to bridge this gap, but have had limited success due to long distances between SA and FA measurements. This absence of studies dealing with data availability at intermediate temporal and spatial scales is perhaps the most significant gap in the current body of literature.

1.3 Research Objectives

In Whistler, British Columbia, the installation of a dense array of meteorological instrumentation in connection with the 2010 Olympic and Paralympic Winter Games created an unprecedented opportunity to investigate SA and FA temperature structure. This work has many implications for the south Coast Mountains, including improved temperature, precipitation type, and avalanche prediction, and higher quality input for snowmelt models.

Specifically, this Whistler-based field study examines SA and FA temperature profile characteristics and their relation to each other using a new approach of categorizing profiles by cloud cover hours. In doing so, this research will address the following objectives:

- Obtain representative SA and FA lapse rates for each cloud cover category and evaluate the consistency of these profiles
- Describe and explain SA-FA temperature differences and how these profiles evolve over time
- Describe the structure of surface-based inversions both on the slope and within the FA, and provide insight for forecasting their formation, persistence, and break up
- Quantify the SA-FA temperature relation by deriving an equation that determines SA temperature from FA temperature, and vice versa
- Develop a model to construct complete SA and FA temperature profiles for a given cloud cover category.

The remainder of this thesis is organized as follows. Chapter 2 describes the geographical and climatological setting of sites, meteorological instrumentation, and field study design. Chapter 3 presents SA and FA temperature profiles under clear and cloudy sky conditions and discusses the factors that cause differences between them. Additionally, the nature of inversions within Whistler Valley is discussed. In Chapter 4 an equation is developed for diagnosing SA and FA temperatures and finally, concluding remarks and recommendations for future work are presented in Chapter 5.

Chapter 2

Sites, Instrumentation and Field Study Design

Environment Canada (EC) installed over 40 surface weather stations (Olympic Automated Network, hereafter OAN) to gain familiarity with the weather of the 2010 Olympic and Paralympic venues, and to acquire data for use in model output statistics (Joe et al., 2010). Five of these stations were located on Whistler's slopes, and, in addition to the Whistler Mountain Air Chemistry Observatory station, served as the starting point for the observational field campaign presented in this research. Further installation of five University of British Columbia (UBC) temperature sensors in January 2009 created high-resolution pseudo vertical slope-air (SA) profiles. SA temperatures (measured by weather stations on the slope) and free air (FA) temperatures (measured by radiosondes) were analyzed to meet the objectives presented in Chapter 1. Described below are the field sites, instrumentation, and field study design used to collect and analyze data from the Olympic Forecasting Team Practicum (3–24 Feb 2009), the Olympics (5–28 Feb 2010), and the Paralympics (5–21 Mar 2010).

2.1 Climatology and Geographical Setting of the Whistler Region

Located approximately 100 km north of Vancouver, BC, Whistler is nestled in the southernmost Coast Mountains, a range of steep, often glaciated peaks with most ranging in height from 2000–2500 mASL (Fig. 2.1). Whistler is influenced by its proximity to the Pacific Ocean and generally experiences mild winters with frequent low pressure systems bringing ample precipitation to the area (Mass, 2008; Roeger et al., 2002). The general northeast-southwest orientation of the Whistler Valley causes low-level valley winds to be topographically channeled to either southwesterly "inflow" winds (flowing inland from the Coast) associated with low pressure systems (Klock and Mullock, 2001; Barton, Personal Communication), or northeasterly "outflow" (flowing from the Interior to the Coast) winds from continental

anticyclones. Outflow events bring dry, cold air down the valleys, through mountain gaps, towards the Strait of Georgia (Mass, 2008). Consideration of local complex terrain effects is of utmost importance when estimating temperature patterns in this area. Wind channeling through narrow valleys and mountain passes along with thermally-driven up- and down-slope flows can lead to low cloud formation and rapid changes in precipitation type (Mailhot et al., 2010).
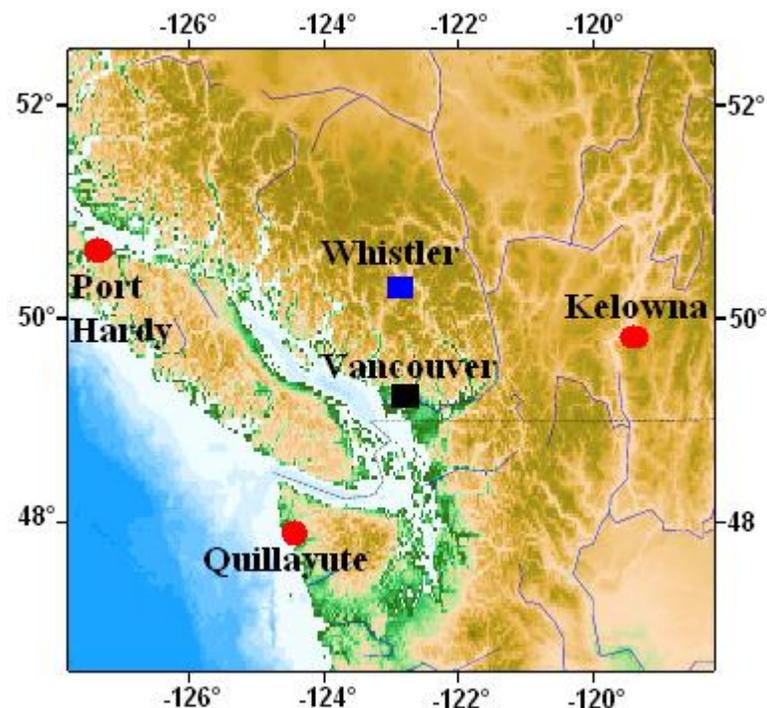
Figure 2.1: Map of study region showing the location of Whistler (blue square), Vancouver (black square), and surrounding radiosonde stations (red circles).

Whistler Mountain is heavily forested up to the tree line at approximately 1750 m, with the exception of numerous large swaths that have been clear cut for ski trails. The large vertical relief results in significant temperature differences between Whistler's base (654 m) and peak (2180 m). It is therefore not uncommon for rain to be falling in Whistler Village with heavy snowfall in the alpine. Despite these spatial variations, snow depths ranged from 1.2–3.6 m on the upper portions of the mountain to 0.70–1.27 m near its base during the study period.

2.2 Instrumentation

2.2.1 EC Slope Air Temperature Sensors

Four EC surface observing stations (VOT, VOB, VOL, VOH) were positioned on the west slope along the alpine courses and one (VOA) on the northeast slope (Table 2.1; Fig. 2.2). Each installation followed the Meteorological Service of Canada (MSC) "Siting Standards for Meteorological Observing Sites" (MSC, 2001), which were derived from World Meteorological Organization recommendations (WMO, 1996), individual instrument manuals, and manufacturer's recommendations (Wong, Personal Communication). While a variety of meteorological instrumentation was present at the EC stations, only temperature sensors are relevant to this study. Joe et al. (2010) provide a more detailed account of site instrumentation and Olympic weather services. All instrumentation operated continuously during the three observational periods with funding provided by EC and the Vancouver Organizing Committee for the 2010 Olympic and Paralympic Winter Games (Doyle, Personal Communication).

Station ID	Latitude (hddd°mm'ss.s")	Longitude (hddd°mm'ss.s")	Elevation (mASL)
VOT	N50 04 45.2	W122 57 04.4	782
VOB	N50 04 37.0	W122 56 52.1	918
VOL	N50 05 06.7	W122 57 51.4	1300
VOA	N50 05 15.8	W122 58 37.3	1624
VOH	N50 05 30.0	W122 58 51.3	1662
WHI	N50 03 33.4	W122 57 27.2	2180

Table 2.1: Locations of EC surface stations used in this study. The use of mASL within this table and in subsequent text indicates metres above sea level.

Each 3-m high platform (e.g., Fig. 2.2a) contained a Campbell Scientific HMP45C temperature sensor housed within an unaspirated 10-plate radiation shield positioned on an arm that stretched outwards from the platform. All instrument specifications, including UBC sensors (below), are described fully in Appendix A. Surface station maintenance was provided by Whistler Mountain ski patrol who removed accumulated snow as needed. Data loggers recorded the average 1-minute temperature once every 15 minutes.
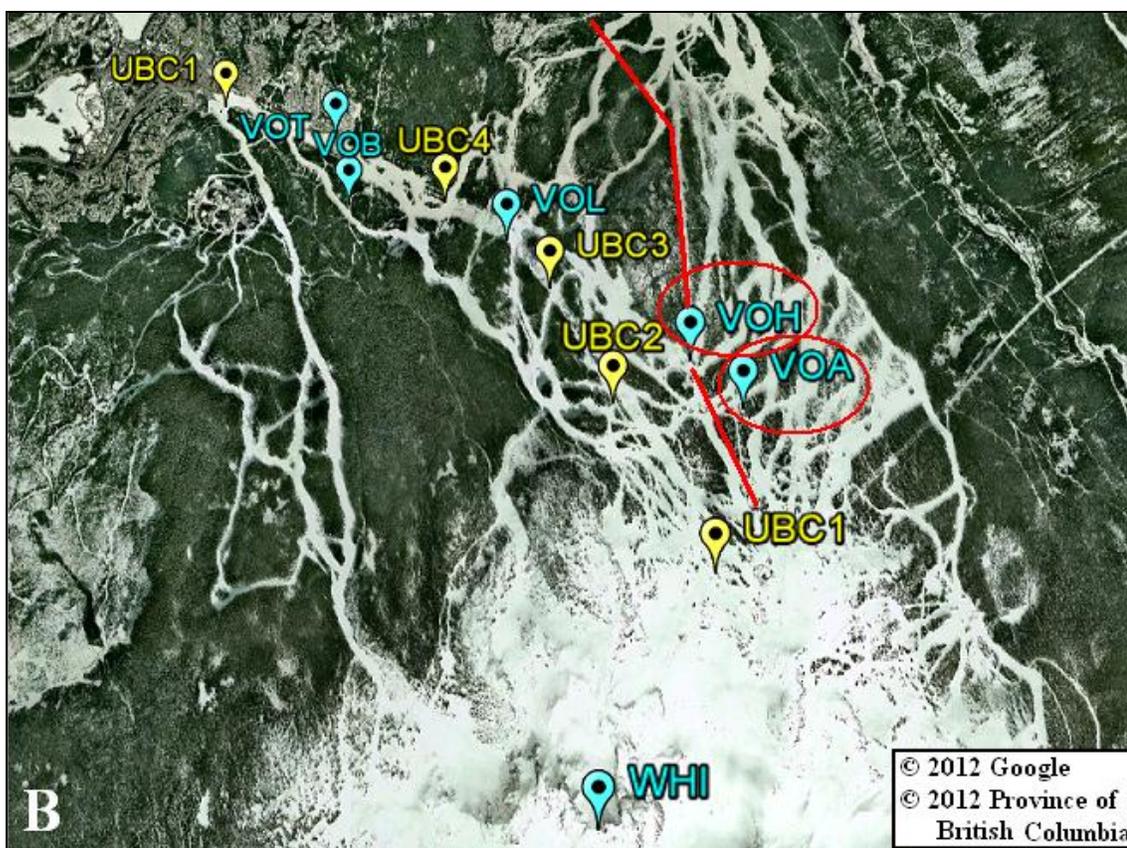
Figure 2.2: a) EC surface station (VOB), and b) locations of VOA and VOH (red circles) relative to the ridge line (red line) which separates VOA from the west slope and the rest of the stations (image courtesy of Google Earth).

A sixth EC observing station, WHI, was located at the summit of Whistler Mountain (Table 2.1; Fig. 2.2b). It contained a Campbell Scientific HMP45CF temperature sensor housed in a 10-plate radiation shield, and was mounted to a post on the northwest side of the Air Chemistry building. The data logger recorded instantaneous temperatures every minute.

Analysis of SA temperature profiles from winter 2009 and 2010 revealed that VOA frequently reported temperatures that deviated significantly from adjacent stations, including nearby VOH. This is most likely explained by the different aspect (northeasterly) of VOA (Fig. 2.2b), the tall vegetation sheltering it on all sides, and a topographic concavity leading down to it from the southwest. These factors affect the amount of intercepted radiation and its susceptibility to cold air drainage (Barton, Personal Communication). VOA was sited to ensure representative precipitation measurements first and foremost, and its resulting sheltered location compromises wind and temperature measurements to some extent (Wong, Personal Communication). Measurements from VOA frequently skewed the mountainside temperature profile, producing unrealistic lapse rates. To confirm the anomalous nature of the VOA readings, temperature profiles (excluding VOA) were fitted with a loess curve, and temperature at the elevation of VOA ($T_{VOA\ loess}$) was calculated. The difference between $T_{VOA\ loess}$ and T_{VOA} was found to be non-zero, indicating that T_{VOA} is inconsistent with the statistical nature of the bulk dataset; VOA temperature data are therefore omitted from this study.

Together, WHI and the four OAN stations (excluding VOA) will be referred to as *EC stations*. For a detailed overview of the siting for each weather station, refer to Appendix B.

2.2.2 Additional Slope Air Temperature Sensors

As part of the UBC component of this study, five temperature sensors (UBC1, UBC2, UBC3, UBC4, UBC5) were installed on lift towers (hereafter *UBC stations*; Table 2.2). Temperature sensors (Hoskins Scientific U23-002 Hobo sensor and data logger) were placed in a non-aspirated 10-plate radiation shield and attached to the northeast side of lift tower ladders (Fig. 2.3).

Station ID	Latitude (hddd°mm'ss.s")	Longitude (hddd°mm'ss.s")	Elevation (mASL)
UBC1	N50 04 15.0	W122 57 02.8	1763
UBC2	N50 04 39.5	W122 57 24.1	1599
UBC3	N50 04 57.2	W122 57 39.8	1462
UBC4	N50 05 14.8	W122 58 10.0	1040
UBC5	N50 05 36.1	W122 59 16.2	654

Table 2.2: Locations of UBC stations used in this study.

Figure 2.3: UBC temperature and relative humidity sensor (UBC3) within a radiation shield and its attachment to the ski lift tower ladder.

Three criteria were used to select appropriate lift towers:

1) Elevation: to fill in data gaps left by EC stations and provide equal vertical spacing of temperature measurements
2) Accessibility: for downloading data and maintenance purposes
3) Terrain: similar exposure to radiation and wind, and to avoid topographical features prone to localized temperature modifications (i.e., cold air sinks)

Additionally, UBC stations adhered to the siting standards of EC stations (MSC, 2001) summarized in Appendix C. Following WMO guidelines, temperature sensors were placed at 1.5 mAGL (WMO, 1996). Regular visits (every 2–4 weeks) ensured the sensors remained unblocked by accumulated frozen precipitation and that they maintained their 1.5 mAGL height (which varied somewhat according to snow depth).

During the Olympic and Paralympic periods, direct access to two UBC sensors was denied, but visual inspections allowed for monitoring of site conditions. Fortunately, temperature sensors remained within 0.17 m of the target height, with the exception of a period of less than 24 h on March 16, 2010.

Despite omitting VOA temperature data from the analysis, this was the only EC station where permission was given to temporarily mount UBC stations and determine if systematic differences existed between the two types of sensors. Using a two-week dataset from January

2009, statistical tests of temperature differences (UBC-EC) produced a mean bias of -0.04°C and a root mean square difference of 0.44°C. Given the accuracies of these sensors, ±0.36°C and ±0.30°C for UBC and EC, respectively (Appendix A), these discrepancies were deemed to be within an acceptable range, and no corrections were applied. UBC sensors were then relocated to their permanent positions along the west slope of Whistler Mountain as described above. Loggers were first set to record instantaneous temperatures every five minutes from January 2009 to January 2010. The logging interval was then decreased to record instantaneous temperatures every 15 minutes to preserve data logger memory space during February and March 2010. Together, EC and UBC stations create high-resolution (average of 170 m vertical separation) SA temperature profiles from 654–2180 mASL (Fig. 2.4).
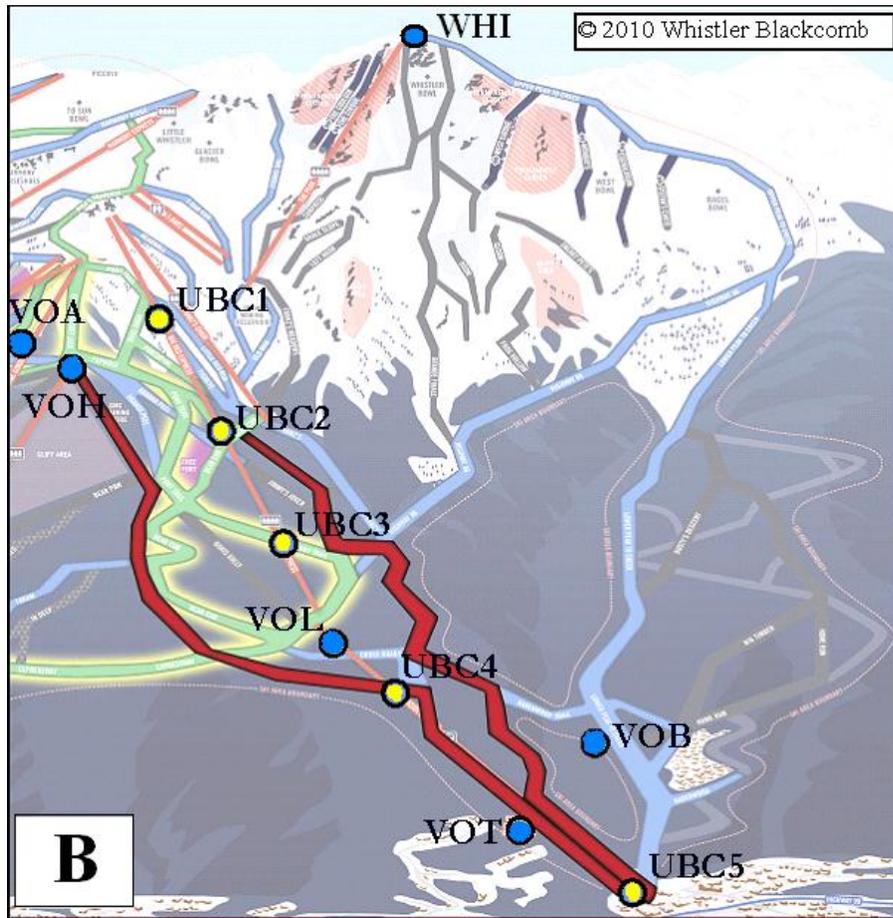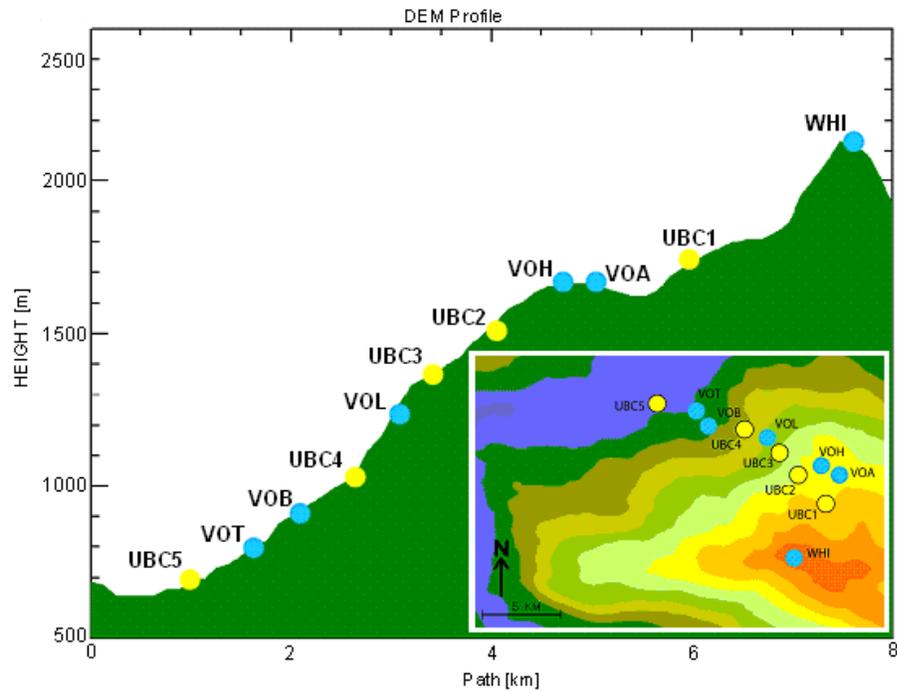
Figure 2.4: Locations of EC (blue) and UBC (yellow) stations overlaid on (a) a digital elevation model cross-section (plan view topographic map inset [shaded every 200 m]), and (b) Whistler-Creekside ski trails with Men's (left), Women's and Paralympic (right) alpine courses (red). Images courtesy of Paul Joe (EC) and Whistler Blackcomb.

2.2.3 Whistler Radiosonde

Following similar definitions in Ekhart (1948) and Whiteman et al. (2004), FA is defined as the column of air over the centre of Whistler Valley. To gather FA temperature data, radiosondes were launched from the Whistler radiosonde station (VOC), installed and operated by EC. The station was co-located with the manned Whistler weather station (WAE) approximately 5 km north of the Whistler-Creekside slope (Fig. 2.5). It took 4–10 minutes for the Whistler radiosonde to ascend from valley bottom to summit level. Due to the short flight duration and limited temporal resolution of the SA temperature sensors, radiosonde profiles are assumed to be an instantaneous measurement at the time of their launch [e.g., radiosondes launched at 0315 PST (FA) are compared to SA temperature observations at 0315 PST].
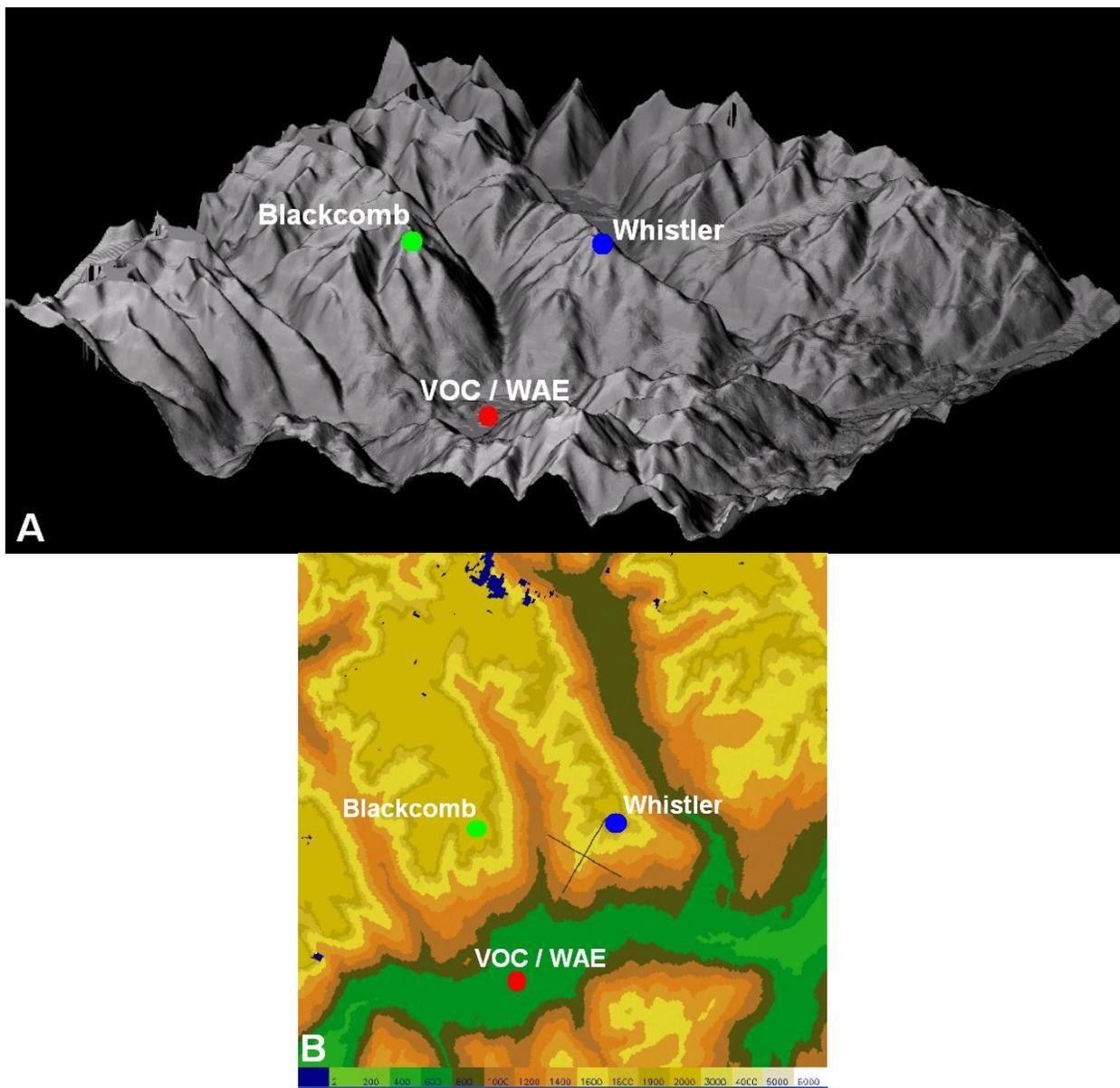
Figure 2.5: Maps of Whistler Valley and surrounding terrain using (a) a shaded smoothed rendering of a 3-arc-second digital elevation model looking south-southeast, and (b) a plan view topographic map (shaded every 200 m). Locations of Whistler radiosonde station/manned observing station (red), Whistler Peak (blue), and Blackcomb Peak (green) are shown for reference (Images courtesy of Paul Joe, EC).

Vaisala RS92-SGP Radiosondes were used at this site, recording temperature, humidity, pressure, wind direction, and wind speed every two seconds (Appendix A). The raw data was then quality controlled by EC, and released for public use (Bowling, Personal Communication). Whistler radiosondes were launched three times daily (0315, 0915, and 1515 PST) from 3–24 Feb 2009, four times daily (0315, 0915, 1515, and 2115 PST) from 5–28 Feb 2010, and two times daily (0315 and 1515 PST) from 5–21 Mar 2010. Data from the 0315 and 1515 PST launches were primarily used in this study, although case studies use additional launch times.

21

2.3 Field Study Design

This field study was designed to investigate the relation between SA temperature profiles on Whistler Mountain and FA profiles over the valley during wintertime under clear sky and cloudy conditions. To this end, nighttime and daytime SA and FA temperature profiles were categorized by cloud cover.

Local sunrise (sunset) for February 2009/2010 varied from 0657–0745 PST (1706–1753 PST) and from 0630–0727 PST (1754–1943 PST) for March 2010. Large areas of Whistler Mountain lose sunlight (and start cooling) well before sunset (Howard and Stull, 2011). The soundings at 1515 and 0315 PST proved the most logical times to observe the cumulative effects of daytime heating and nighttime cooling processes. Therefore, the *daytime* (*nighttime*) periods will be defined as 0700–1515 PST (1900-0315 PST), inclusive.

Cloud cover was categorized by cloud cover hours (CCH), adapted from Stull (1991), defined here as:

(1) $$\text{CCH} = \sum_{i=1}^{5} C_i h_i \, ,$$

where C_i is the value of fractional cloud cover (defined in Table 2.3) for the cloud layer with the most extensive coverage, and h_i is the number of hours C_i was observed.

i	Assigned value of fractional cloud coverage (C_i)	Actual fractional cloud coverage defined by METAR code	METAR cloud cover descriptor
1	8/8	8/8	OVC
2	6/8	5/8–7/8	BKN
3	3.5/8	3/8–4/8	SCT
4	1.5/8	1/8–2/8	FEW
5	0/8	0/8	SKC

Table 2.3: Cloud cover values used to calculate CCH. The value of C_i (column 2) was assigned using the average fractional sky coverage defined by METAR (aviation routine weather report) code. For example, BKN (broken) cloud cover implies 5/8–7/8 coverage, hence an average value of 6/8.

Cloud cover hours were summed during the nighttime and daytime periods. Hourly cloud cover was obtained from the observing site WAE. Cloud cover observations were taken around the clock at WAE in February and March 2010, however, in February 2009 observations were only taken from 0700–1600 PST. Supplementary data (described below) was used to fill these gaps.

Clear skies are defined as daytime/nighttime periods having CCH <1/3 the duration of the period, while *cloudy skies* have CCH values >2/3 of the period. *Partly cloudy sky* periods are omitted from this study to maintain a definitive distinction between cloudy and clear conditions.

Cloud cover conditions were further verified by use of satellite imagery and web cameras. GOES 11 visible satellite imagery (4-km resolution) provided top-down verification of cloud cover during the day (satellite data courtesy of EC). Nighttime cloud analysis used GOES 11 infrared satellite imagery (8-km resolution) with cloud-top temperature colour enhancement for cloud height identification.

Webcam images (10-minute resolution) from VOC were used to corroborate cloud cover reported by the valley observer at WAE. A second webcam situated near the top of Blackcomb Mountain pointing southwards towards Whistler Mountain confirmed the extent of cloud cover above the peak. The latter web camera was particularly important because a valley observer can only discern cloud base and not its vertical extent over Whistler Mountain. Together, satellite imagery and webcams were used to eliminate days/nights where broken or overcast cloud layers did not extend above the summit from the cloudy sky category.

One adjustment to the WAE-calculated CCH was made for days/nights that were categorized as partly cloudy or overcast but only contained thin (cloud opacity 0/8–3/8, as observed in webcam images), high cirrus. Upon comparing clear sky profiles to those with cirrus, it was found that thin cirrus had little to no impact on slope or free air profiles. This type of cloud does not appear to affect the daytime/nighttime radiation budget enough to cause a significant effect on slope or free air temperatures (Pepin and Norris, 2005; Oke, 1978).

Profiles for 20–21 Feb 2009, and 18–21 Feb 2010 were classified as having clear skies, but are not included in the clear sky category of profiles due to persistent inversion conditions. Under

these circumstances the vertical temperature structure and evolution differ significantly from the diurnal inversion formation and breakup found in other clear sky cases. These are instead discussed separately in case studies in section 3.4.

Analysis of cloudy sky profiles revealed two subcategories. Manual synoptic classification using satellite interpretation determined whether a profile was collected within the pre-/post-frontal airmass, or within the frontal zone, which generally featured heavier precipitation and stronger winds. This "circulation-to-environment" method of classification (Yarnal, 1993) delineated the pre-/post-frontal (type A) profiles from those obtained within the frontal zones (type B). Under an idealized setting, one might expect a systematic difference in lapse rates between the pre- and post-frontal airmasses. In this study, however, SA and FA temperature profiles are below ridge top within complex terrain, and lapse rates typically associated with pre- and post-frontal conditions are significantly altered by upstream terrain.

2.4 Chapter Summary

This chapter provided an overview of the 2009/2010 observational field study designed to meet the objectives outlined in Chapter 1. Careful site selection in conjunction with continuous maintenance resulted in a high-quality data set. Further, the combined use of bottom-up (METAR and VOC webcam) and top-down (Blackcomb webcam and satellite) cloud cover observations allowed for a robust classification of sky conditions. The *clear sky* and *cloudy sky* categories are now used to explore the wintertime relation between SA and FA temperature profiles.

Chapter 3

Comparisons of Slope Air and Free Air Wintertime Temperatures

3.1 Introduction

In this chapter temperature profiles from the west slope of Whistler Mountain (SA) are compared to the Whistler radiosonde data (FA) to determine the SA-FA temperature relation during wintertime over a snow-covered surface. The analysis is organized into clear sky conditions followed by cloudy sky conditions, each examining profiles for the daytime and nighttime. After determining representative lapse rates for each cloud cover category, differences between SA and FA temperatures are explained. Case studies are then used to describe how clear and cloudy sky profiles evolve over time. The final section analyzes the formation and dissipation of inversions in Whistler Valley.

3.2 Winter Clear Sky Analysis

In this section, comparisons are made between SA and FA temperature profiles for daytime (1515 PST) and nighttime (0315 PST) clear sky conditions. First, an overview of the temperature profiles and their tendencies for each cloud cover category is provided. Using these qualitative descriptions, temperature differences between the SA and FA for a wintertime, snow-covered surface are compared with literature on slope-free air temperature relations.

3.2.1 Vertical Profiles: Day and Night

In Fig. 3.1 clear day profiles are origin-adjusted by removing the vertically-averaged mean temperature, so that the vertical temperature structures can be more easily compared. The profiles feature generally consistent near-dry adiabatic lapse rates, and consequently the averaged profiles (Fig. 3.1 black lines) are representative of typical FA and SA profiles for clear days at 1515 PST. The mean lapse rates for the FA and SA are 8.36°C km^{-1} and 8.04°C km^{-1}, respectively, with both having standard deviations of ~1.30°C km^{-1}. The lapse rates are not statistically different from each other, a result that is further illustrated in Fig. 3.1b which overlays the SA and FA averaged profiles. Thus, the SA and FA data can be combined to yield a single lapse rate of 8.26°C km^{-1} with a standard deviation of 1.25°C km^{-1}.
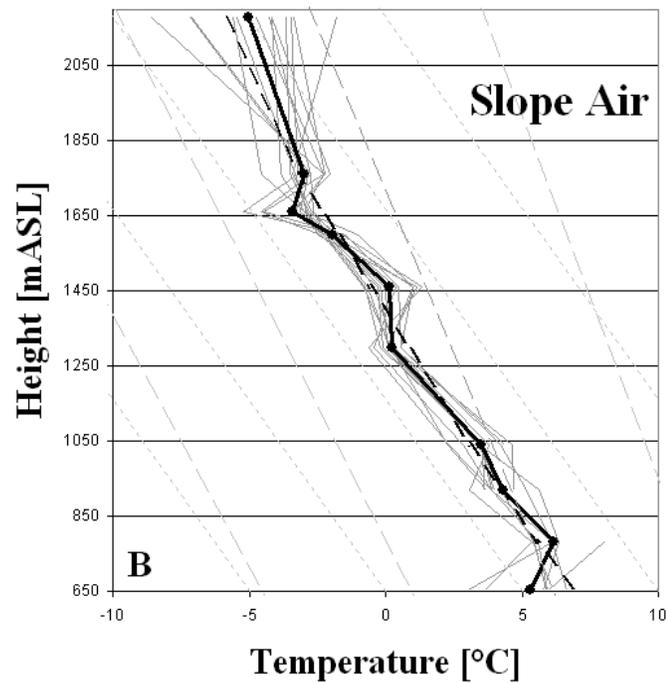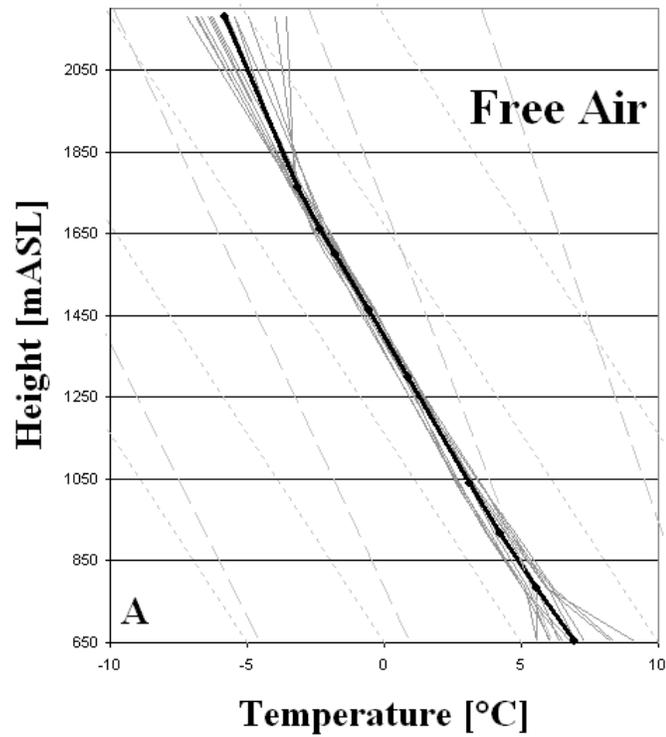
Figure 3.1: Temperature profiles for the category of clear days obtained at 1515 PST for a) FA, and b) SA. All profiles (grey, solid) were origin-adjusted by removing the vertically-averaged mean temperature, and the average profile (black) is provided. Dots in FA profiles (a) are radiosonde data interpolated to the elevation of the weather stations, while dots in SA profiles (b) are the average temperature at each weather station. Dry adiabats (grey, small dashed) and moist adiabats (grey, large dashed) are included for reference. Additionally, the averaged FA profile is shown (black, dashed line) for comparison on (b).

FA profiles are smoother than SA profiles (cf. Figs. 3.1a, b). The station locations for the SA profiles were chosen to minimize representativeness issues, (i.e., avoid microclimates; full site descriptions are provided in Appendix B). In complex terrain, however, it is not possible to avoid these completely, and the effects of shading and other factors (as discussed in section 1.1) are apparent.

Profiles obtained at 0315 PST for clear nights are shown in Fig. 3.2, with the average profile (Fig. 3.2 black lines) representing the typical temperature structure for the FA (Fig. 3.2a) and SA (Fig. 3.2b). The FA profiles reveal a pronounced surface-based inversion layer that develops in the middle of Whistler valley overnight under clear sky conditions. The strong inversion marked by the bottom four stations (UBC5 [645 mASL] to UBC4 [1040 mASL]) is present in all profiles and has an average lapse rate of -9.48°C km^{-1} with a standard deviation of 4.21°C km^{-1}. Above the inversion (UBC4 [1040 mASL] to Peak [2180 mASL]), the average lapse rate is 3.30°C km^{-1} with a standard deviation of 1.88°C km^{-1}. Both portions of the profile are absolutely stable, indicating the suppression of vertical motion throughout the depth of the valley.
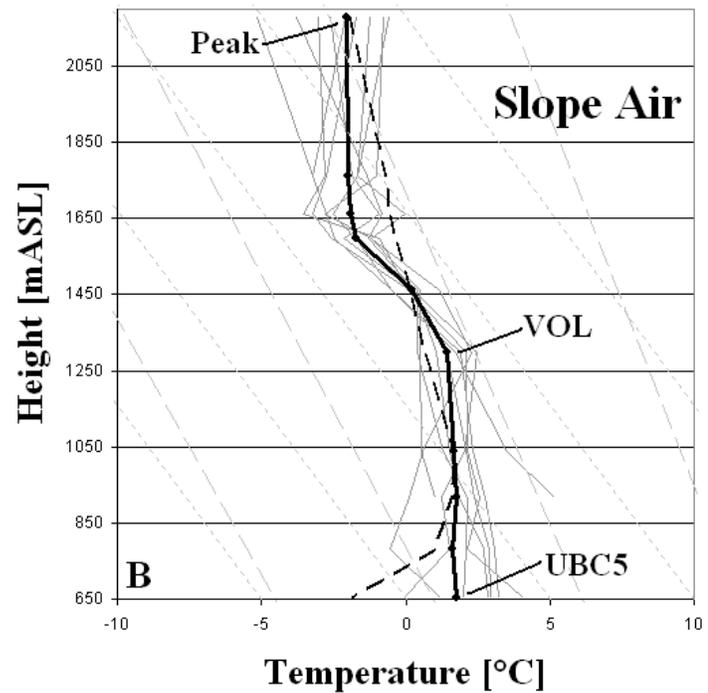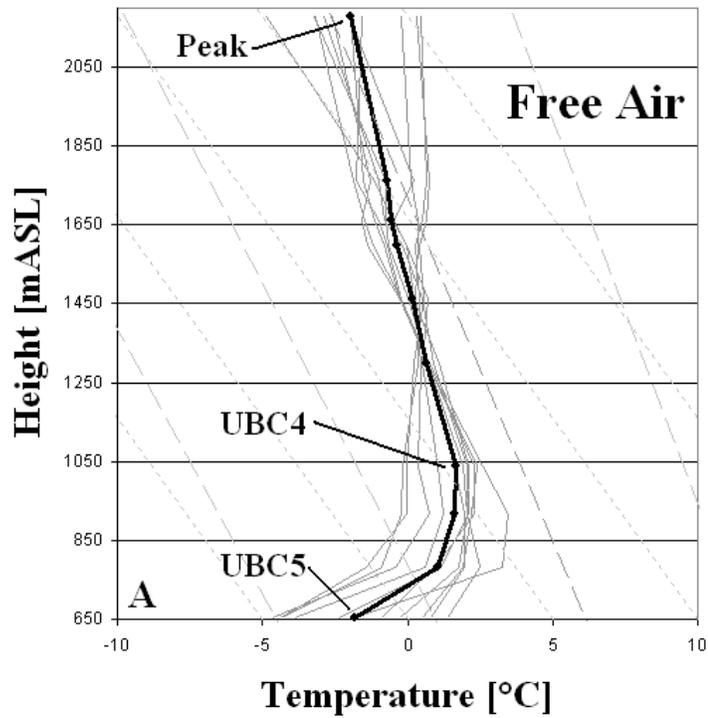
Figure 3.2: Temperature profiles for the category of clear nights obtained at 0315 PST for a) FA and b) SA. All profiles (grey, solid) were origin-adjusted by removing the vertically-averaged mean temperature, and the average profile (black) is provided. Dots in FA profiles (a) are radiosonde data interpolated to the elevation of the weather stations, while dots in SA profiles (b) are the average temperature at each weather station. Dry adiabats (grey, small dashed) and moist adiabats (grey, large dashed) are included for reference. Labeled points are referred to in text.

The SA profiles, by contrast, exhibit a deep, predominantly isothermal layer up to ~1300 mASL (cf. Figs. 3.2a and b). The average lapse rate within the isothermal layer (UBC5 [654 mASL] to VOL [1300 mASL]) is 0.40°C km^{-1} (standard deviation of 3.05°C km^{-1}), becoming 3.94°C km^{-1} (standard deviation of 2.44°C km^{-1}) above the isothermal layer (VOL [1300 mASL] to Peak [2180 mASL]). The FA and SA lapse rates for both the bottom and top portions of the profiles are statistically different from each other and from the daytime clear sky lapse rate.

3.2.2 Daytime Temperature Differences for Summit, Slope and Valley

The discussion of temperature differences between the SA and adjacent FA for daytime (1515 PST) will be divided into three subsections; summit, slope, and valley. Related studies (e.g., Pepin and Lundquist, 2008; Barry, 2008) have adopted similar divisions based on different processes dominating the various regions of the mountain.

Summit

The average SA-FA temperature difference at summit-level (2180 mASL) for clear daytime profiles is 1.17°C (Fig. 3.3). This value is much larger in magnitude and different in sign than the results of numerous other studies. Hansel (1962) found mean monthly daytime SA-FA temperature differences at an 1134-m summit to be -0.5°C and -0.6°C for February and March, respectively. Peppler (1931) found daytime summit SA-FA differences on clear days (cloud coverage of 0/10–1/10) to be -2.2°C. The daytime temperature differences observed in this study more closely resemble values found in summertime studies on bare slopes. For example, Richner and Philips (1984) found daytime summit SA-FA differences of approximately 0.8–2.6°C.
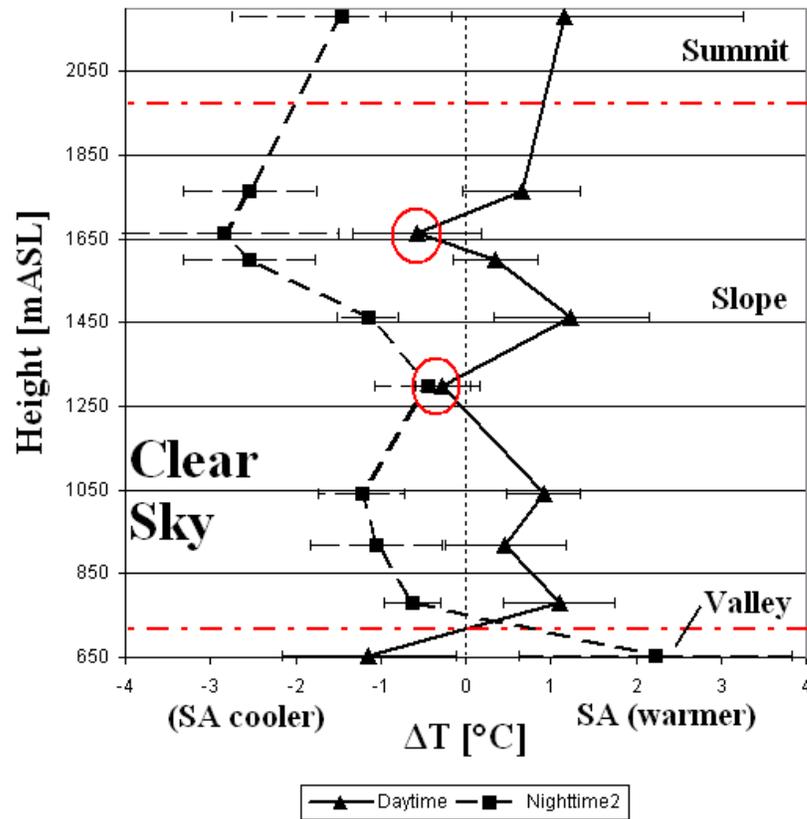
Figure 3.3: Average SA-FA temperature difference at the elevation of each weather station under clear sky conditions for daytime (1515 PST, solid) and nighttime (0315 PST, dashed) temperature measurements. Standard deviation bars are provided. Summit, Slope, and Valley sections are delineated by horizontal, red, dot-dashed lines. Stations VOH (red circle, top), and VOB (red circle, bottom) are highlighted and referred to in text.

There is a relatively large amount of variability both in the summit-level SA and FA temperatures (Figs. 3.1a and b), and in the SA-FA temperature differences (standard deviation of 2.10°C, Fig. 3.3). In fact, large summit-level SA-FA temperature differences of 2.7°C to 4.1°C with an isothermal SA temperature structure between UBC1 and Peak were observed in 36% of clear daytime profiles (e.g., Fig. 3.4a), compared to the much smaller remaining temperature differences of 1.5°C or less. A histogram (Fig. 3.4b) using all daytime summit-level SA-FA temperature differences illustrates this division. A similar discontinuity was found in nighttime data.
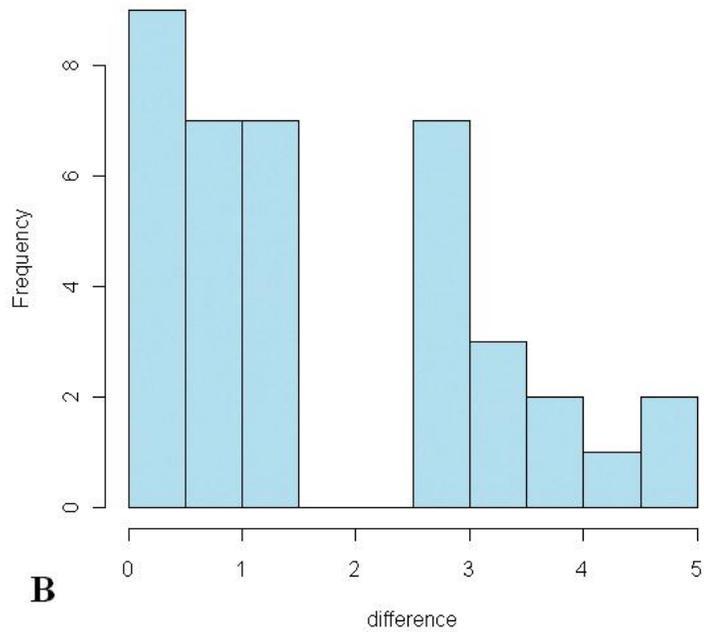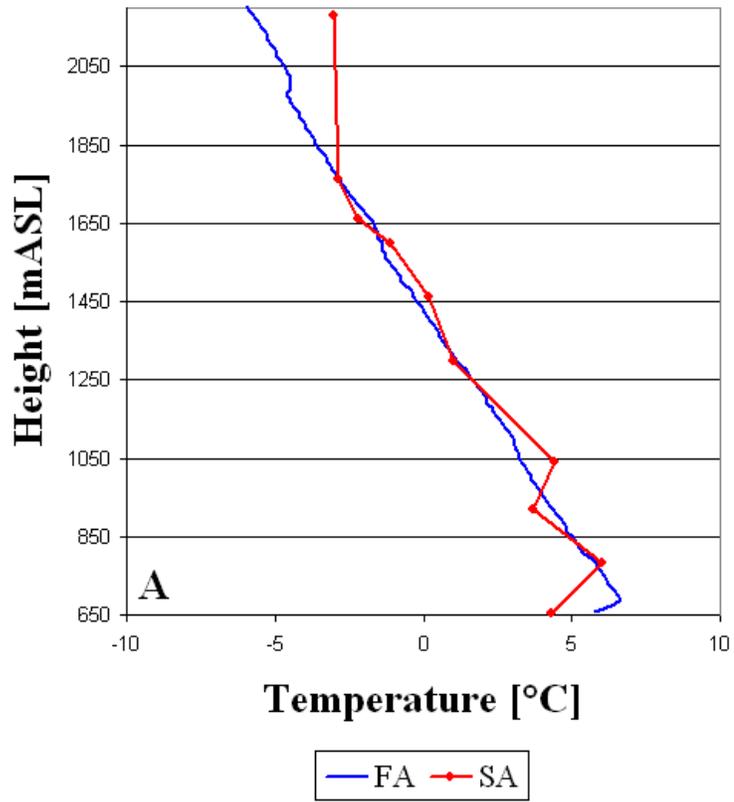
Figure 3.4: a) FA (blue) and SA (red) temperature profiles showing a large positive summit-level SA-FA temperature difference for 1515 PST 19 Feb 2009, and b) a histogram of summit-level SA-FA daytime temperature differences.

Synoptic-scale processes such as warm air advection at the summit are unlikely to be the cause of such large SA-FA temperature differences as the effects would be seen in both the FA and SA temperatures. Furthermore, linear regression analysis failed to reveal any variable (wind direction, wind speed, cloud cover, precipitation, and time of day) as being able to account for these distinct profiles. Therefore, the anomalous summit-level SA warming is a local effect most likely caused by this sensor's unique location (see Appendix B, WHI station). Possible explanations include but are not limited to, additional longwave radiation from the building wall (located within 15 cm of sensor), decreased aspiration due to blocking by the building, or the build up of rime ice on the sensor. Rime ice often accumulates on buildings and instruments on the summit. Not only would this limit aspiration but it would insulate the sensor from the surrounding air, leading to temperature measurements that deviate significantly from actual SA conditions.

Discarding data from profiles displaying this anomalous temperature structure (hereinafter defined as a summit-level SA-FA temperature difference >2.5°C, giving a near-isothermal layer between UBC1 and Peak), the average clear sky summit-level SA-FA temperature difference is reduced from 1.17°C to 0.65°C. Although still warmer than other studies (e.g., Hansel, 1962; Peppler, 1931), these new results likely better reflect the summit-level temperature structure near Whistler Mountain. This temperature difference seems appropriate given the competing processes of surface heating, and the local heat removal by upper-level winds, and is in agreement with similar reasoning found in Pepin and Lundquist (2008).

Slope

During the daytime, SA-FA differences average 0.49°C through the slope portion of the profile (VOT [782 mASL] to UBC1 [1763 mASL]), with an average standard deviation of 0.62°C (Fig. 3.3). These positive SA-FA temperature differences are explained by the greater heating of SA by conduction from the underlying surface than heating of the FA by convective processes. This average temperature difference is smaller than that of McCutchan (1983), who found an average SA-FA difference of 2.1°C during summertime at 1600 PST. This is expected, given the lower amounts of insolation absorbed at the surface in this study due to the higher albedo associated with a snow-covered slope, reduced daylight hours, and lower sun angle. Additionally, solar

energy absorbed by a snow-covered surface is partially expended through the processes of melting and sublimation, and thus the transfer of sensible heat to the air is greatly reduced (Pepin and Norris, 2005).

The sign and magnitude of daytime differences are subject to local factors (e.g., slope angle, aspect, topographical shading, and albedo) that produce variations in the net radiation received by a particular area. This impact of local factors was first shown in Fig. 3.1, and is again illustrated by the non-linear SA-FA differences in Fig. 3.3. In particular VOH and VOL (Fig. 3.3 red circles) have noticeably cooler microclimates. These sites are both situated on raised knolls which have greater exposure to winds, and consequently are more likely to be well-mixed with the adjacent FA. VOL also experiences enhanced shading from nearby trees that border this site to its south. Numerous other studies (e.g., McCutchan, 1983; Whiteman et al., 2004) have encountered similar problems with the placement of stations that are highly subject to local influences and differing levels of exposure.

Valley

Lastly, clear daytime SA-FA valley-level (654 mASL) temperature differences average -1.14°C (i.e., the bottom of the Whistler slope is colder than the near-surface air over the middle of the valley, Fig. 3.3). Differences in surface albedo and topographic shading provide the most likely explanations as the daytime spatial distribution of surface air temperature is primarily forced by insolation (Mahrt, 2006). The radiosonde site, VOC, is closely surrounded by forest to its west and paved roads to its east giving it a much lower effective albedo than the snowy, open slopes that encircle UBC5, allowing for more absorption of insolation and heating during the day. Secondly, topographic shading of UBC5 late in the afternoon results in an earlier cessation of insolation than the area around VOC.

3.2.3 Nighttime Temperature Differences for Summit, Slope and Valley

Summit

The average summit-level (2180 mASL) SA-FA temperature difference for clear sky nighttime profiles is -1.45°C with a standard deviation of 1.29°C (Fig. 3.3). These results are similar to various field studies from other summit locations around the world. For instance, nighttime mean summit-level SA-FA temperature differences of -1.9 and -1.8°C were found for the Harz Mountains, Germany for the months of February and March, respectively (Hansel, 1962). Peppler (1931) similarly found wintertime summit-level SA-FA temperature differences of -2.8°C under clear sky conditions in the northern Alps.

The relatively large standard deviation about the mean at the summit in comparison to all other elevations (Fig. 3.3) can be explained by two phenomena. As was observed with daytime summit-level SA-FA comparisons (e.g., Fig. 3.4a), some nighttime profiles also show anomalously warm temperatures at the summit-level (Peak) station. Secondly, there were cases where the appearance of subsidence warming at the Peak station significantly lagged its appearance in FA measurements, resulting in large temperature differences (up to -6.7°C). This is illustrated using a series of SA and FA profiles from the evening of 17 Feb 2010 until the morning of 18 Feb (Fig. 3.5). From 2115-0315 PST the FA subsidence inversion sinks from 2150 mASL to 1400 mASL (Fig 3.5a). No such warming is observed in the SA (Fig. 3.5b); instead the profile cools. It is not until 0915 PST that the upper portions of the SA profile (>1500 mASL) warm. By this time, the FA subsidence inversion has lowered to ~1000 mASL.
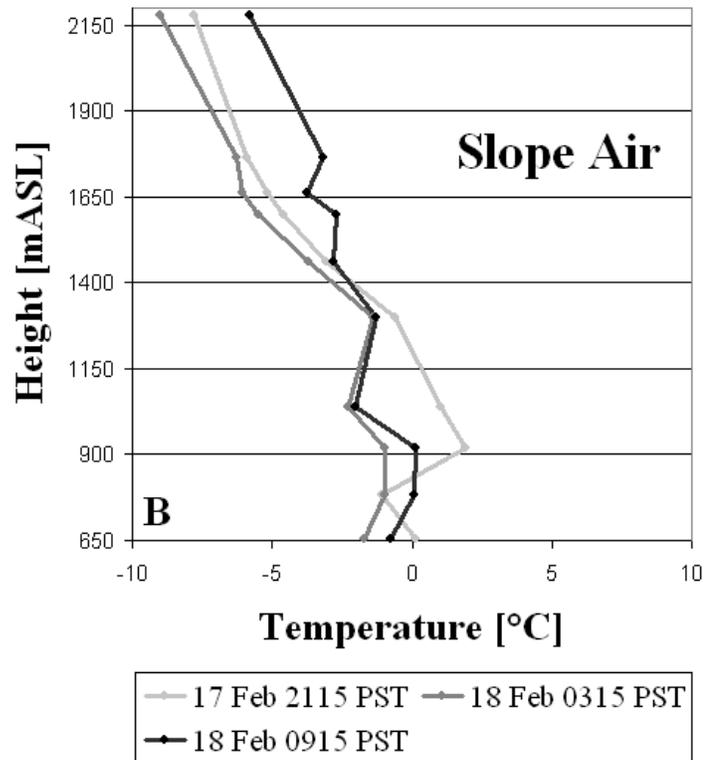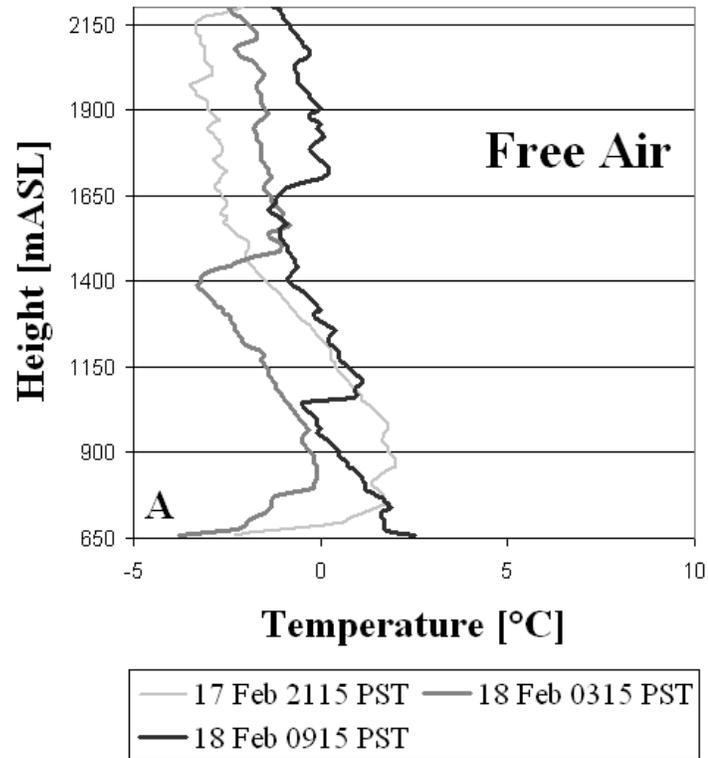
Figure 3.5: Profiles for a) FA, and b) SA at 2115 PST 17 Feb 2010, 0315 PST 18 Feb 2010, and 0915 PST 18 Feb 2010 illustrating the lag in subsidence warming of the SA relative to the FA.

Anomalously warm summit-level SA temperatures and the delay of subsidence warming in the SA, both giving rise to large standard deviations, could result from rime ice on the sensor. Alternatively, the shallow stable layer of cool air that develops on slopes at night may also play a role in preventing subsidence warming from being detected on the slope until daytime heating can destabilize the surface layer and mix down the warm air.

Slope

For nighttime, clear sky conditions, SA temperatures are colder than FA temperatures for the slope portion of the profile (VOT [782 mASL] to UBC1 [1763 mASL], Fig. 3.3). There is, however, a very clear distinction between the bottom half of the slope, where the average temperature difference is -0.90°C, and the top half of the slope, where the average temperature difference increases to -2.64°C. The boundary between these two portions of the profile approximately coincides with the top of the SA isothermal layer (Fig. 3.2). This change occurs consistently at the same level through all clear sky nighttime profiles.

In general, the results from Whistler Mountain agree with the literature (e.g., Whiteman, 2000; McCutchan, 1983; Lundquist and Cayan, 2007), in that nighttime SA temperatures during wintertime over a snow-covered surface should be colder than the adjacent FA. These nighttime differences are predominantly caused by longwave radiation loss from the slope and the downward flux of sensible heat from the near-surface air, which combine to create a layer of cooler slope air. The increase in SA-FA temperature differences above the valley inversion is a feature also documented in a previous nighttime SA-FA temperature comparison in an alpine basin (Whiteman et al., 2004). They observe that as cold air drains downslope, and further down the more gently sloping valley floor, compensatory adiabatically warmed air can enter through the top of the valley atmosphere. This adiabatically-warmed FA at upper levels within the valley creates large horizontal SA-FA temperature differences, whereas the SA-FA temperature differences within the surface-based inversion maintain a much more horizontally homogeneous temperature structure.

Valley

Lastly, comparison of the valley portion of the profile (654 mASL) reveals a nighttime, clear sky SA-FA difference of 2.23°C (Fig. 3.3). Figure 3.2 shows a strong inversion develops in the middle of Whistler Valley versus the isothermal profile found in the SA. The radiosonde launch site is susceptible to cold air drainage from the surrounding mountain slopes as well as additional cold air from the glaciers at the head of Fitzsimmons Creek (Oke, 1978). While gentle down-valley drainage allows some of this air to exit the valley, a large portion pools in the middle of the valley. Furthermore, Olympic Ridge, north of the lowest SA sensor (UBC5) shelters this SA station from the down-valley drainage, and thus UBC5 is subject only to local downslope drainage.

3.2.4 Case Study: Diurnal Temperature Evolution for Clear Skies

Thus far, comparisons have been made between SA and FA temperatures under clear sky conditions at 0315 and 1515 PST along with a discussion of the factors responsible for creating temperature differences between them. A case study is now provided using data from 19–20 Feb 2010 when radiosondes were launched four times daily, and allows for an in-depth examination of how SA and FA temperatures progress throughout a 24-hour period of clear sky conditions. Specifically, this section addresses when and where cooling/heating occurs, its magnitude, and how these changes affect the SA-FA relation.

A surface analysis (Fig. 3.6a) illustrates the ridge of high pressure centred over BC during this time period. The corresponding multispectral satellite image (Fig. 3.6b) shows clear skies over the majority of BC with small amounts of low cloud (denoted by pale yellow shading) seen in the interior valleys.
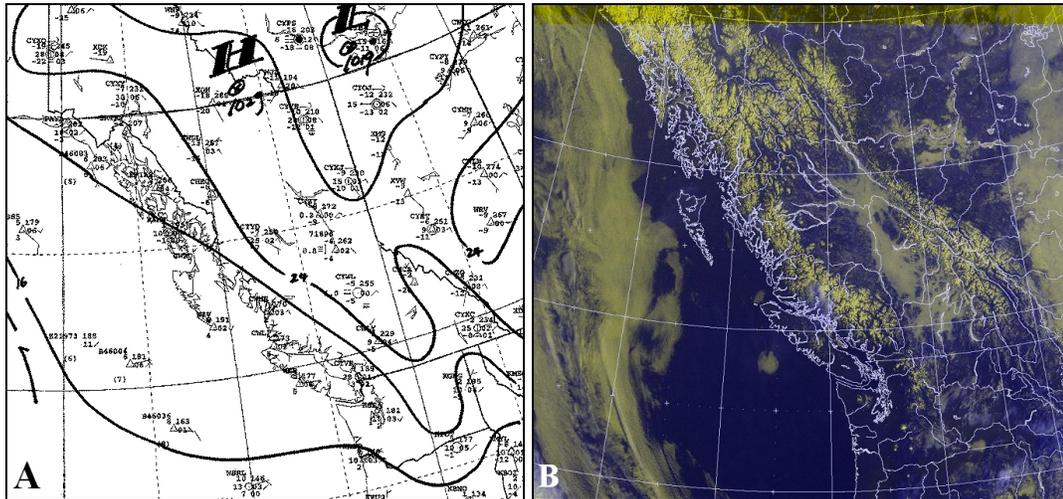
Figure 3.6: (a) Surface analysis, and (b) multispectral visible satellite imagery for BC at 1010 PST 20 Feb 2010 (courtesy of EC). The surface map has sea level pressure contoured every 4 hPa, and fronts and trowals are analyzed with traditional symbols.

The majority of cooling occurs within the first 6 h (1515–2115 PST 19 Feb, Fig. 3.7) and is greatest in the lower levels $[>5°C \ (6 \ h)^{-1}]$, with more uniform, smaller amounts of cooling in the upper levels [average of $2.5°C \ (6 \ h)^{-1}$ for SA, $1.3°C \ (6 \ h)^{-1}$ for FA]. The SA generally experiences greater amounts of cooling than the FA with the exception of the lowest (valley) level. It is during this time that previously warmer SA becomes colder than the FA, and also the time period when the inversion forms in the FA.
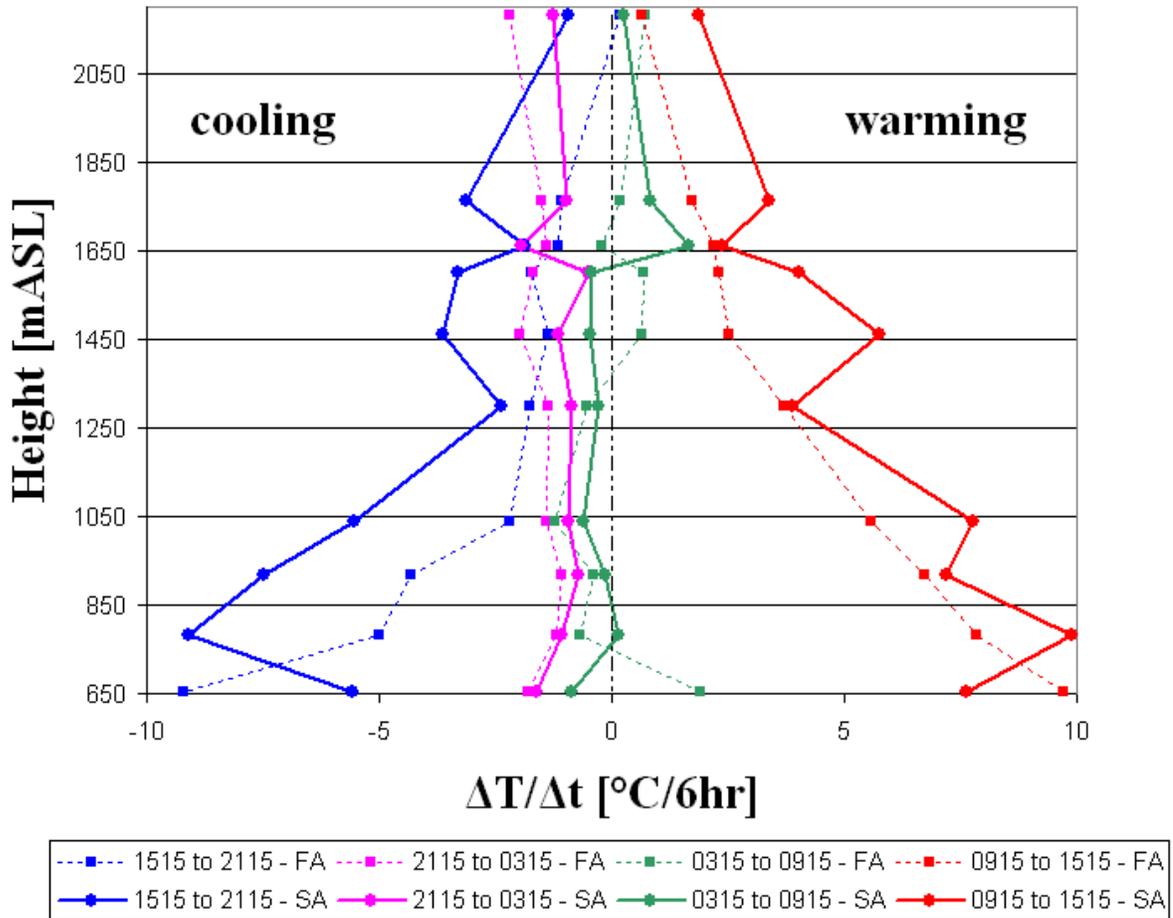
Figure 3.7: 6-h temperature changes under clear sky conditions for SA (solid, circles) and FA (dashed, squares) over time periods denoted during 19-20 Feb 2010.

During the following time period (2115 PST 19 Feb to 0315 PST 20 Feb), similar amounts of cooling occur along the entire profile in both the SA [average of 1.1°C (6 h)$^{-1}$] and FA [average of 1.5°C (6 h)$^{-1}$] (Fig. 3.7). An even smaller amount of cooling occurs in the SA [0.38°C (6 h)$^{-1}$] and FA [0.71°C (6 h)$^{-1}$] during the third time period (0315–0915 PST 20 Feb, Fig. 3.7), with slight warming [0.9°C (6 h)$^{-1}$ for SA, 0.4°C (6 h)$^{-1}$ for FA] occurring on the upper portion of the mountain. The warming results from insolation affecting the upper elevations first in the early morning. The SA warms more during this period, but remains cooler than the FA at this time (not shown).

The SA and FA warm most from 0915–1515 PST 20 Feb. The SA warms 1.7°C (6 h)$^{-1}$ faster than the FA on average at all levels (Fig. 3.7). The bottom portion of the valley atmosphere,

where the inversion is eroded, is where the largest warming occurs. Additionally, increased land surface area at lower elevations leads to more heat transferred to the FA.

These results suggest that daytime SA warming is delayed well past sunrise due to topographical shading, and the majority of nighttime cooling occurs within the first few hours of sunset with little adjustment thereafter. Even where insolation is intercepted earlier by upper portions of the mountain, slope heating is minimal. This is likely due to early morning insolation striking the earth at a very low angle, which means a) it passes through a thicker layer of atmosphere leading to large amounts of scattering and absorption, and b) it strikes the ground at a low angle delivering smaller amounts of energy over a larger surface area (Ahrens, 1994). Further, the high albedo of the snow-covered surface leads to an even smaller amount of energy absorbed by the slope. As the solar angle increases and albedo decays throughout the later parts of the day (Wiscombe and Warren, 1980), more energy is absorbed at the surface and subsequently re-emitted to the FA, contributing to more significant afternoon warming.

Rapid cooling of the SA occurs when the surface no longer receives incoming shortwave radiation but continues to emit longwave radiation. There is, however, a maximum amount of heat that can be lost before temperature gradients between the SA and FA become so large that valley circulations take over to re-distribute energy (Mahrt, 2006). The negligible change in SA-FA temperature differences that occur after 2115 PST suggests the FA and SA have reached an equilibrium; whereby any further radiative cooling on the slope is balanced by the removal of cold air, likely via cold air drainage down-slope and down-valley.

3.3 Winter Cloudy Sky Analysis

3.3.1 Vertical Profiles: Day and Night

As discussed in Chapter 2, cloudy day profiles were divided into pre-/post-frontal profiles, and those within the frontal band. Profiles within these categories (Fig. 3.8) share consistent vertical temperature structures, and consequentially the average profiles (Fig. 3.8 black solid lines) are representative of the typical shapes of the subcategory profiles for cloudy days at 1515 PST. The mean lapse rates for the drier pre-/post-frontal category (type A) for the FA and SA are 7.64°C

km^{-1} and 5.60°C km^{-1}, respectively. The more saturated frontal conditions (type B) produce near-moist adiabatic lapse rates; averaging 5.07°C km^{-1} and 4.31°C km^{-1} for the FA and SA, respectively (compare dashed black lines to solid black lines in Figs. 3.8b and d).
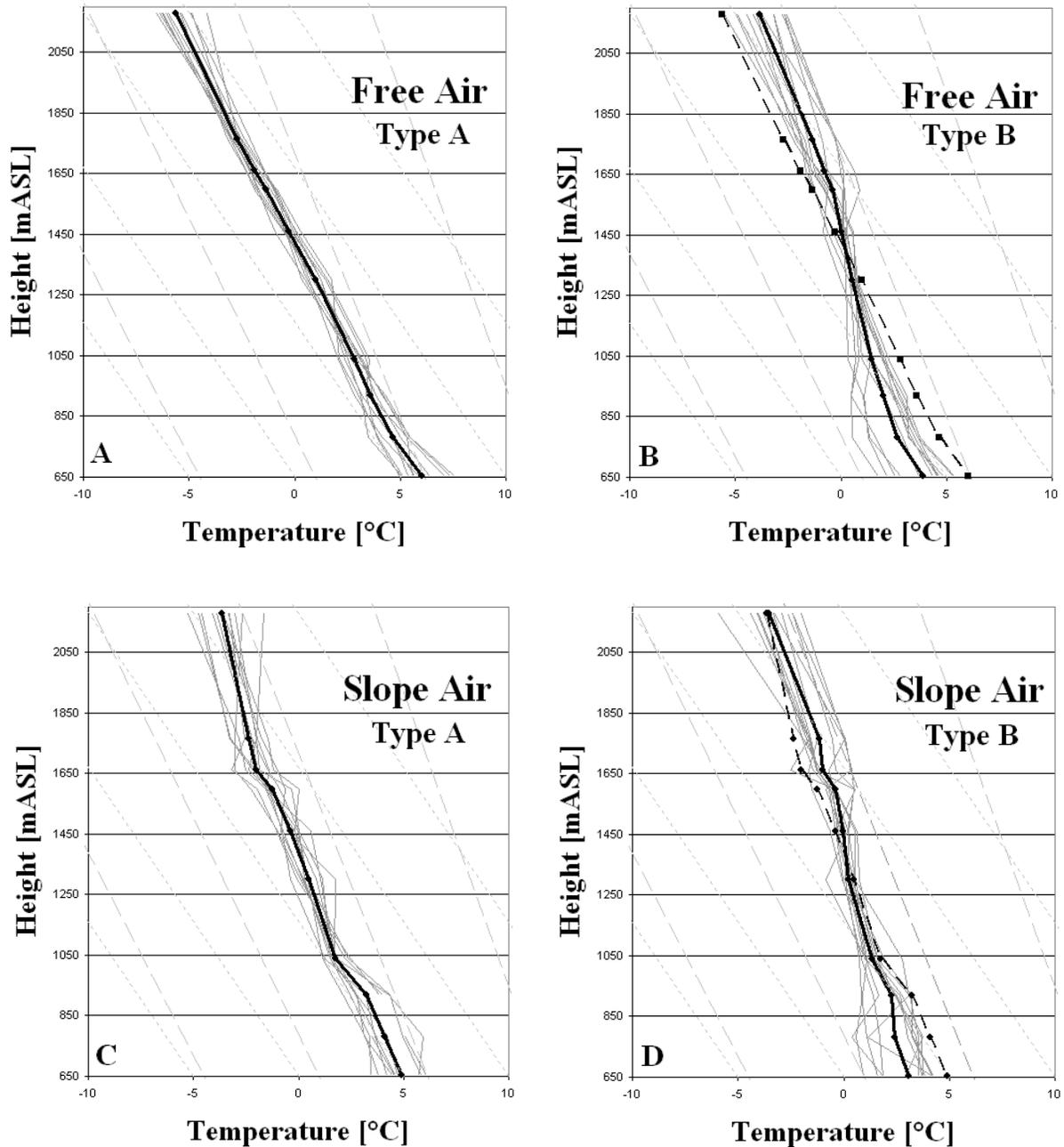
Figure 3.8: Temperature profiles for the category of cloudy days obtained at 1515 PST for a) FA type A, b) FA type B, c) SA type A, and d) SA type B. All individual profiles (solid, grey) were origin-adjusted by removing the vertically-averaged mean temperature, and the average profile (black) is provided. Dots in FA profiles are radiosonde data interpolated to the elevation of the weather stations, while dots in SA profiles are the average temperature at each weather station. Dry adiabats (grey, small dashed) and moist adiabats (grey, large dashed) are included for reference. Additionally, the average FA and SA profile for type A is shown (dashed black line) in (b) and (d) respectively for comparison.

Daytime SA profiles for cloudy skies have more linear lapse rates as compared to those for clear skies (cf. Figs 3.8c and d, Fig. 3.1b). The effect of microclimates is less pronounced as cloud cover reduces incoming shortwave radiation (up to 10% of its clear sky value) and significantly modifies the surface long-wave budget (Oke, 1978).

Cloudy night individual and average air temperature profiles for 0315 PST are shown in Fig. 3.9. The mean lapse rates for type A for FA and SA are 6.11°C km^{-1} and 5.20°C km^{-1}, respectively; while the more saturated, well-mixed type B profiles have more stable lapse rates of 4.23°C km^{-1} and 3.86°C km^{-1} (e.g., black, dashed line tends towards solid, black line in Figs. 3.9b and d).
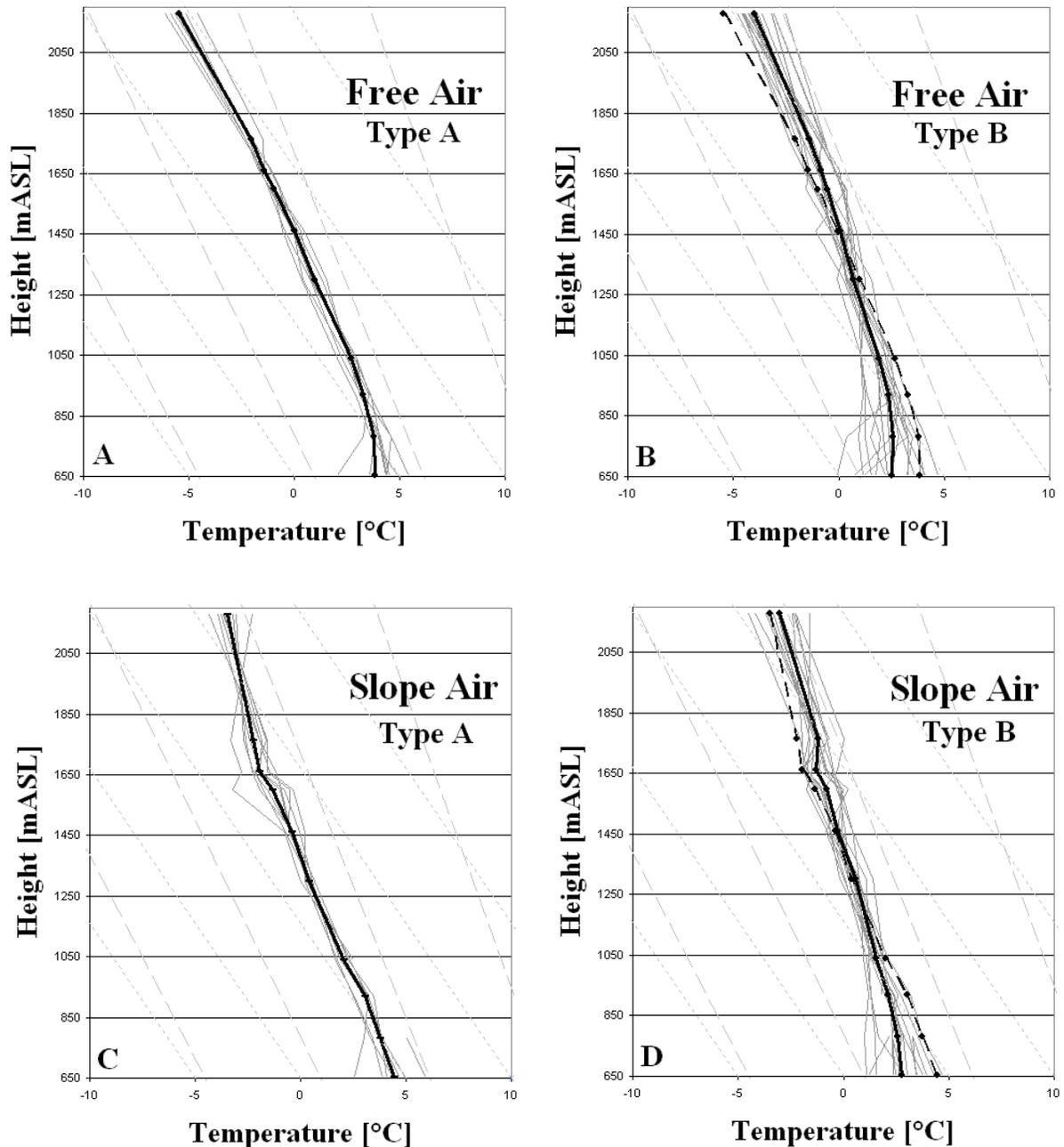
Figure 3.9: Temperature profiles for cloudy nights obtained at 0315 PST for a) FA type A, b) FA type B, c) SA type A, and d) SA type B. All profiles (grey, solid) were origin-adjusted by removing the vertically-averaged mean temperature, and the average profile (black) is provided. Dots in FA profiles are radiosonde data interpolated to the elevation of the weather stations, while dots in SA profiles are the average temperature at each weather station. Dry adiabats (grey, small dashed) and moist adiabats (grey, large dashed) are included for reference. Additionally, the average FA and SA profile for type A is shown (black, dashed line) on (b) and (d) respectively.

For both types A and B, radiative exchange between the cloud cover and surface inhibits the development of a strong, surface-based inversion (cf. Figs. 3.9a-d, Fig. 3.2). Any cold air drainage from the surrounding mountain slopes is unable to produce a deep inversion, and

44

instead a shallow low-level isothermal layer frequently forms in the middle of the valley (Figs. 3.9a and b). This indicates that while the synoptic conditions act to prevent a nighttime inversion from forming, limited cold air drainage and radiative cooling over the snow-covered surface of Whistler Valley still produce a stable surface-based isothermal layer. This isothermal layer is not observed in the SA profiles (Figs. 3.9c and d), where a near-moist adiabatic lapse rate is found throughout.

By comparing all the SA and FA cloudy type A and B lapse rates and their associated standard deviations, certain categories could be combined. Cloudy type A days and nights for SA and cloudy type A nights for FA were statistically similar, yielding a representative lapse rate of 5.63°C km^{-1} with a standard deviation of 0.95°C km^{-1}. Likewise, cloudy type B days and nights for both the SA and FA data can be combined giving a lapse rate of 4.32°C km^{-1} with a standard deviation of 1.26°C km^{-1}. Fig. 3.10 summarizes the statistically significant lapse rates for all cloudy sky categories.
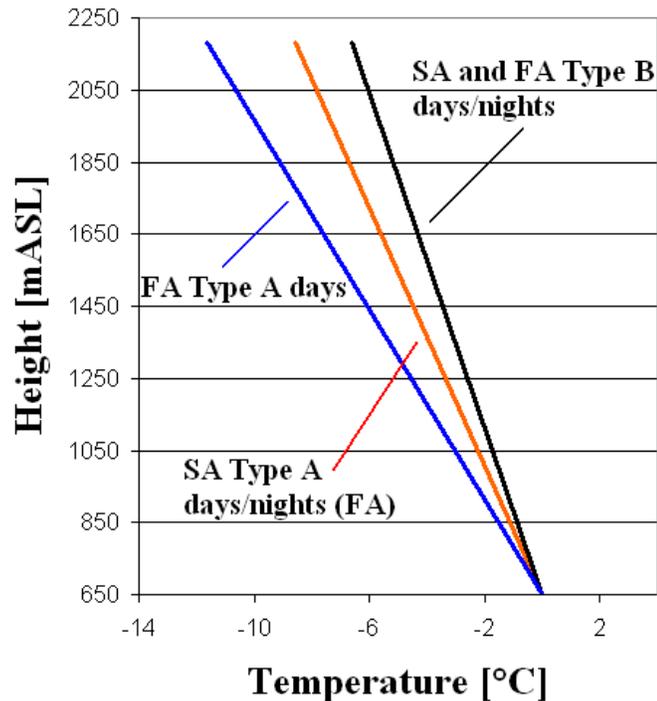
Figure 3.10: Statistically significant lapse rates for cloudy sky categories.

It is not surprising that the datasets for type B day and night are similar as stronger winds within the frontal zone keep the slope-valley atmosphere well-mixed. However, this is the first time, to

the author's knowledge, that a statistically similar lapse rate has been demonstrated throughout the diurnal cycle. It is interesting that cloudy type A SA profiles also yield similar profiles for daytime and nighttime. Data for daytime FA type A was statistically different from all other cloudy sky datasets. This is most likely due to reduced landmass at higher elevations leading to significantly less heat transferred to the FA and ample heat transfer from the sidewalls and valley floor to the FA in the bottom portion of the valley atmosphere, creating a steeper lapse rate.

3.3.2 Daytime Temperature Differences for Summit, Slope and Valley

A discussion of cloudy sky temperature differences between the SA and adjacent FA is now provided with the temperature profiles divided into the same three sections as above: summit, slope, and valley. Comparisons to clear sky conditions will also be made to help explain the different processes that dominate under cloudy conditions.

Summit

The average summit-level (2180 mASL) SA-FA temperature difference for cloudy daytime profiles is 2.61°C and 0.87°C for type A and B, respectively (Fig. 3.11). Comparing these results to other studies, Peppler (1931) found that the average SA-FA temperature difference for a mountain in the northern Alps from October-March was 0.1–0.5°C for cloud cover 8/10 or greater. Summertime observations (April-September) from that same study concluded afternoon temperature differences were only slightly larger at values of 0.8–1.0°C. Richner and Philips (1984) found that 1500 LST temperature differences between the SA and FA were approximately 0.75–1.6°C.
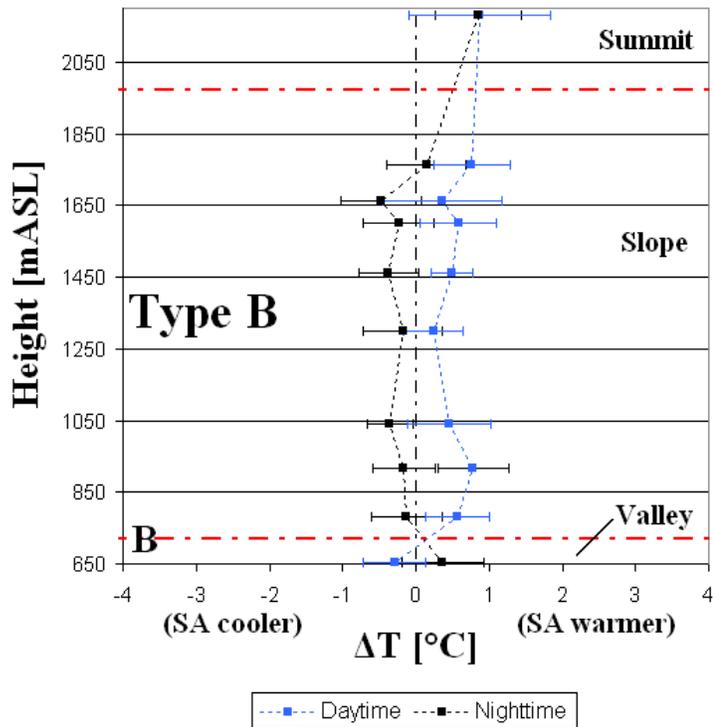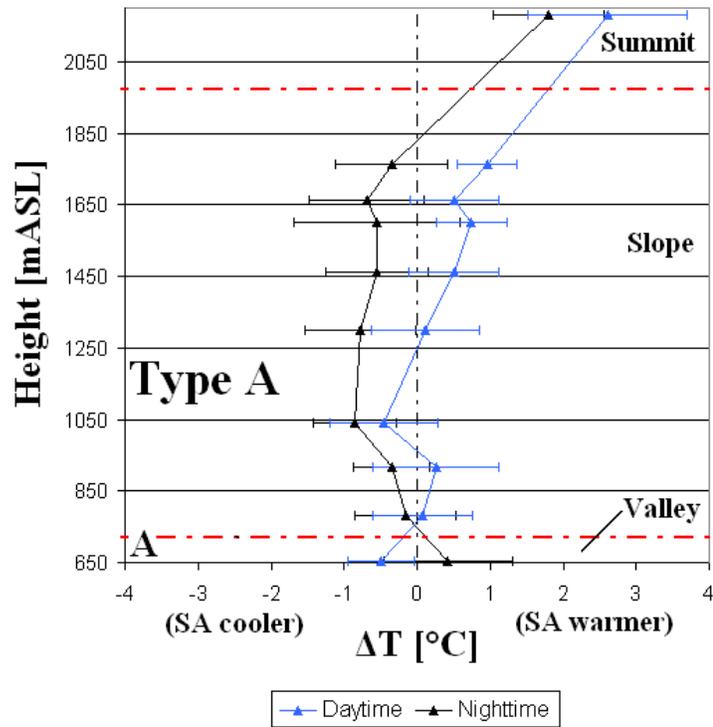
Figure 3.11: Average SA-FA temperature difference at the elevation of each weather station under cloudy sky conditions for daytime (1515 PST) and nighttime (0315 PST) temperature measurements for a) type A, and b) type B. Standard deviation bars are provided. Summit, slope, and valley sections are delineated by red, dot-dashed lines.

Anomalously large positive SA-FA temperature differences also appeared under cloudy skies. For cloudy type A, anomalous differences (>2.5°C) appeared in 42% of all profiles, and in cloudy type B, only 8%. One possible explanation is that the higher wind speeds found near frontal zones keeps the SA and FA well–mixed, reducing local effects. Moreover, the mean FA summit-level temperatures between cloudy type A and B differ by 4°C, with type A averaging -9.2°C and type B averaging -5.1°C (not shown). Type A profiles are within the optimal temperature range for icing on sensors to occur [-9°C–-15°C (MOIP, 2000)], and thus, more cases of anomalously large positive differences are observed.

Slope

In Fig. 3.11b the average SA-FA temperature difference for the slope portion of the profile under cloudy type B daytime conditions is 0.53°C. The SA is heated more uniformly under cloudy as compared to clear sky conditions and the temperature differences are more uniform along the entire slope (c.f. Figs. 3.3, 3.11b).

The well-mixed environments of the stormy type B profiles were expected to produce smaller temperature differences than those of type A. Instead, the average temperature difference for cloudy type A for mid-mountain and below shows almost negligible differences (0.26–0.07°C) with some stations reporting colder SA (up to -0.44°C) (Fig. 3.12). These results are likely due to complications from a phenomenon specific to Whistler Mountain, known as Harvey's Cloud. This cloud has a base above VOT and cloud top below 1850 mASL (Joe et al., 2010; Joe, 2009). Refer to Mo et al. (2011) for a detailed discussion of the formation, persistence and dissipation of Harvey's Cloud. The affect on the vertical temperature structure above the valley, however, is shown for the first time here.
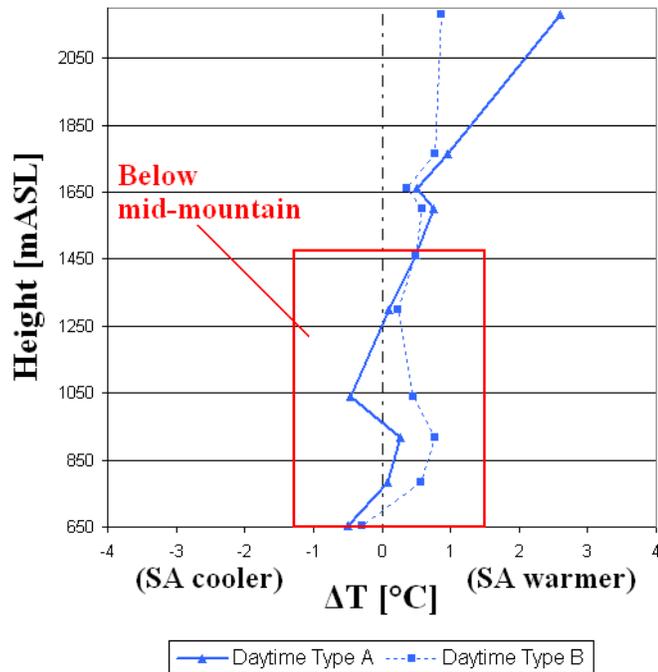
Figure 3.12: Average daytime (1515 PST) SA-FA temperature difference at the elevation of each weather station under type A and B cloudy sky conditions. The bottom portion of the mountain is highlighted and referred to in text.

To illustrate, an example of the effects of Harvey's Cloud from 24 Feb 2010 is now provided. On this date a series of upper-level shortwave troughs passed over the central BC coast creating widespread instability over the region. The southwesterly synoptic flow behind these shortwave troughs dominated Whistler for the entire day with lee wave clouds visible along the southern Coast Mountains (Fig. 3.13).
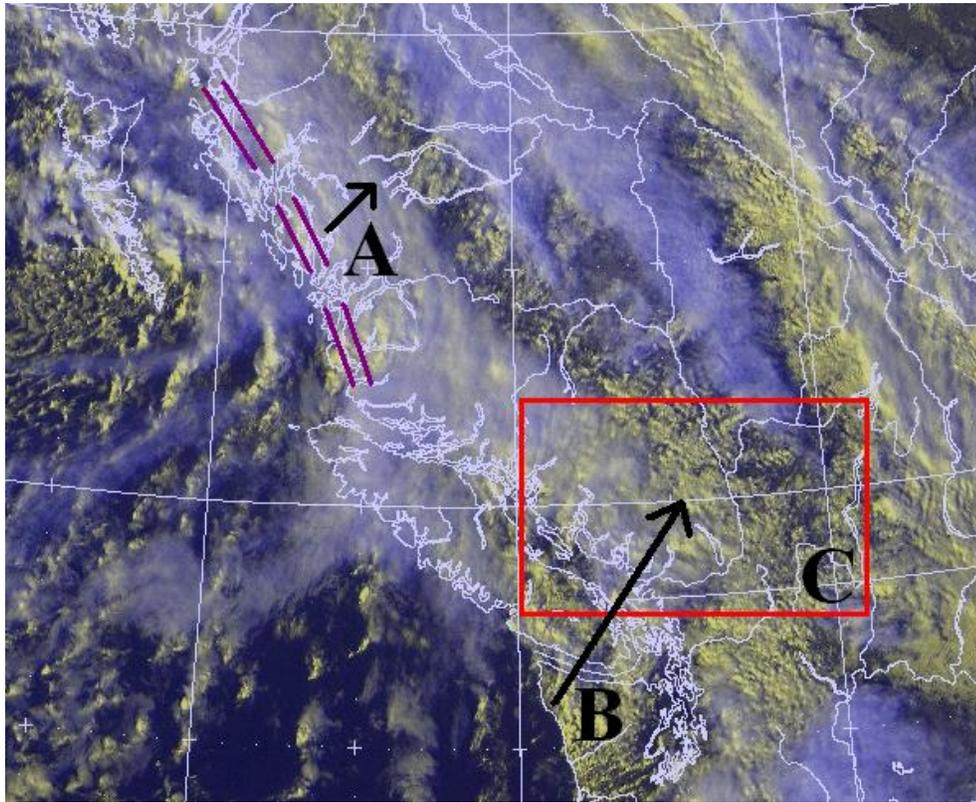
Figure 3.13: Multispectral visible satellite imagery for southwestern BC for 1530 PST 24 Feb 2010 (courtesy of EC). Labels highlight A: east-northeastward movement of a shortwave trough, B: large-scale southwesterly onshore flow over the South Coast, and C: lee wave cloud pattern over southwestern BC. All features were derived from a sequence of satellite images.

Webcam images illustrate the overcast conditions reported by the observer at VOC (Fig. 3.14a), with a break in the cloud at mid level and overcast conditions above the mountain (Fig. 3.14b). A persistent southerly push of marine stratus up Howe Sound with additional help from lee wave subsidence in capping the cloud kept boundary layer conditions in Whistler moist. Wind data collected from the OAN weather stations observed southerly up-valley winds through Squamish and Whistler Valley with light upslope winds measured at VOT, VOB and VOL helping to sustain the mid-mountain cloud until 1330 PST.
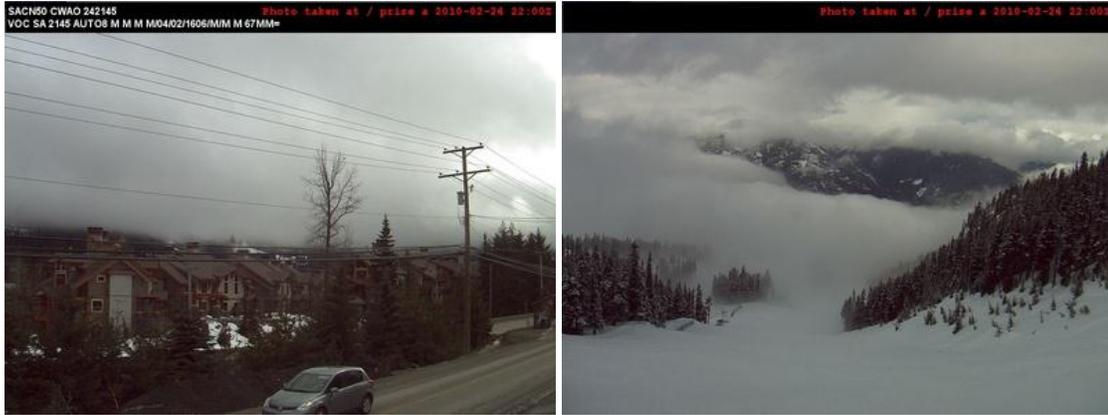
Figure 3.14: Webcam images (courtesy of EC) for 1400 PST 24 Feb 2010 taken from a) VOC (looking up towards Whistler Mountain), and b) the top of the Men's downhill course (looking down and westwards towards Whistler Valley).

From 1330 PST onwards, southerly flow persisted through the Squamish and Whistler Valleys, and upslope (westerly) winds at VOL were maintained. At VOT, however, a wind shift was observed where winds on the lower-mountain reversed direction becoming downslope (easterly) for the rest of the afternoon. Precipitation over the middle of the valley from Harvey's Cloud had ceased by noon, but measurable localized precipitation over Whistler Mountain was observed late in the afternoon. At this time SA below UBC3 became cooler than the FA at the same elevation over the middle of the valley, most likely due to precipitation-induced diabatic cooling (Fig. 3.15). The cooled SA began to sink giving light downslope winds. Reversal of mountain slope winds due to precipitation-induced diabatic cooling was also documented in Steiner et al. (2003).
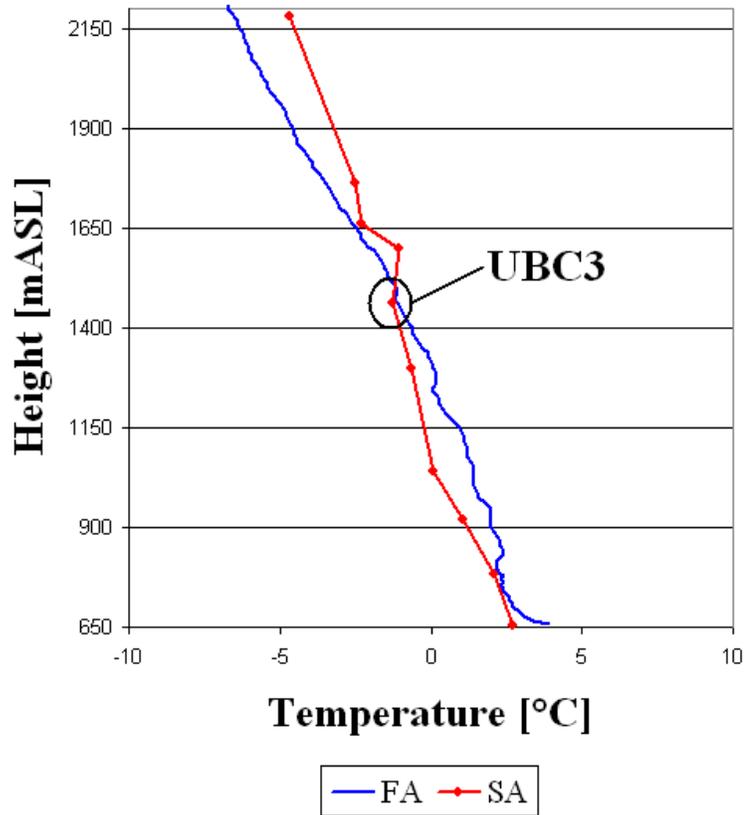
Figure 3.15: FA (blue) and SA (red) profiles for 1515 PST 24 Feb 2010. UBC3 highlighted to mark the transition of warmer SA relative to FA, to cooler SA.

This is also supported by time-heights of SA relative humidity (Fig. 3.16). Note the dry layer that develops above the mid-mountain cloud by 1000 PST. Mo et al. (2011) provide a detailed explanation of how the development of this dry layer can act as an indicator of lee wave subsidence, trapping the mid-mountain cloud below.
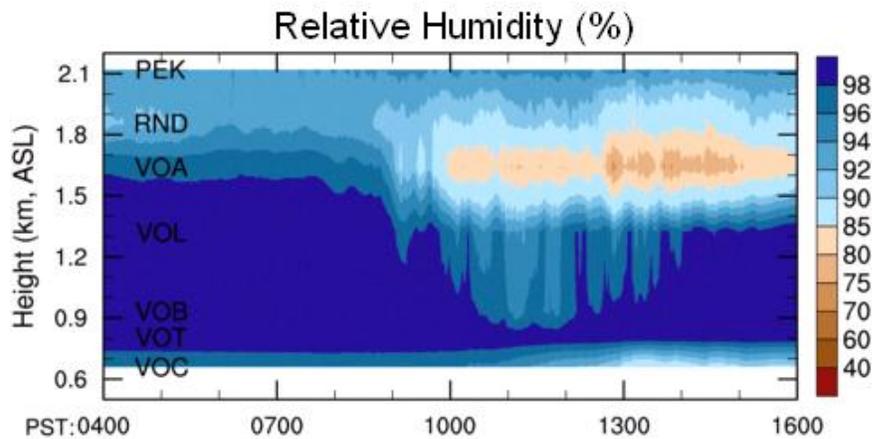
Figure 3.16: Time-height diagram of relative humidity for 24 Feb 2010 using data collected from OAN autostations VOC, VOT, VOB, VOL, VOA, RND, and PEK (figure courtesy of Paul Joe, EC).

For cloudy type A, there were a total of six profiles showing similar temperature profile characteristics to Fig. 3.15. Four of these cases coincide with Harvey's Cloud events presented by Mo et al. (2011) and the lower mountain wind reversal presented here. If the Harvey's Cloud cases are removed from the cloudy type A dataset, SA-FA temperature differences for the slope portion of the profile average 0.65°C. This is greater than the 0.53°C difference for cloudy type B profiles, as was originally expected. By eliminating cases where the effects of Harvey's Cloud influence lower portions of the profile, one is left with regular mid-level overcast conditions, where slope temperatures are dominated by diffuse insolation. Arithmetic means are highly sensitive to outliers (Crawley, 2005), averaging these two entirely different phenomena should be avoided.

Valley

Daytime valley-level (654 mASL) SA-FA temperature differences are -0.5°C and -0.29°C for cloudy type A and B, respectively (Fig. 3.11). Under cloudy conditions, shortwave energy is reflected, scattered and to a lesser extent, absorbed by clouds reducing the amount of shortwave radiation that reaches the surface. This is evidenced by the smaller temperature differences across the valley floor as compared to sunny sky conditions (1.14°C). As expected, smaller temperature differences are associated with the stormier cloudy type B conditions.

3.3.3 Nighttime Temperature Differences for Summit, Slope and Valley

Summit

The average summit-level (2180 mASL) SA-FA temperature differences for cloudy nighttime profiles are 1.81°C and 0.86°C for type A and B, respectively (Fig. 3.11). These relatively small differences confirm the postulate that locations that are more susceptible to clouds and/or wind, such as mountain summits, should have SA temperatures that are closely related to FA temperatures (as proposed by, e.g., Pepin and Lundquist, 2008). However, the positive nighttime temperature differences are at odds with studies performed on various mountaintops around the world (e.g., Pepin and Norris, 2005). For instance, Richner and Philips (1984) found that on average the summit-level SA-FA temperature difference at 0400 LST was approximately -1.9°C. For days with cloud cover greater than 8/10, Peppler (1931) found early morning summit-level SA-FA temperature differences of -1.6–-0.3°C, with the highest amounts of cloud cover producing the smallest difference.

Examining all cloudy nighttime profiles (not shown), the summit-level SA-FA differences for type A ranged from 1.03–3.31°C, while for type B, values ranged from 0.16–1.88°C. Hence, summit-level SA temperatures are always warmer than the adjacent FA under all nighttime, cloudy conditions, in contrast with findings from the previous studies listed above (also compare to Fig. 3.3). Of these profiles, there were more anomalously warm summit temperatures (SA-FA difference of >2.5°C) in cloudy type A profiles (33%) than type B (17%), as in the daytime profiles above. The anomalous summit-level temperatures in all cloud categories suggest that proper sensor placement is crucial for obtaining representative temperature data. Specifically, close proximity to heat sources (e.g., buildings, vents, etc.) should be avoided.

Slope

During the night, SA is predominantly colder than the adjacent FA for both type A and B through the slope portion of the profile (VOT [782 mASL] to UBC1 [1763 mASL]). Type A temperature differences average -0.53°C, while the saturated, well-mixed type B profiles give an average temperature difference of -0.22°C (Fig. 3.11). There are numerous cases where cloudy

type B SA and FA profiles directly overlap, whereas the majority of type A profiles exhibit large SA-FA differences (e.g., Fig. 3.17). During cloudy type B nights, clouds and wind both limit radiative surface cooling and keep the valley atmosphere well-mixed, practically eliminating the SA-FA temperature differences.
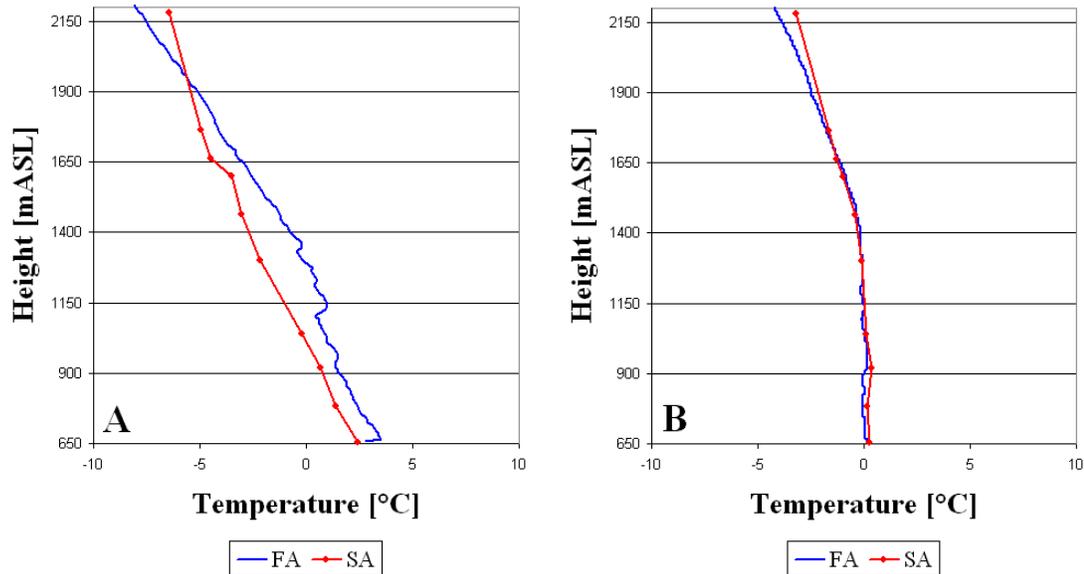
Figure 3.17: Examples of FA (blue) and SA (red) profiles obtained at 0315 PST for a) cloudy type A on 17 Mar 2010, and b) cloudy type B on 23 Feb 2009.

The average temperature differences for cloudy type A and B (-0.22 and -0.53°C, respectively) are much smaller than those for clear nights (-0.90 and -2.64°C, respectively; cf. Figs. 3.11, 3.3). This is because cloud cover counteracts nighttime radiative cooling through downward longwave radiation, which in turn reduces cold air drainage (Whiteman, 2000; Pepin and Norris, 2005). The downward longwave radiation from clouds increases as cloud base temperature increases (Oke, 1978). Thus, low-level stratus layers contribute more energy to the slope than mid- to high-level clouds. Likewise, greater cloud cover amounts absorb and emit more downward longwave radiation, allowing less surface-based outgoing longwave radiation to escape to space (Liou, 2002). Peppler (1931) observed this as well, finding that as cloud cover increased, temperature differences decreased. Additional mixing caused by strong southwesterly flow up Howe Sound as synoptic systems pass over Whistler further reduces SA-FA differences.

Valley

Lastly, valley-level (654 mASL) nighttime cloudy type A and B SA-FA differences are 0.42°C and 0.36°C, respectively (Fig. 3.11). This illustrates the small, but noticeable differences that occur between SA and the shallow, relatively isothermal surface-based layer in the middle of the valley. There is no evidence of cold air pooling at the bottom of the slope; the near-constant SA lapse rate (Fig. 3.9) extends to valley bottom.

The presence of extensive cloud cover significantly reduces the net longwave radiation lost from the slope, reducing the SA-FA differences. Buoyancy differences are weaker, inhibiting cold air drainage, and thus, only a very shallow stable layer forms at VOC. This local depression amongst an undulating valley floor can impact the local heat budget (Haiden and Whiteman, 2005), giving rise to subtle temperature differences across Whistler Valley. Clear sky conditions, by contrast, generated a strong surface-based inversion with SA-FA differences of 2.23°C.

3.3.4 Case Study: Diurnal Temperature Evolution for Type B Cloudy Skies

At 1515 PST on 10 Feb 2010 a trowal extended from Oregon, up towards the Haida Gwaii off the North Coast of BC, bringing precipitation to Whistler. As the trowal moved eastward, it was quickly followed by a second low pressure system and its associated warm front, which passed through Whistler shortly after 1000 PST 11 Feb (Fig. 3.18a). As 11 Feb progressed, precipitation began as a rain-snow mix in the valley bottom, switching over to rain near noon. Freezing levels rose from 900 mASL at 0915 PST to 1300 mASL at 1515 PST, with a near-freezing layer extending up to 1600 mASL.

Looking at cloud cover evolution over the 24-h time period, the overcast cloud layer hovered between 2060–2334 mASL, with lower scattered-broken layers at approximately 1206 mASL. Satellite analyses revealed broken layers of high cloud associated with the trowal persisting over the Whistler region until 1700 PST 10 Feb. As the high cloud moved eastward, a band of low-

mid level cloud lingered on the Coast Mountains in the unstable onshore flow until the second low arrived. By 0430 PST 11 Feb, thick warm-frontal cloud dominated southwest BC and persisted for the remainder of the period (Fig. 3.18b).
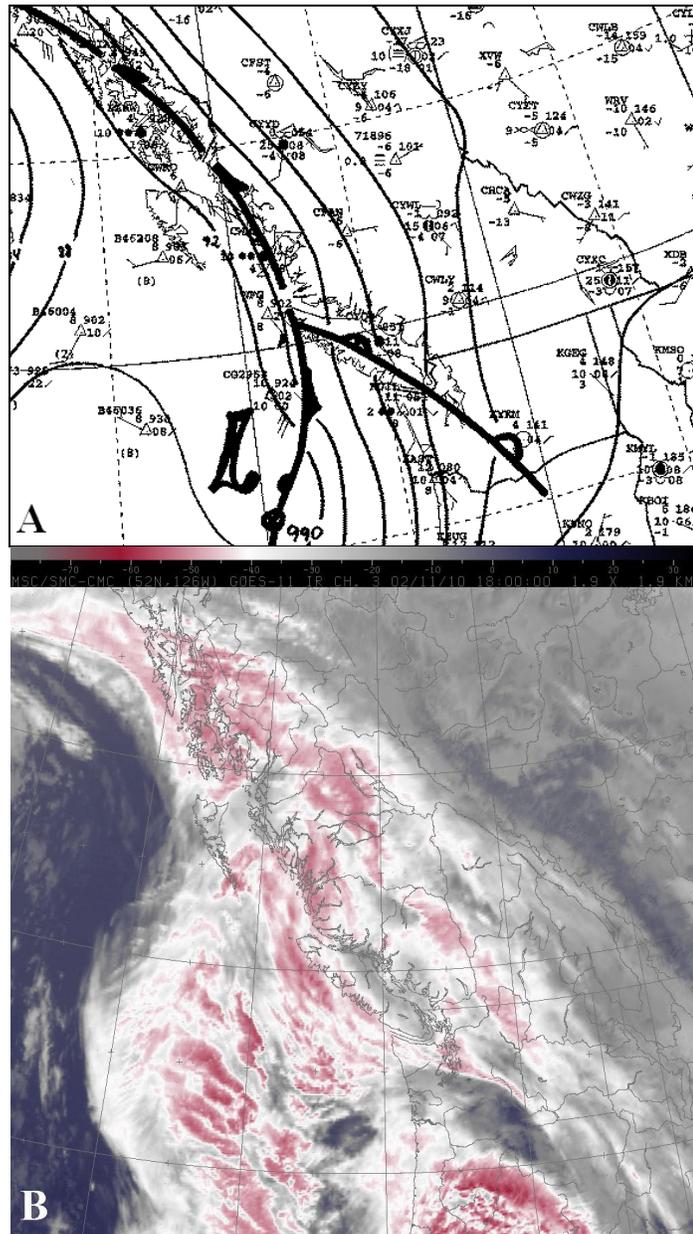
Figure 3.18: (a) Surface analysis, and (b) infrared-redtop satellite imagery over southwestern BC for 1000 PST 11 Feb 2010 (courtesy of EC). The surface map has sea level pressure contoured every 4 hPa, and fronts and trowals are analyzed with traditional symbols. Frontal positions were determined using all available data including surface observations, radar, and animation of infrared, visible and water vapour satellite imagery. Darker red colours on the infrared image denote colder cloud tops.

The largest overall cooling rates are found in the SA from 1515–2115 PST 10 Feb [1.7°C (6 h)$^{-1}$ on average] (Fig. 3.19), but very small cooling rates occur in the FA [0.4°C (6 h)$^{-1}$ on average], with the exception of the valley-level. The valley-level FA cooling [1.9°C (6 h)$^{-1}$] is much smaller than that of the clear sky case study in section 3.2.4 [9.2°C (6 h)$^{-1}$], and clearly illustrates the limiting effect of cloudy frontal conditions on radiative cooling and cold air drainage. During this period of limited cooling, the SA becomes colder than the FA, and a shallow isothermal layer forms in the FA at valley bottom.
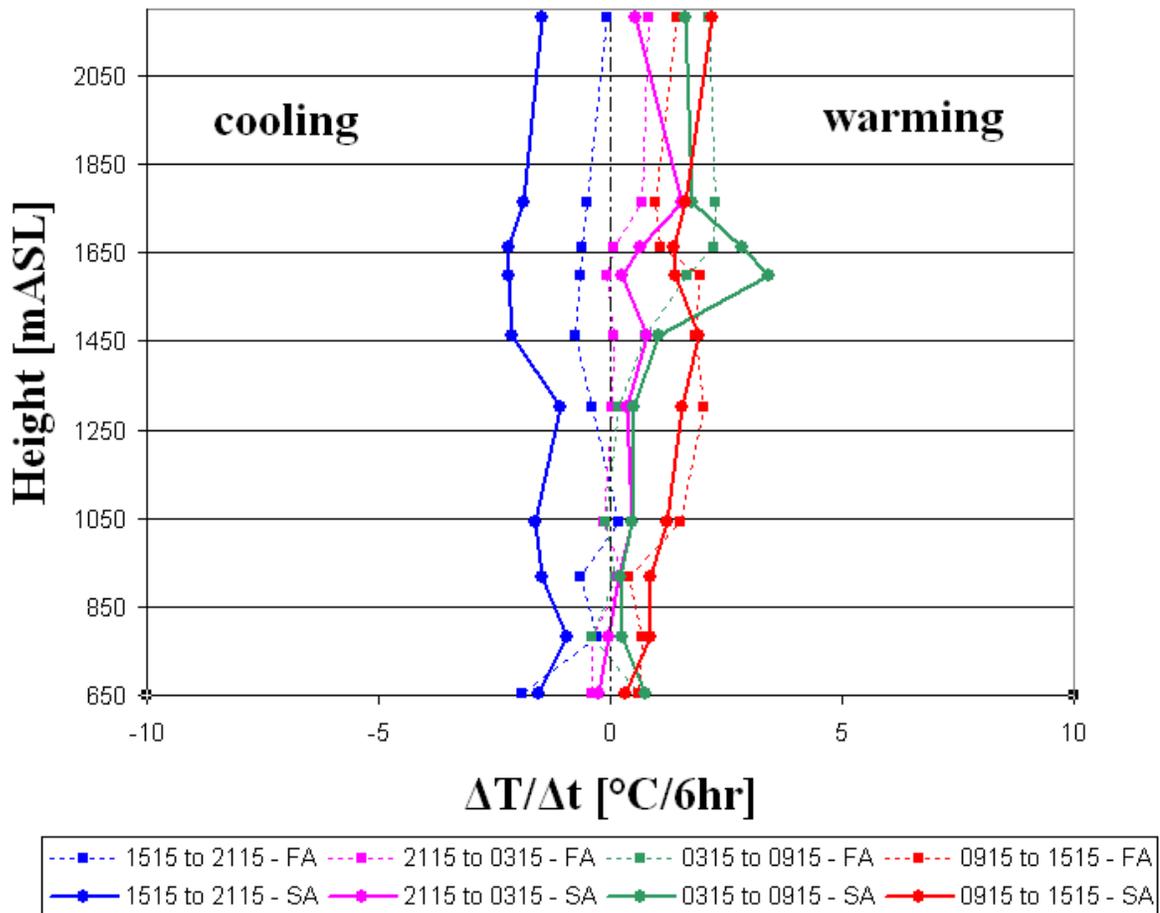
Figure 3.19: 6-h temperature changes under cloudy sky conditions for SA (solid, circles) and FA (dashed, squares) over time periods denoted during 10–11 Feb 2010.

From 2115 PST 10 Feb to 0315 PST 11 Feb (Fig. 3.19), there are negligible changes for much of the SA and FA profiles [averaging 0.3°C (6 h)$^{-1}$ and -0.07°C (6 h)$^{-1}$, respectively]. The exception is slight warming at the upper two elevations in the SA and FA [averaging 1.0°C (6 h)$^{-1}$ and 0.7°C (6 h)$^{-1}$, respectively]. A significant warm air intrusion aloft (>1450 mASL) associated with the warm front is observed in the third time period (0315–0915 PST 11 Feb;

58

Fig. 3.19). Below this, SA undergoes a small amount of warming [averaging $0.6°C$ $(6 h)^{-1}$], whereas the FA remains unchanged. This is a fairly common phenomenon in mountainous areas, where the low-level baroclinic structure of a front is stripped off by upstream terrain, leaving the valley atmosphere relatively unchanged (Colle et al., 2002; Steenburgh, 2003; Shafer et al., 2006). The SA becomes warmer than the FA during this period.

The largest warming occurs during the late morning/early afternoon (0915–1515 PST 11 Feb, Fig. 3.19). During this time diffuse solar radiation warms the SA (and in turn the FA), and the mild maritime airmass settles into southwest BC. Mixing due to convective processes and mechanical turbulence has eroded nearly all of the colder valley atmosphere, with the exception of the lowest few hundred metres, where only small warming rates are observed [~$0.8°C$ $(6 h)^{-1}$ for SA and FA] (Fig. 3.19).

This case study has provided insight into the complex interactions between terrain and transient synoptic weather systems, and the resulting evolution of the SA and FA temperature profiles. First, relatively little temperature change occurs in the FA in any portion of the case study. The FA normally has a small diurnal temperature change above 850 hPa (Seidel and Free, 2005), but under cloudy conditions the changes below 850 hPa are just as small. Hence, SA temperature changes predominantly dictate the changes in SA-FA temperature differences. The majority of SA cooling occurs within the first few hours of sunset and is likely caused by the loss of longwave radiation from the surface. The effectiveness of clouds at absorbing this outgoing radiation and re-emitting it back towards the surface is apparent in cloudy-clear sky case study comparisons. The magnitude of cooling taking place in the first 6 h is significantly reduced, and thus much less air drains down-slope towards the valley floor. In this case a shallow (264 m thick), surface-based isothermal layer formed in the FA. Following the initial SA cooling, the valley-level FA reaches equilibrium, and no significant further changes to the FA occur. Initial SA warming results from both daytime heating and synoptic-scale warming from the warm front, on the upper portions of the mountain, with subsequent warming along the entire slope in late-morning/early-afternoon.

3.4 Case studies: Formation and Break Up of Inversions

While much of section 3.2 dealt with averaged characteristics of diurnal surface-based temperature inversions under clear skies, it did not describe the evolution of individual cases. Out of the 55 nights with observations from winter 2009/2010, 53% had surface-based inversions. Here, two case studies are presented describing the formation and break up of a strong, multi-day inversion, a weak inversion, and the synoptic conditions associated with each.

3.4.1 Strong, Multi-day Inversion Case Study

On 19 Feb 2009, a ridge of high pressure began to build over central BC as an upper-level low and its associated cloud cover drifted northwestward away from the southern BC coast. The ridge continued to strengthen over the following 24 h, maintaining stable conditions and clear skies over the southern Coast Mountains (Fig. 3.20). Northeasterly, low-level outflow winds spread through southern sections of Howe Sound. At Whistler, winds recorded over this three-day period at VOH reached their daily maxima, ~13 km hr^{-1}, between 1000–1700 PST, dropping to ~7 km hr^{-1} overnight. Valley bottom (VOC) winds recorded daily maxima of ~6 km hr^{-1} between 1000–1600 PST, becoming quiescent overnight. Clear sky conditions continued until late evening on 21 Feb 2009 when a low moving eastward towards the BC coast brought increasing cloud cover.
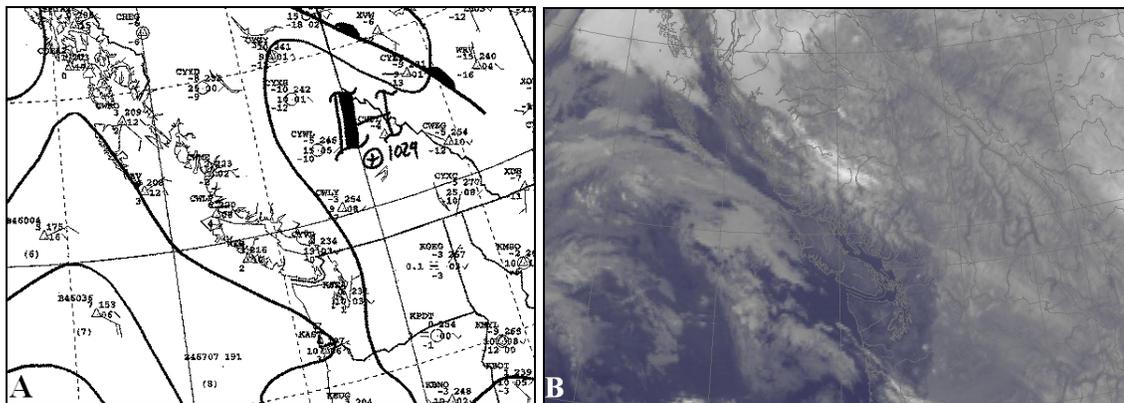
Figure 3.20: (a) Surface analysis and (b) infrared satellite imagery over southern BC at 2200 PST 20 Feb 2009 (courtesy of EC). The surface map has sea level pressure contoured every 4 hPa, and fronts and trowals are analyzed with traditional symbols. Lighter grey colours on the infrared image denotes colder cloud tops.

Calm, cloud-free conditions provided an environment that maximized nighttime net longwave radiation loss from the surface, increasing the strength of the inversion from -10.8°C km^{-1} to -29.7°C km^{-1} for SA, and from -22.0°C km^{-1} to -51.9°C km^{-1} for FA with each successive night from 19–21 Feb (Fig. 3.21). The inversion reached its peak at 0315 PST 21 Feb 2009.
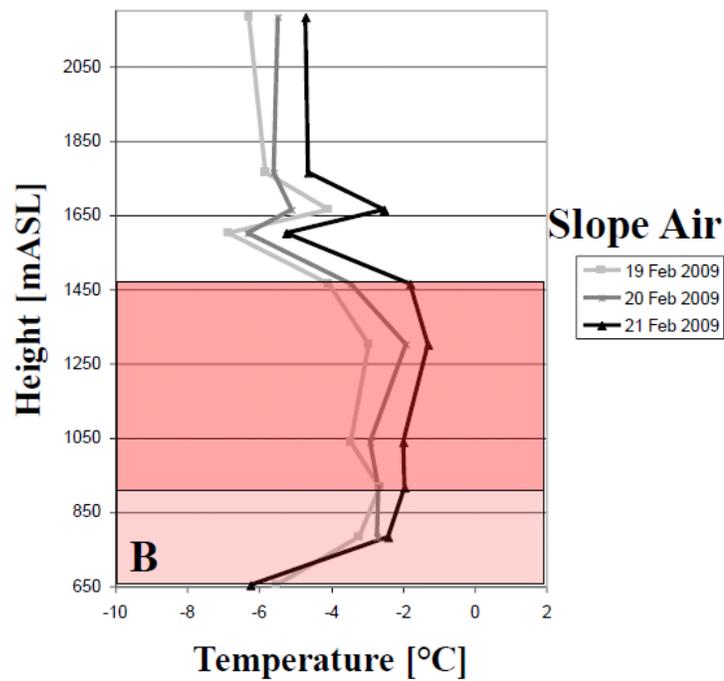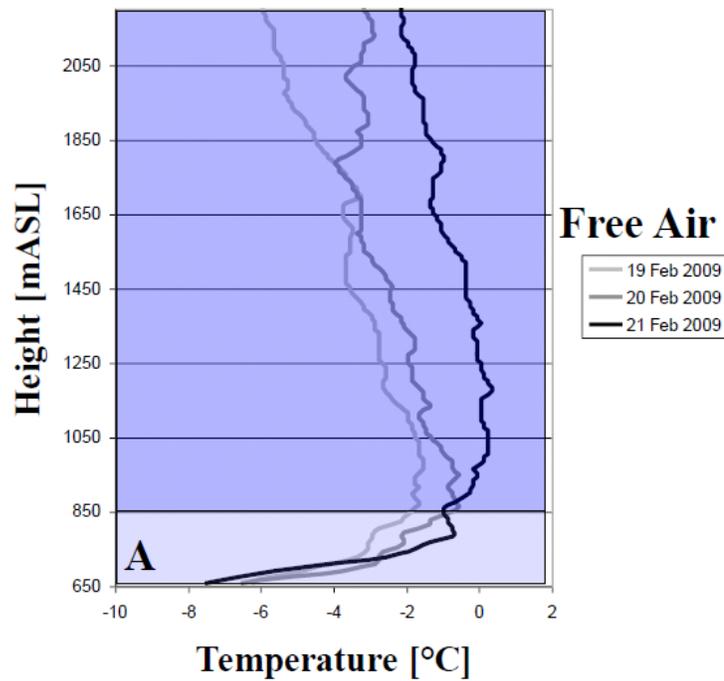
Figure 3.21: Progression of a multi-day temperature inversion in Whistler Valley at 0315 PST on 19–21 Feb 2009 for a) FA and b) SA. Light blue (a) and red (b) shaded areas indicate the average depth of the surface-based inversion. The darker shaded areas highlight the average depth of the stable layer aloft.

Atop the surface-based inversion resided a deep (~680 m for SA, >1380 m for FA) stable layer (Fig. 3.21 dark shaded areas). SA and FA lapse rates in this layer became more stable each night as the synoptic ridge continued to strengthen. The associated adiabatic warming due to subsidence aloft is illustrated in the upper portion of the FA and SA profiles (Fig. 3.21).

Daytime heating from the low winter sun angle was unable to overcome the continuous long wave radiation loss from the snow-covered surface. Thus, with each successive night the surface-based inversion increased in strength (Fig. 3.21). This combined with adiabatic warming at the mid-levels within the valley caused the depth of the daytime stable layer to increase (Fig. 3.22 shaded areas). The resulting daytime temperature structures are significantly different than those observed under *single day* (clear skies lasting no longer than 24 h) clear sky conditions (cf. Figs. 3.1, 3.22b and c). Additionally, a surface-based inversion appears in nighttime SA profiles under a multi-day period of clear skies, a feature that was not found in single day events (cf. Figs. 3.2b, 3.21b).
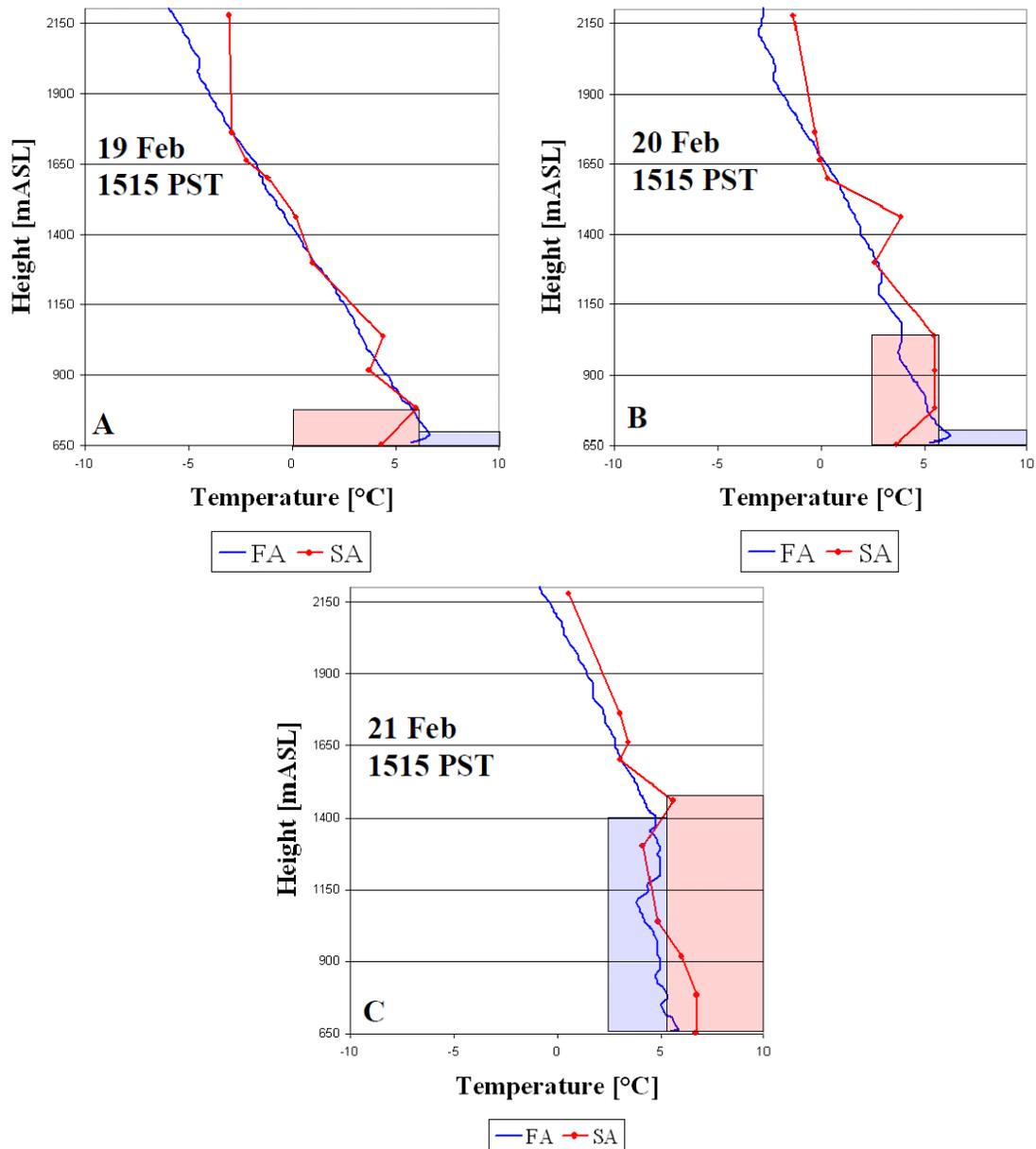
Figure 3.22: Daytime SA (red) and FA (blue) temperature profiles for 1515 PST on a) 19, b) 20, and c) 21 Feb 2009. The shaded areas (red for SA, blue for FA) indicate the increasing depth of the stable layer (inclusive of any surface-based inversion) with each successive day.

A change in the overlying synoptic conditions from an approaching low aided in the break up of the surface inversion at approximately 1200 PST 21 Feb. In the hours following (1200–1600 PST), a residual inversion layer (~1300–1462 mASL) persisted aloft (not shown). A nearly identical evolution was observed during the continuous clear sky period of 18–21 Feb 2010.

Insufficient daytime heating and resultant weakened convection during winter are commonly linked to persistent inversions (Whiteman et al., 2001). Inversions may strengthen further via

warm air advection aloft, low-level cold air advection (e.g., Arctic air intrusions), or warming aloft due to subsidence from a high pressure centre (Zhong et al., 2001). As shown above (Fig. 3.21), inversions continually strengthen under these multi-day clear sky conditions. Despite significant warming aloft, minimal change in surface temperature occurs between nights (e.g., -6.3°C–-7.5°C for FA, -5.5°C–-6.2°C for SA from 19–21 Feb 2009). Likewise, there is little change in the daytime low-level temperature structure and surface temperatures (e.g., 5.7–5.4°C for FA, 4.3–3.7°C for SA from 19–20 Feb 2009). With most cities and towns located in valley bottoms, persistence forecasting of nighttime low and daytime high temperatures is expected to work well under these conditions. The break up of persistent inversions often requires a change in synoptic conditions. Forecasting if and when sufficient conditions for break up will occur is difficult (Smith et al., 1997), and due to the large vertical temperature gradient involved, can lead to large forecast errors.

The forecasting of daily temperature inversion formation in Whistler Valley is easier, simply requiring satellite interpretation of cloud cover and the use of prognostic models to determine whether clear sky conditions will prevail throughout the night. Additionally, these inversions are usually foreshadowed by a 1515 PST radiosonde profile featuring a shallow (15–50-m deep) surface-based inversion (e.g., Fig. 3.23a blue shading). This is an indication that ideal radiative cooling conditions are in place. These inversions grow to an average depth of 386-m within the middle of the valley and form a 646-m near-isothermal layer in the SA by 0315 PST (Fig. 3.23b blue and red shading). By late morning, the inversions frequently became distributed over a greater depth as they weaken, sometimes covering the entire depth of the valley (Fig. 3.23c blue shading). These inversions generally dissipate with the help of daytime heating by 1200–1400 PST (not shown).
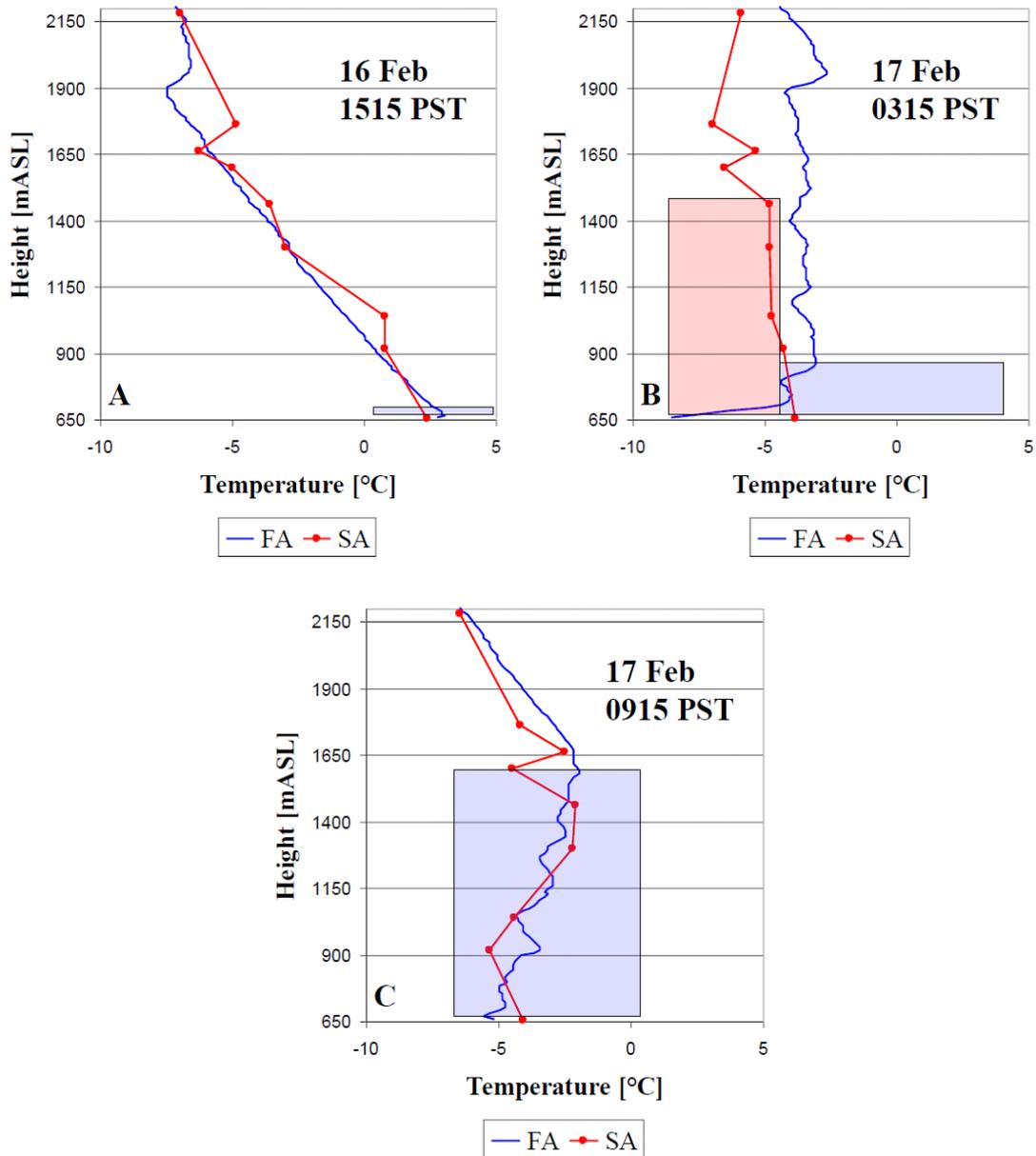
Figure 3.23: FA (blue) and SA (red) temperature profiles showing the evolution of a diurnal temperature inversion for a) 1515 PST 16 Feb, b) 0315 PST 17 Feb, and c) 0915 PST 17 Feb 2009. The depth of the FA inversion is indicated by blue shading and the SA isothermal layer is illustrated by red shading.

3.4.2 Weak Inversion Case Study

Section 3.3 discussed the radiational feedback between the mountain surface and overlying clouds, which inhibits nighttime inversion formation. There were, however, a few cases where despite widespread cloud cover, a surface-based inversion briefly developed. Inversions of this nature were significantly weaker and shorter-lived than their clear sky counterparts, as illustrated in the following example.

Amidst a pattern of storms continually battering BC, a low approached the BC coast from the southwest at 0400 PST 13 Feb 2010. By 1000 PST an intense warm front brought heavy precipitation and strong southeasterly winds, with VOH recording speeds up to 22 km hr^{-1} lasting throughout the day and into the overnight period. The front progressed inland around 0400 PST 14 Feb (Fig. 3.24), and winds at VOH gradually decreased to 7 km hr^{-1} by 0600 PST. Despite the winds on the upper mountain, the sheltered valley bottom saw near-calm conditions (mostly 0–2 km hr^{-1}) over the two-day period. Showers lingered along the coast in the unstable airmass behind the weakening cold front for much of 14 Feb.
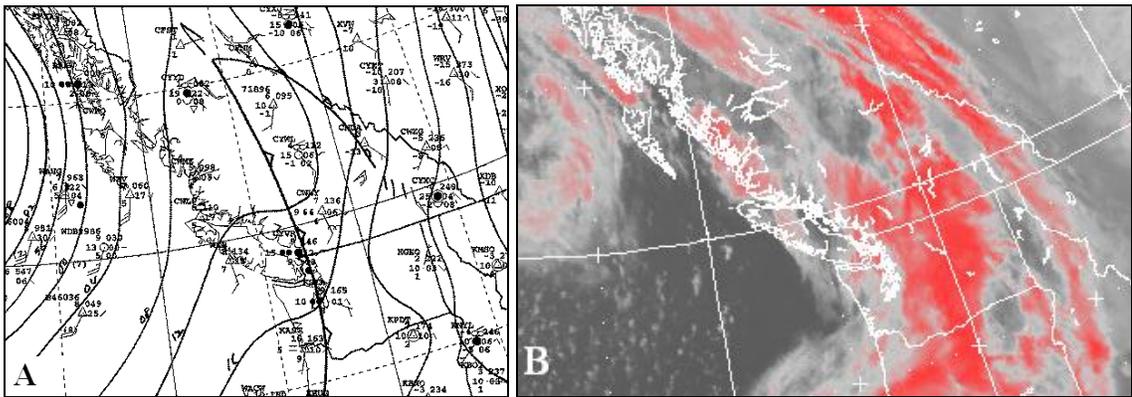
Figure 3.24: (a) Surface analysis and (b) infrared-redtop satellite imagery over southern BC for 0400 PST 14 Feb 2010 (courtesy of EC). The surface map has sea level pressure contoured every 4 hPa, and fronts and trowals are analyzed with traditional symbols. Frontal positions were determined using all available data including surface observations, radar, and animation of infrared, visible and water vapour satellite imagery. Darker red colours on the infrared image denote colder cloud tops.

The passage of this intense frontal band resulted in a well-mixed valley atmosphere with nearly-identical SA and FA temperature profiles (Fig. 3.25a). The saturated (SA RH >96.7% for all stations) conditions produced nearly-moist adiabatic lapse rates. Despite the lingering precipitation early morning on 14 Feb, quiescent valley-bottom winds allowed the formation of a shallow, surface-based inversion within the FA (Fig. 3.25b).
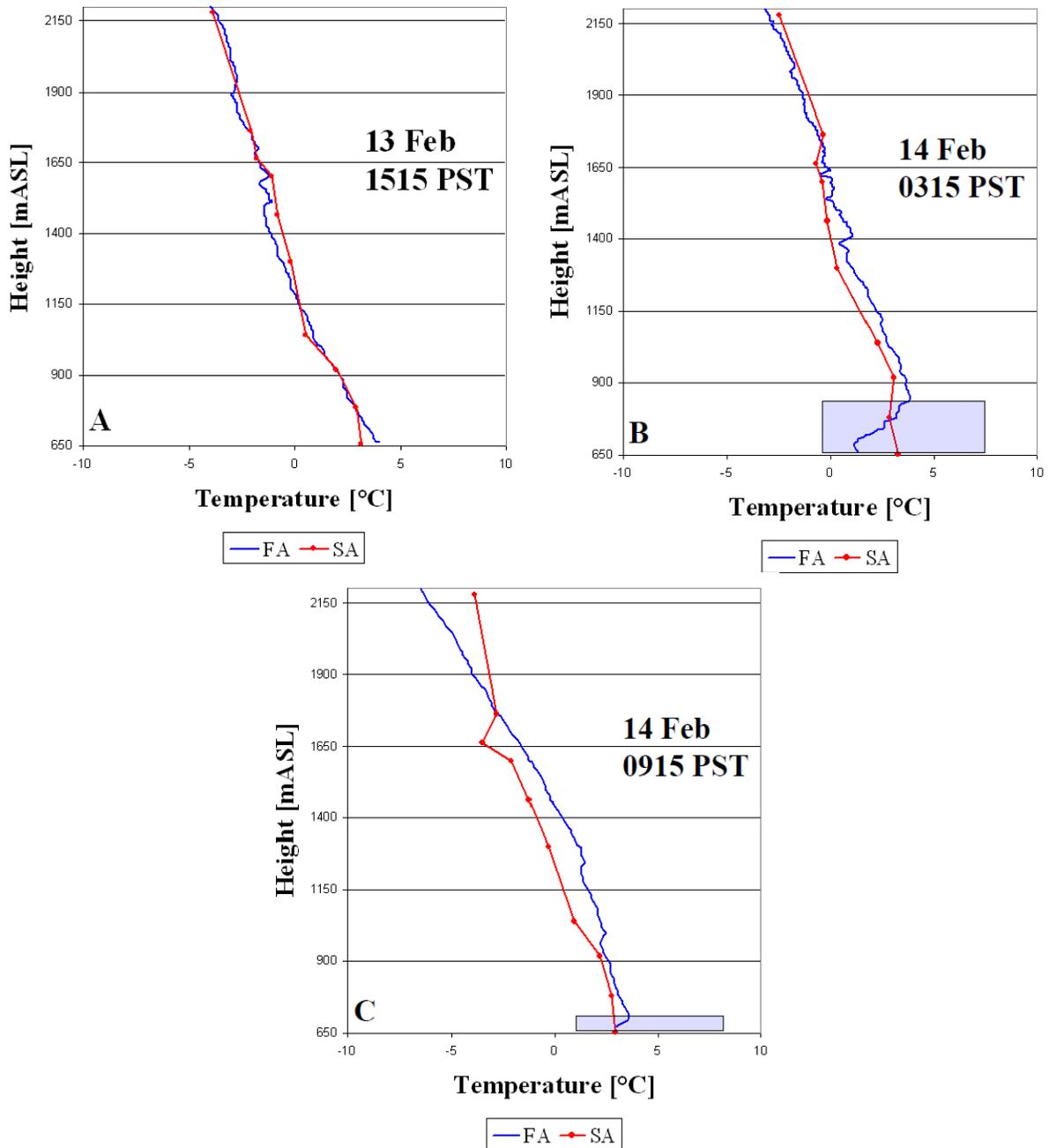
Figure 3.25: SA (red) and FA (blue) temperature profiles from a) 1515 PST 13 Feb, b) 0315 PST 14 Feb, and c) 0915 PST 14 Feb 2010. Blue shaded areas indicate the depth of the FA surface-based inversion.

Forecasting the formation of inversions under cloudy skies can be more difficult than multi-day or diurnal clear sky inversions as their development is rare, can occur in a very short amount of time, and may even take place in the wake of a passing front. Unlike for clear sky inversions, surface-based, shallow precursor inversions in the previous afternoon's 1515 PST FA profile (e.g., Fig. 3.25a) tended to be absent. If a cloudy sky inversion forms overnight (e.g., Fig. 3.25b

blue shading) they tend to become weaker and shallower (50–100-m deep) until 0915 PST (e.g., Fig. 3.25c blue shading), deteriorating rapidly by 1100 PST (not shown). In addition to potentially large low temperature forecast errors, predicting the correct precipitation type when an inversion is present can be problematic. Further research is needed to investigate how inversions form under these conditions.

3.5 Chapter Summary

Co-located SA and FA data presented in this chapter provided a unique, comprehensive view of temperature structure and evolution in Whistler Valley under varying conditions of cloud cover. Grouping profiles by CCH and time of day resulted in a robust means of categorization whereby profiles showed consistent lapse rates over two consecutive winter seasons.

Under clear sky daytime conditions all FA profiles display an extremely consistent, linear temperature structure. The shape of the coinciding SA profiles was relatively non-linear due to local microclimate effects. The average lapse rate of the SA profiles, however, was consistent, allowing for a fairly representative linear SA mean lapse rate. Due to statistical similarities, FA and SA data were combined, and a representative mean lapse rate of $8.26°C$ km^{-1} was calculated. Given the consistency of SA and FA profiles over the observational period, these lapse rates can be used to estimate temperature at any height on the slope or in the valley atmosphere during winter under most clear sky conditions. The SA is warmer than the FA during the daytime, in agreement with previous studies (e.g., Whiteman, 2000; Barry, 2008). However, SA-FA temperature differences are smaller than in other studies (e.g., McCutchan, 1983) likely due to the shortened day light hours, low solar angles, and the high albedo of the snow-covered slopes in this study.

At night under clear skies, surface-based inversions develop within the FA, with an average depth of 386 m and a lapse rate of $-9.48°C$ km^{-1}. By contrast, in the SA a predominantly isothermal temperature profile (lapse rate of $0.40C°$ km^{-1}) forms up to 1300 mASL. The SA-FA temperature differences arise from net longwave radiation loss at the slope surface predominantly within the first few hours of sunset, and subsequently from cold air drainage. At

the summit level, this surface-based stable layer may temporarily mask large-scale subsidence warming until daytime heating can destabilize and erode this surface layer. At lower elevations the SA is colder than the FA, but these temperature differences are smaller in the bottom half of the valley where cold air pools. This horizontally near-homogeneous temperature structure within the valley-bottom cold pool has been observed in enclosed alpine basins (Whiteman et al., 2004), but was an unexpected finding for this unenclosed valley.

Case studies described the strong, persistent inversions that can form over a multi-day period of clear sky conditions, and the rare, weak inversions that can develop under cloudy skies. Under a persistent ridge, surface-based inversions can strengthen and grow to cover the entire depth of the valley. This occurs through synoptically-driven day-to-day subsidence warming throughout most of the profile, and relatively small day-to-day surface-based cooling. A change in the synoptic conditions (i.e., break down of the ridge) is often necessary to eliminate multi-day inversions. Alternatively, cloudy sky weak inversions can be much more difficult to predict as they are quite rare. Fortunately, these events are short-lived and much shallower than under clear sky conditions.

The diurnal clear sky case study indicates that most SA warming occurs well after sunrise, while the majority of cooling occurs within the first six hours of sunset. After this initial nighttime cooling, an equilibrium is reached between the SA and FA whereby further near-surface cooling is redistributed by slope/valley circulations. Although the magnitude of warming/cooling decreased significantly for the cloudy night diurnal case study, the trends were similar. For both sky conditions, changes in SA temperatures account for the vast majority of changes in SA-FA temperature differences.

Cloudy day and night profiles were divided into types A (pre-/post-frontal) and B (frontal), and compared to clear sky conditions. The daytime and nighttime lapse rates were statistically similar (with the exception of the FA for daytime type A) and thus those datasets were combined. This simplified the analysis leaving statistically significant lapse rates of $7.64°C$ km^{-1} for FA daytime type A, $5.63°C$ km^{-1} for the remaining FA/SA type A categories, and $4.32°C$ km^{-1} for FA/SA type B. The reduction in lapse rates from type A to B was mirrored in the SA-FA temperature differences. The only exception was during episodes of Harvey's Cloud where

localized precipitation-induced diabatic cooling produced cooler SA on the lower half of the mountain during the day.

At night, cloud cover for types A and B inhibited the formation of a surface-based inversion. The nighttime SA-FA temperature differences (-0.53°C for type A, -0.22°C for type B) are not only smaller than their daytime counterparts, but they are also much smaller than clear sky nighttime conditions (-0.90°C within inversion, -2.64°C above inversion). While Whiteman et al. (2004) postulated that under clear sky conditions SA and FA profiles within the surface-based inversion act as good proxies for each other, these results show that under cloudy conditions the entire SA and FA profiles can serve as proxies for each other.

Numerous instances of anomalously warm summit-level SA temperatures were observed throughout this study, which emphasizes the importance of careful site selection when installing instruments and the difficulties that arise from taking measurements in such an exposed location. The true magnitude of summit-level SA-FA temperature differences was not ascertainable, a common problem in previous studies (refer to Barry, 2008 for a complete review).

Lastly, this study illustrates that clouds help create a smoother SA temperature profile; one that is less subject to microclimates and perhaps more representative of temperatures at a given elevation. Likewise, SA-FA temperature differences are much more uniform along the entire slope. While the impacts of cloud cover on local heat budgets have been reported by numerous studies (e.g., Samson, 1965; Richner and Philips, 1984; Peppler, 1931), this is the first time, to the author's knowledge, that such linearity in SA temperatures and a consistent SA lapse rate has been shown.

Chapter 4

A Diagnostic Model for Constructing SA and FA Temperature Profiles

4.1 Introduction

Now that a clearer understanding of the vertical structure and evolution of temperature within the Valley has been established, along with the robustness of lapse rates under different conditions, this chapter will attempt to employ this knowledge to create a diagnostic tool. First a few metrics are used to quantify SA-FA differences. Next, the lapse rates calculated in Chapter 3 are combined with a linear regression analysis to construct SA and FA temperature profiles based on a single SA or FA temperature at a given elevation (e.g., mid-mountain station, VOL). To this end, SA versus FA temperature scatter plots are examined and discussed, followed by the development of a diagnostic equation for each cloud cover category.

4.2 Linear Regression Analysis

The development of a regression model begins by determining what type of relation exists between SA and FA temperatures using scatter plots (i.e., linear or nonlinear). Data from only the *slope* portion of the temperature profiles are used; temperature data at the UBC5 (valley) elevation are irrelevant as they are technically not FA comparisons to SA, but instead two valley surface temperatures, and summit-level data are not included for reasons previously discussed (see sections 3.2 and 3.3).

The strong, linear relation between SA and adjacent FA temperatures is illustrated for clear days (Fig. 4.1a) and cloudy type A nights (Fig. 4.1b). Refer to Appendix D for results from all cloud cover categories.
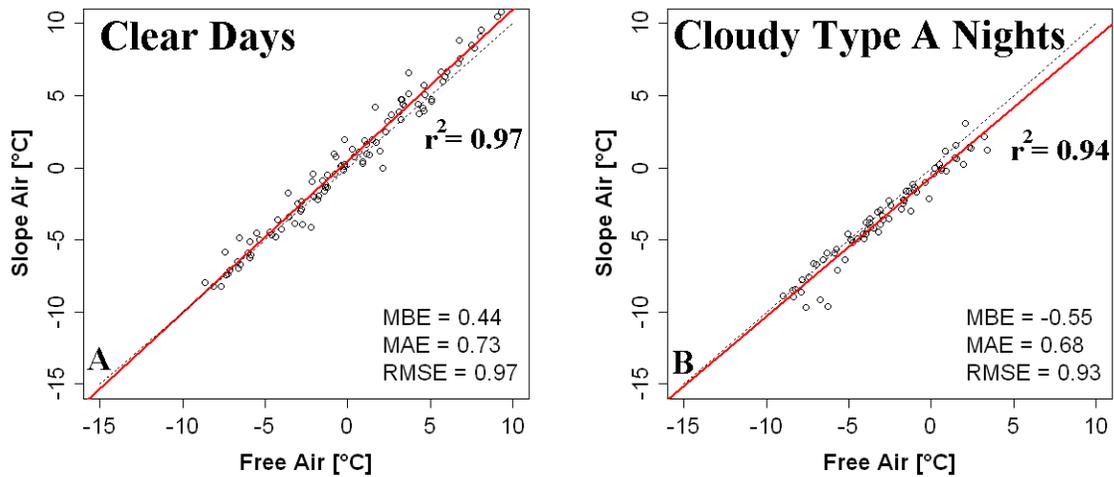
Figure 4.1: Scatter plots of SA temperature versus FA temperature (open circles) for a) clear days, and b) cloudy type A nights. Two lines are plotted: a reference line with a slope of 1 (black, dotted), and the linear regression model (red, solid). Mean bias error (MBE), mean absolute error (MAE), root mean square error (RMSE), and adjusted-r^2 values are provided (see Appendix E for equations).

The reference line (Fig. 4.1 black dotted line) represents where data points would lie if SA temperatures were identical to the FA. The MBE provides the average bias of SA relative to FA, while the MAE and RMSE are measures of the average SA-FA differences. Data points lying to the right of the reference line are representative of SA temperatures that are cold relative to the FA (negative MBE); while data points to the left represent SA that is warmer than the FA (positive MBE). In Figs. 3.3 and 3.11, averages were used to describe SA-FA temperature differences at each station, but here the scatter plots provide a better illustration of predominantly warmer SA under clear skies at 1515 PST (Fig. 4.1a), and colder SA for cloudy type A (pre-/post-frontal) at 0315 PST (Fig. 4.1b). Out of all the categories, cloudy type B nights had the smallest MBE (-0.22°C; Appendix D), while clear nights (above inversion) had the largest (-2.24°C; Appendix D).

Comparing MAE, and RMSE for all cloud cover categories (Fig. 4.1, and Appendix D), cloudy type B nights have the smallest values (0.43°C and 0.54°C, respectively), while clear nights (above inversion) have the largest (2.24°C and 2.53°C, respectively). Smaller SA-FA differences are expected for windy, cloudy (type B) conditions due to the well-mixed slope-valley atmosphere. The clear night values corroborate the results of section 3.2.3, where larger SA-FA temperature spread occurs above the surface-based inversion due to decoupling of the SA layer from the rest of the valley atmosphere.

Since MAE is a linear scoring rule (equal weight to all temperature differences), and RMSE is quadratic (higher weight to outliers), they can be used together to diagnose the variation in SA-FA temperature differences for each cloud cover category. The greater the difference between MAE and RMSE, the greater the variance in the individual temperature differences of the sample (Neter et al., 1996). The RMSE-MAE difference for cloudy type B nights (0.11°C) is smaller than for clear nights (above inversion, 0.29°C), indicating smaller SA-FA spread variance for cloudy type B nights. A similar assessment for the other categories reveals variances for clear nights (within inversion), cloudy type A days, and cloudy type B days are relatively small (strong SA-FA linear relation), while variances for clear days, and cloudy type A nights are a bit larger (slightly weaker linear relations).

The linear regression models developed to determine the SA temperature from observed FA (radiosonde) temperature at a given reference elevation for each cloud cover category take the following form:

(2) $$T_{SA}(Z_r)_n = a_0 + a_1 T_{FA}(Z_r)_n$$

Where $T_{SA}(Z_r)_n$ is the SA temperature at a reference elevation, Z_r, $T_{FA}(Z_r)_n$ is the FA temperature at that same elevation, a_0 is a constant, a_1 is the regression coefficient, and n is the number of data pairs. Results are displayed in Table 4.1. The linear regression model for clear nights is broken into two distinct equations using the average depth of Whistler Valley FA inversions (SA isothermal layer) to delineate the portions of the temperature profiles within, versus above the inversion (isothermal layer).

Cloud Cover Category	Equation: $T_{SA}(Z_r)=$	Standard Error for	Adjusted-r^2
Clear Days	*0.44 + 1.05 $T_{FA}(Z_r)$*	a_0: 0.08 a_1: 0.02	0.97
Clear Nights (within inversion)	*-1.00 + 0.92 $T_{FA}(Z_r)$*	a_0: 0.10 a_1: 0.04	0.90
Clear Nights (above inversion)	*-2.43 + 0.92 $T_{FA}(Z_r)$*	a_0: 0.18 a_1: 0.05	0.86
Type A Days	*0.45 + 0.96 $T_{FA}(Z_r)$*	a_0: 0.11 a_1: 0.02	0.97
Type A Nights	*-0.65 + 0.96 $T_{FA}(Z_r)$*	a_0: 0.12 a_1: 0.03	0.94
Type B Days	*0.50 + 0.96 $T_{FA}(Z_r)$*	a_0: 0.06 a_1: 0.03	0.91
Type B Nights	*-0.27 + 0.96 $T_{FA}(Z_r)$*	a_0: 0.05 a_1: 0.02	0.96

Table 4.1: Linear regression output from (2) showing constants, coefficients, their associated standard errors, and adjusted-r^2 values for all cloud cover categories. Each equation is statistically significant according to the standard errors.

Multiple linear regression (as opposed to simple linear regression) analysis was then performed in an attempt to improve the fit of the model by incorporating elevation data as a predictor, and took the following form

(3) $$T_{SA}(Z_r)_n = a_0 + a_1 T_{FA}(Z_r)_n + a_2 z$$

Scatter plots of T_{SA} versus z were generated (not shown) to demonstrate the linear relation. While a general decrease of temperature was observed as elevation increased, the overwhelming dominance of T_{FA} as a predictor caused all other terms in the multiple linear regression to be non-significant (Appendix F). A forward step Akaike's Information Criterion confirmed that the simple model (2) was superior to the complex model (3) as the additional parameter did not cause a reduction in deviance of at least 2.0 (Crawley, 2005).

The linear regression models (*Equations* in Table 4.1, also see Fig. 4.1 and Appendix D red lines) represent the lines that minimize the sum of squares of the residuals (Crawley, 2005). Although the linear regression models (Fig. 4.1 and Appendix D red lines) visually seem close to the reference line (Fig. 4.1 and Appendix D black dotted lines), based on the regression coefficient standard errors (Table 4.1), the slopes (a_1) of the linear models are significantly different from 1.

A common measure of fit, r^2, represents the fraction of the total variation in T_{SA} that is explained by the regression equation (Crawley, 2005). However, r^2 will increase as additional data are added, even if the new data do not increase the predictive capabilities (Neter et al., 1996). An alternative measure of fit is *adjusted-r^2* which will only increase if newly added data increase the explanatory capabilities of the model (Neter et al., 1996). The high *adjusted-r^2* values for each cloud cover category indicate that the simple model (2) provides an excellent fit to the data. Therefore, the equations provided in Table 4.1 can be used to determine T_{SA} at a given elevation using T_{FA}, or if (2) is solved for T_{FA}, T_{FA} can be determined given T_{SA}.

4.3 Diagnostic Model for Constructing SA and FA Temperature Profiles

The model used for constructing SA and FA temperature profiles from a single, routine SA or FA temperature measurement consists of two steps. First, for a given elevation, cloud cover category, and SA (FA) temperature, the linear regression models (Table 4.1) are used to determine the corresponding FA (SA) temperature. Next, the results of Chapter 3 illustrated that the temperature profiles within each cloud cover category have consistent, representative lapse rates (summarized in Table 4.2). These lapse rates can be used to construct the complete SA (FA) and FA (SA) temperature profiles using the initial SA (FA) and calculated FA (SA) temperature. A flow chart (Fig. 4.2) depicts this two-step process.

Cloud Cover Category	Lapse Rates [°C km^{-1}]	
	SA	FA
Clear Days	8.26	8.26
Clear Nights (within inversion)	0.40	-9.38
Clear Nights (above inversion)	3.94	3.30
Type A Days	5.63	7.64
Type A Nights	5.63	5.63
Type B Days	4.32	4.32
Type B Nights	4.32	4.32

Table 4.2: Statistically significant SA and FA mean lapse rates for each cloud cover category summarized from Chapter 3 results. The average height of the Whistler Valley inversion (isothermal) layer was used to delineate the within inversion lapse rates from the above inversion lapse rates for FA (SA).
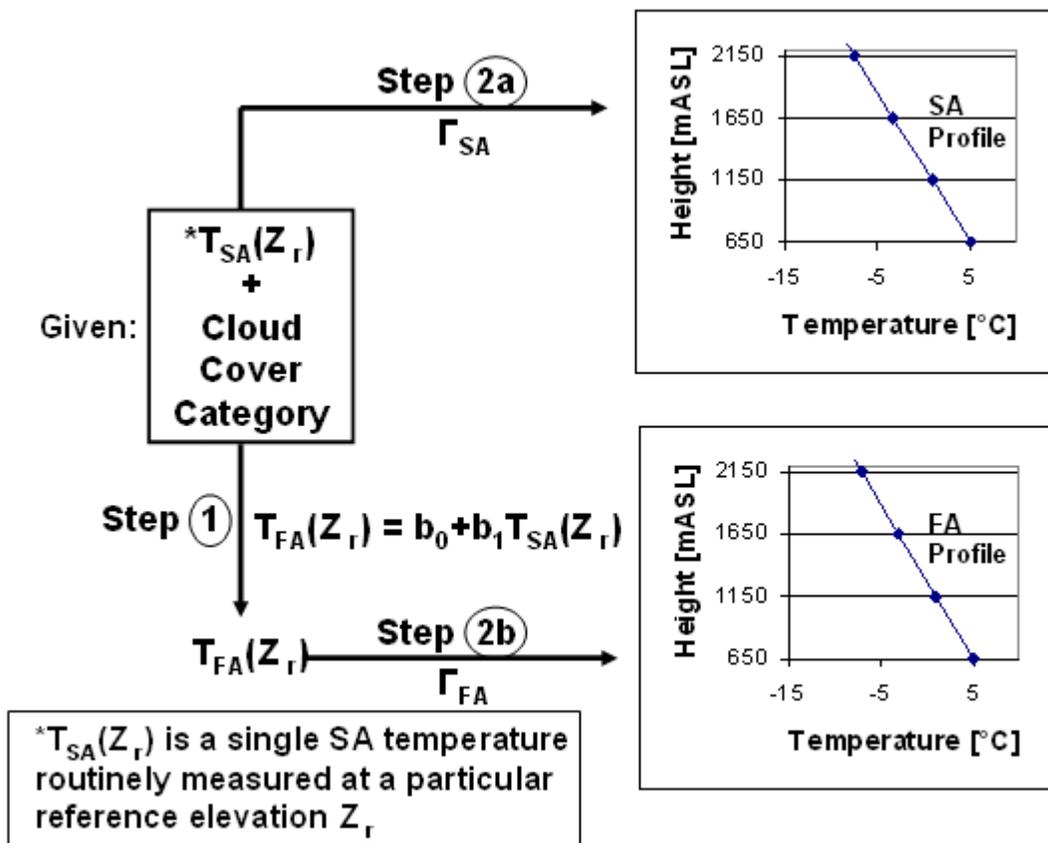
Figure 4.2: Flow chart indicating how a single, routine SA temperature measurement at a given reference elevation (Z_r) can be combined with the linear model equation and lapse rate for a particular cloud cover category to construct the complete SA and FA temperature profiles. Constant (b_0) and coefficient (b_1) are found by re-arranging (2) to solve for T_{FA}. The same can be done given a single FA temperature.

To demonstrate the construction of SA and FA temperature profiles using this model, the appropriate equations and lapse rates are applied to one profile from the 2009/2010 dataset.

Comparisons are then made between the actual versus model temperature profiles. The temperature profile obtained at 0315 PST (nighttime) 9 Feb 2009 (an independent dataset was not available) was classified as cloudy type A, and its observed SA temperature at 1300 mASL (station VOL) was used to initiate calculations (Fig 4.3 black square). This was deemed to be a suitable location as it is not strongly affected by unrepresentative local processes such as localized cold air pooling or rime ice buildup on the sensor.

Following the steps outlined in Fig. 4.2, the nighttime cloudy type A SA lapse rate of 5.63°C km^{-1} (Table 4.2) was applied to the observed temperature at VOL to extrapolate the full SA temperature profile (Fig. 4.3 red line). T_{FA}(*1300 mASL)* was determined by solving the cloudy type A nighttime linear regression equation (Table 4.1) for T_{FA}. Lastly, the corresponding cloudy type A nighttime FA lapse rate of 5.63°C km^{-1} (Table 4.2) was applied to the calculated T_{FA}(*1300 mASL),* and used to extrapolate the FA temperature profile (Fig. 4.3 blue line). Actual FA and SA temperatures (Fig. 4.3 solid circles) observed at 0315 PST 9 Feb 2009 are included to illustrate the exceptional performance of this model. The largest absolute errors for the SA and FA were 0.41°C and 0.55°C, respectively.
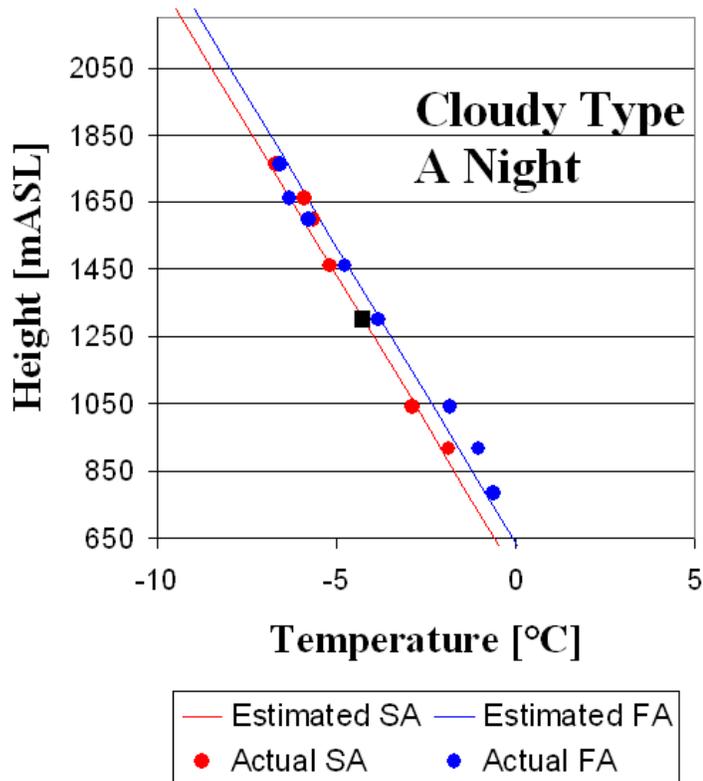
Figure 4.3: Model (lines) and actual (solid circles) temperature profiles for SA (red) and FA (blue) at 0315 PST 9 Feb 2009. The observed temperature at station VOL (black square) was used to initialize calculations.

The construction of clear night SA and FA profiles is more complicated as one has to use the linear equations and corresponding lapse rates for both above the inversion and within the inversion (Tables 4.1 and 4.2). However, if the observed SA or FA temperature used to initialize calculations is above (within) the inversion, the temperature profile above (below) the mean inversion height can be constructed down (up) to the top of the inversion using the above (within) inversion lapse rate. The remainder of the temperature profile is constructed using the within (above) inversion lapse rate from the temperature at the inversion top. Since this process involves using two equations and two lapse rates, each having their own standard errors, the errors will be additive.

4.4 Chapter Summary

After some initial quantification of SA-FA relationships, this chapter concluded by developing a model for constructing SA and FA temperature profiles in Whistler Valley based on a given

cloud cover category and a single SA or FA temperature measurement. The strong diagnostic capabilities of the linear regression equations were substantiated by high adjusted-r^2 values. Error analysis showed that weaker (stronger) linear relations coincided with the larger (smaller) temperature differences and variances. In the model SA and FA temperature profiles constructed in the above example, as well as the error characteristics presented in Table 4.1, the small errors promise substantial improvements over the results found for previous methods used in other mountainous areas across the US and Europe (e.g., McCutchan, 1983; Paul, 1976; Cortemiglia et al., 1989; Carrega, 1995; Furman, 1978).

Chapter 5

Conclusions and Recommendations for Future Research

5.1 Conclusions

Meteorological instrumentation installed by EC for the 2010 Olympic and Paralympic Winter Games was combined with additional UBC temperature sensors to create a high-resolution SA temperature profile along the west slope of Whistler Mountain. This, in conjunction with a three-month (February 2009/2010 and March 2010) FA temperature dataset obtained from the nearby Whistler radiosonde, created an extraordinary opportunity to investigate the relation between SA and FA vertical temperature structure in complex terrain.

In doing so, a new, robust method for categorizing SA and FA temperature profiles by cloud cover was developed. The calculation of CCH established a systematic method for defining clear (<1/3 duration of period) and cloudy (>2/3 duration of period) skies. Further, the use of METAR, combined with supplementary data from satellite and webcams provided a complete picture of the cloud cover that was fed into the CCH equation.

Categorizing SA and FA temperature profiles using CCH gave consistent, repeatable lapse rates for each category across all months. Statistically indistinguishable SA and FA lapse rates were found for each category with the exception of daytime cloudy type A and nighttime clear conditions. These results indicate that under many conditions, the change in temperature with height is independent of its proximity to the west slope of Whistler Mountain. Therefore, inexpensive slope-side temperature sensors and data loggers provide useful proxies for the FA temperature structure and can replace much more expensive, labour-intensive radiosondes under certain conditions.

Cloudy skies prevented nighttime FA inversions or SA isothermal layers from forming, which meant statistically similar daytime and nighttime lapse rates (except for FA type A). Such

findings shed more light on the dampening effects clouds have on diurnal stability fluctuations within the valley-atmosphere.

Despite similar SA and FA lapse rates, there are still significant SA-FA temperature differences whose magnitudes vary between cloud cover categories. Hence, SA and FA temperature profiles are parallel but are not coincident.

Daytime clear sky SA temperature profiles are relatively non-linear due to local effects, a common observation throughout the literature (e.g., Mahrt, 2006). Previous studies' short observational periods, perhaps compounded by their methods of categorization, failed to assemble a collection of consistent temperature profiles, and thus the prevailing wisdom is that SA temperature profiles under clear skies are highly variable both in time and space (Lundquist and Cayan, 2007; Rolland, 2003; Barry, 2008). In this study, however, the vertical temperature structures were consistent within categories, allowing for a fairly representative mean lapse rate to be defined.

Further, this study is the first, to the author's knowledge, to examine the effect of overcast cloud cover on temperature profiles within a mountain valley. The linearity of cloudy daytime and nighttime SA profiles suggests that the linear lapse rate approximations invoked in previous studies (e.g., Martinec and Rango, 1998; Régnière, 1996; Running et al., 1987; Thornton et al., 1997) may work fairly well under cloudy skies. This finding is in disagreement with Harlow et al. (2004), who stated that this simplification induces large errors due to site-specific microclimates. The present study shows that overcast conditions essentially eliminate these microclimates, leading to a consistent, linear lapse rate throughout the entire SA profile.

The magnitude of SA-FA temperature differences is largest for clear skies and smallest for cloudy type B. Changes in SA temperatures accounted for the majority of changes in SA-FA differences. Daytime temperature differences were much smaller than those found in summertime studies over bare ground (e.g., McCutchan, 1983). This can be explained by shortened daylight hours, low solar angles, and the high albedo of the snow-covered surface. SA-FA differences are generally uniform through the slope portion of the profile, while both the summit- and valley-level differences are heavily influenced by local effects on SA temperatures.

During clear nights, the SA-FA temperature difference within the surface-based stable layer is only about a third of what is found above, showing increased horizontal homogeneity near valley bottom. These findings are similar to those of Whiteman et al. (2004) for an enclosed basin. This shows that horizontal homogeneity of surface-based stable layers can be found in both enclosed basins and drained valleys, and thus is encouraging for the applicability of these findings to other valleys and basins.

Linear regression analysis was used to further quantify the link between SA-FA temperatures. Scatter plots illustrated a strong (high adjusted-r^2 values) linear relation, leading to an equation relating SA and FA temperatures for each cloud cover category that provided an excellent fit to the data. This equation allows FA temperature to be determined using SA temperature, and vice versa. The standard errors (0.02–0.18°C) associated with these simple, linear equations are an order of magnitude less than the multiple regression equations found in the literature [e.g., 1.32–1.52°C in McCutchan (1983)]. This suggests that sorting temperature data by CCH greatly strengthens and simplifies the SA to FA relation.

Lastly, a new model was developed that uses a single SA or FA temperature measurement to construct the complete SA and FA temperature profiles for a given cloud cover category. This method offers a substantial improvement to estimating SA and FA temperatures than currently used methods such as monthly mean lapse rates (e.g., Carrega, 1995), persistence-based equations (e.g., Furman, 1978), and correction functions (e.g., Dreiseitl, 1988); all of which fail to describe daily fluctuations in temperature structure.

5.2 Limitations and Recommendations for Future Research

Daytime near-surface air temperatures are predominantly driven by insolation. As even partial cloud cover significantly modifies insolation received locally (Mahrt, 2006), irregular temperature patterns can develop along the slope. Previous investigations have shown strong relations between temperature and either clear or overcast skies (e.g., Barry, 2008; Peppler, 1931), yet data for partly cloudy skies does not fit well between these two extremes (Richner

and Philips, 1984). To maintain a distinction between clear and cloudy conditions, *partly cloudy* sky periods were omitted from this study. Further studies are required to investigate the SA-FA relation under such conditions.

Multi-day clear sky conditions were removed from the clear sky dataset and analyzed separately using case studies. Daytime temperature profiles deviated from the typical near-dry adiabatic, linear structure due to persistent surface-based inversions found in both SA and FA profiles. Nighttime SA profiles showed an uncharacteristic inversion instead of an isothermal layer. Hence, the diagnostic equations developed here will not work as well under these conditions.

The diagnostic model presented in this work represents a new approach to understanding and quantifying the strong relation between SA and FA temperatures. Categorizing profiles by CCH has shown repeatable results across two winter seasons in Whistler Valley. Future work should test this method in other mountainous areas to determine its transferability to areas outside Whistler Valley.

When constructing SA and FA temperature profiles using the linear regression model, it is recommended that the initial SA or FA temperature measurements be obtained from a representative mid-mountain site (see Appendix C). A summit-level consistent SA-FA relation has not yet been found in the literature (Barry, 2008), and valley-level areas are highly susceptible to local cold air pooling and must also be avoided. Using data from either of these locations to initialize calculations could lead to less accurate temperature profiles.

This work has several relevant applications to forecasting, and hydrological models in complex terrain. Dynamic forecasting models often do a poor job of simulating the details of boundary layer temperature structure (e.g., Price and Bush, 2004), especially within mountain valleys (Zhong and Fast, 2003; Reeves et al., 2011). Further, in many cases model terrain is too coarse to resolve the full depth of the valley bottom. This is usually the most crucial elevation to forecast for, as this is where population centres and agriculture tend to be located. To alleviate this issue, one could use a dynamical model forecast for a single point within the valley where the model's skill is highest, and then use this diagnostic model to construct complete SA and FA

profiles. The resulting improved temperature and precipitation type forecasts would have a wide range of benefits.

Another important application of this research is snow melt modeling. Over 90% of BC Hydro's power is derived from hydroelectricity, including that from the Cheakamus River Basin in which Whistler is located. Replacing the current methods for approximating SA vertical temperature structure with those described here has the potential to greatly reduce temperature errors, improving the timing and magnitude of runoff. Increased forecast accuracy ultimately reduces operating costs, saving money for BC Hydro and its customers (McCollor and Stull, 2009).

In closing, the work presented here fills a gap between previous studies employing short-term field studies with high observational density, and others that used longer periods of study but lower observational density. As such, this research is uniquely situated to provide findings that are both temporally and spatially robust. This paper adds to our growing understanding of the structure and evolution of temperature in mountain valleys, while also contributing a valuable tool for accurately constructing SA and FA profiles from a limited amount of information.

References

ACIA, 2005. Arctic Climate Impact Assessment. Cambridge University Press: Cambridge, UK.

Aguado, E., and J. E. Burt, 2009. Understanding Weather and Climate, 3rd edition. Pearson Education, Inc., Upper Saddle River, New Jersey.

Ahrens, C. D., 1994. Meteorology today: an introduction to weather, climate, and the environment, 5th edition. West Publishing Company: St. Paul, Minnesota.

Baggi, S., and J. Schweizer, 2008. Characteristics of wet-snow avalanche activity: 20 years of observations from a high alpine valley. Natural Hazards, 50, 97-108.

Barnett, T. P., J. C. Adam, and D. P. Lettenmaier, 2005. Potential impacts of a warming climate on water availability in snow-dominated regions. Nature, 438, 303-309.

Barry, R.G., 2008. Mountain weather and climate, 3rd edition. Cambridge University Press: Cambridge, UK.

Barry, R. G., and R. J. Chorley, 1992. Atmosphere, weather and climate, 6th edition. Routledge: New York, New York.

Barton, M. Climatologist, Environment Canada. Vancouver, British Columbia.

BC Hydro, 2012. Generation system. Retrieved 22 Mar 2012 from BC Hydro website: http://www.bchydro.com/energy_in_bc/our_system/generation.html.

Bowling, J. Technical Services, Meteorological Service of Canada. Prince George, British Columbia.

Carozzi, A. V., and J. K. Newman, 1995. Horace-Bénédict de Saussure: Forerunner in glaciology. Mémories Soc. Phys., Histoires naturelles de Geneve. Geneva: Éd. Passé Présent, 48, pp. 149.

Carrega, P., 1995. A method for the reconstruction of mountain air temperatures with automatic cartographic applications. Theor. Appl. Climatol., 52, 69-84.

Chapman, J. D., 1952. The climate of British Columbia. Paper presented to the fifth British Columbia Natural Resources Conference. University of British Columbia, February 27, 1952.

Colbeck, S. C., 1994. Bottom temperatures of skating skis on snow. Medicine & Science in Sports and Exercise, 26, 258-262.

Colette, A., F. K. Chow, and R. L. Street, 2003. A numerical study of inversion-layer breakup and the effects of topographic shading in idealized valleys. Journal of Applied Meteorology, 42, 1255-1272.

Colle, B. A., B. F. Smull, M-J. Yang, 2002. Numerical simulations of a landfalling cold front observed during COAST: Rapid evolution and responsible mechanisms. Monthly Weather Review, 130, 1945–1966.

Cortemiglia, G. C., 1988. Variazoni termometriche con la quota nel bacino della Scrivia (Piemonte meridionale). Proc. CIMA '88: 20th Congresso Int. di Meteorologia Alpina, Sestola, Italy, 329-340.

Cortemiglia, G. C., R. Rossetti, A. Ghezzi, and M. Tortelli, 1989. Variations thermiques avec l'altitude dans les Alpes occidentales italiennes: Actes du colloque de Pavia, Italie, 1-3 Juin 1989. Publ. Assoc. Int. Climatol., 2, 19-26.

Crawley, M. J., 2005. Statistics: An introduction using R. John Wiley & Sons, Ltd.: England.

Daly, C., W. P. Gibson, G. H. Taylor, G. L. Johnson, and P. Pasteris, 2002. A knowledge-based approach to the statistical mapping of climate. Climate Research, 22, 99-113.

Defant, F., 1949. Zur Theorie der Handwind, nebst Bemerkungen zue Theorie der Berg- und Talwinde. [A theory of slope winds along with remarks on the theory of mountain winds and valley winds]. Arch. Meteor. Geophys. Bioklim., A1, 421-450, English translation: C. D. Whiteman and E. Dreiseitl, 1984. Alpine Meteorology: Translations of classic contributions by A. Wagner, E. Ekhart and F. Defant. Pacific Northwest Laboratory, Richland, Washington, 121 pp. [PNL-5141/ASCOT-84-3].

De Saussure, H. B., 1779-96. Voyages dans les Alpes, précédes d'un eassai sur l'histoire naturelle des environs de Geneve. Vol. 2, Chapters XXXV and LIII 1786, and Vol. 4, Chapters V-IX 1796, Neuchatel: L. Fauche-Borel.

Douguédroit, A., and M. F., De Saintignon, 1970. Méthode d'étude de la décriossance des températures en montagne de latitude moyenne: exemple des Alpes françaises du sud. Rev. Geogr. Alp., 58, 453-472.

Doyle, C. Chief, Weather Services, 2010 Winter Olympic and Paralympic Games, Environment Canada. Vancouver, British Columbia.

Dreiseitl, E., 1988. Slope and free air temperature in the Inn Valley. Meteorology and Atmospheric Physics, 39, 25-41.

Ekhart, E., 1939. Mittlere temperaturverhältnisse der alpen und der freien atmosphäre über dem alpenvorland. Ein beitrag zur dreidimensionalen klimatologie. 1. Die temperaturverhältnisse der alpen. Met. Zeit., 56, 12-26.

Ekhart, E., 1944. Beiträge zur alpinen Meteorologie [Contributions to alpine meteorology]. Meteorologische Zeitschrift, 61 (7), 217-231, English translation: C. D. Whiteman and E. Dreiseitl, 1984. Alpine Meteorology: Translations of classic contributions by A. Wagner, E. Ekhart and F. Defant. Pacific Northwest Laboratory, Richland, Washington, 121 pp. [PNL-5141/ASCOT-84-3].

Ekhart, E., 1948. De la structure Thermique de l'Atmosphere dans la Montagne [On the thermal structure of the mountain atmosphere]. La Meteorologie, 4(9), 3-26, English translation: C. D. Whiteman and E. Dreiseitl, 1984. Alpine Meteorology: Translations of classic contributions by A. Wagner, E. Ekhart and F. Defant. Pacific Northwest Laboratory, Richland, Washington, 121 pp. [PNL-5141/ASCOT-84-3].

Environment Canada. PSPC Weather Data Archive. Retrieved Sept 2011 from http://jervis.pyr.ec.gc.ca/.

Ficker, H. von, 1913. Temperatur differenz zwischen freier atmosphäre und berggipfeln. Meteor. Z., 30, 278-289.

Freedman, J. M., D. R. Fitzjarrald, K. E. Moore, and R. K. Sakai, 2001. Boundary layer clouds and vegetation-atmosphere feedbacks. Journal of Climate, 14, 180-197.

Furman, R. W., 1978. Wildfire zones on a mountain ridge. Ann. Ass. Am. Geog., 68, 89-94.

Google Earth, 2012. Whistler Mountain map images. Retrieved Oct 2011 using Google Earth software.

Grenfell, T. C., S. G. Warren, and P. C. Mullen, 1994. Reflection of solar radiation by the Antarctic snow surface at ultraviolet, visible, and near-infrared wavelengths. Journal of Geophysical Research, 99, 18669-18684.

Haiden, T., and C. D. Whiteman, 2005. Katabatic flow mechanisms on a low-angle slope. Journal of Applied Meteorology, 44, 113-126.

Hann, J. von, 1913. Die berge kalter als die atmosphere, ein meteorologisches Paradoxon. Meteor. Z., 30, 304-306.

Hansel, C. von, 1962. Die unterschiede von temperature und relativer Feuchtigkeit zwischen Brocken und umgebender frier atmosphäre. Zeit. Met., 16, 248-252.

Harlow, R. C., E. J. Burke, R. L. Scott, W. J. Shuttleworth, C. M. Brown, and J. R. Petti, 2004. Derivation of temperature lapse rates in semi-arid southeastern Arizona. Hydrol. Earth Syst. Sci., 8, 1179-1185.

Hildebrandt, A., 1912. Vergleich der temperature auf dem Brocken und in der gleichen Höhe der freien atmosphäre auf Grund neuerer ballon und drachenaufstiege. Geographische Arbeiten, Heft VII, 26, S., Stuttgart, Fed. Rep. of Germany.

Howard, R., and R. Stull, 2011. Forecasting sun vs. shade in complex terrain for the 2010 Winter Olympic and Paralympic Games. Bulletin of the American Meteorology Society, 92, 1303-1309.

Joe, P. Acting Research Manager and Research Scientist, Environment Canada. Toronto, Ontario.

Joe, P., 2009. A short note on the Whistler mid-mountain or Harvey's cloud. Internally Published Document.

Joe, P., C. Doyle, A. Wallace, S.G. Cober, B. Scott, G. A. Isaac, T. Smith, J. Mailhot, B. Snyder, S. Belaire, Q. Jansen, and B. Denis, 2010. Weather services, science advances, and the Vancouver 2010 Olympic and Paralympic Winter Games. Bulletin of the American Meteorological Society, 91: 31-36.

Klock, R., and J. Mullock, 2001. The weather of British Columbia: Graphic area forecast 31. NAV CANADA: Ottawa, Ontario.

Kutner, M. H., C. J. Nachtsheim, and J. Neter, 2004. Applied linear statistical models, 5th edition, McGraw Hill, 1396 pp.

Liou, K. N., 2002. An introduction to atmospheric radiation. Academic Press: San Diego.

Lundquist, J. D., and D. R. Cayan, 2007. Surface temperature patterns in complex terrain: daily variations and long-term change in the central Sierra Nevada, California. Journal of Geophysical Research: 112, D11124.

Mahrt, L., 2006. Variation of surface air temperature in complex terrain. Journal of Applied Meteorology and Climatology, 45, 1481-1493.

Mailhot, J., S. Belair, M. Charron, C. Doyle, P. Joe, M. Abrahamowicz, N. B. Bernier, B. Denis, A. Erfani, R. Frenette, A. Giguere, G. A. Isaac, N. McLennan, R. McTaggart-Cowan, J. Milbrandt, and L. Tong, 2010. Environment Canada's experimental numerical weather prediction systems for the Vancouver 2010 Winter Olympic and Paralympic Games. Bulletin of the American Meteorological Society, 91: 1073-1085.

Martinec, J., and A. Rango, 1986. Parameter values for snowmelt runoff modeling. Journal of Hydrology, 84, 197-219.

Martinec, J. A., and A. Rango, 1998. Snowmelt runoff model (SRM) user's manual. USDA-ARS Hydrology and Remote Sensing Laboratory, 84 pp.

Mass, C., 2008. The Weather of the Pacific Northwest. University of Washington Press: Seattle, Washington.

Mayr, R., 2000. Temperature profiles along mountain slopes and their relationship to vertical profiles in the mid-valley atmosphere. Research Report.

McClung, D., and P. Schaerer, 2006. The avalanche handbook, 3rd edition. The Mountaineers Books: Seattle, Washington.

McCollor, D., and R. Stull, 2008. Hydrometeorological Short-Range Ensemble Forecasts in Complex Terrain. Part II: Economic Evaluation. Weather and Forecasting, 23, 557-574.

McCutchan, M. H., 1983. Comparing temperature and humidity on a mountain slope and in the free air nearby. Monthly Weather Review, 111, 836-845.

McCutchan, M. H., and D. G. Fox, 1986. Effect of elevation and aspect on wind, temperature and humidity. J. Clim. Appl. Met., 25, 1996-2013.

Meteorological Service of Canada, 2001. Weather and Environmental Monitoring Directorate. MSC STDS 2 – 2001 Version 2.4. Internally Published Document.

Meteorologist Operational Internship Program (MOIP), 2006. Program Training Notes, Module 3.2D. Prepared by W. Benjamin. Internally Published Document.

Mo, R., P. Joe, G. A. Isaac, I. Gultepe, R. Rasmussen, J. Milbrandt, R. McTaggart-Cowan, J. Mailhot, M. Brugman, T. Smith, and B. Scott, 2011. Mid-mountain clouds at Whistler during the Vancouver 2010 Winter Olympics and Paralympics. Accepted to Pure and Applied Geophysics.

Müller, M. D., and D. Scherer, 2005. A grid- and subgrid-scale radiation parameterization of topographic effects for mesoscale weather forecast models. Monthly Weather Review, 133, 1431-1442.

Neter, J., M. H. Kutner, C. J. Nachtsheim, and W. Wasserman, 1996. Applied linear statistical models, 4th edition. McGraw Hill: Boston, 338 pp.

Oke, T. R., 1978. Boundary Layer Climates, 2nd Edition. Routledge: New York.

Paul, P., 1976. La décroissance de la température avec l'altitude dans les Vosges et la Forêt-Noire: Aspects locaux et régionaux. Rech. Geogr. Strasbourg, 4, 55-67.

Pawley, D. Technical Services Officer, Atmospheric Monitoring, Environment Canada. Richmond, British Columbia.

Pepin, N. C., and J. D. Lundquist, 2008. Temperature trends at high elevations: Patterns across the globe. Geophysical Research Letters, 35, L14701.

Pepin, N. C., and J. R. Norris, 2005. An examination of the differences between surface and free-air temperature trend at high-elevation sties: Relationships with cloud cover, snow cover, and wind. Journal of Geophysical Research, 110, D24112.

Peppler, W., 1931. Zur frage des temperaturunterschiedes zwischen den berggipfeln und der freien atmospäre. Beitr. Phys. Atmos., 17, 247-263.

Pielke, R. A., and P. Mehring, 1977. Use of mesoscale climatology in mountainous terrain to improve the spatial representation of mean monthly temperatures. Monthly Weather Review, 105, 180-112.

Price, J. D., and M. R. Bush, 2004. Comparisons between model forecast and observed boundary layer profiles and related comments on cloud prediction. Wea. Forecasting, 19, 959–969.

Quick, M. C., and A. Pipes, 1977. U.B.C. Watershed Model. Hydrological Sciences – Bulletin, 21, 153-161.

Reeves, H. D., K. L. Elmore, G. S. Manikin, and D. J. Stensrud, 2011. Assessment of forecasts during persistent valley cold pools in the Bonneville Basin by the North American Mesoscale Model. Wea. Forecasting, 26, 447–467.

Régnière, J., 1996. Generalized approach to landscape-wide seasonal forecasting with temperature-driven simulation models. Environmental Entomology, 25, 869-881.

Richardson, A. D., X. Lee, A. J. Friedland, 2004. Microclimatology of treeline spruce-fir forests in mountains of the northeastern United States. Agric. Forest Meteorol., 125, 53-66.

Richner, H., and P. D. Philips, 1984. A comparison of temperatures from mountaintops and the free atmosphere – Their diurnal variation and mean difference. Monthly Weather Review, 112, 1328-1340.

Roeger, C., R. B. Stull, D. McClung, J. Hacker, X. Deng, and H. Modzelewski, 2003. Verification of mesoscale numerical weather forecasts in mountainous terrain for application to avalanche prediction. Weather and Forecasting, 18: 1140-1160.

Rolland, C., 2003. Spatial and seasonal variations of air temperature lapse rates in alpine regions. Journal of Climate, 16, 1032-1046.

Running, S. W., R. R. Nemani, and R. D. Hungerford, 1987. Extrapolation of synoptic meteorological data in mountainous terrain and its use for simulating forest evapotranspiration and photosynthesis. Can. J. For. Res., 17, 472-483.

Sampson, C. A., 1965. A comparison of mountain slope and radiosonde observations. Monthly Weather Review, 93, 327-330.

Schell, I. I., 1934. Differences between temperature, humidities, and winds on the white mountains and in the free air. Trans. Amer. Geophys. Union, 118-124.

Schmauss, A., 1907. Gleichzeitige temperaturen auf der Zugspitze und in der atmosphäre über München in gleicher Seehöhe. Meteor. Z., 24, 468-470.

Seidel, D. J., and M. Free, 2005. Diurnal cycle of upper-air temperature estimated from radiosondes. Journal of Geophysical Research, 110, D09102, doi: 10.1029/2004JD005526.

Shafer, J. C., W. J. Steenburgh, J. A. W. Cox, and J. P. Monteverdi, 2006. Terrain influences on synoptic storm structure and mesoscale precipitation distribution during IPEX IOP3. Monthly Weather Review, 134, 478-497.

Smith, R., Paegle, J., Clark, T., Cotton, W., Durran, D., Forbes, G., Marwitz, J., Mass, C., Mcginley, J., Pan, H.L., Ralph, M., 1997. Local and remote effects of mountains on weather: Research needs and opportunities. Bull. Amer. Meteor. Soc., 78, 877–892.

Steenburgh, W. J., 2003. One hundred inches in one hundred hours: Evolution of a Wasatch Mountain winter storm cycle. Weather Forecasting, 18, 1018–1036.

Steiner, M., O. Bousquet, Jr. R. A. Houze, B. F. Smull, and M. Mancini, 2003. Airflow within major Alpine river valleys under heavy rainfall. Quarterly Journal of the Royal Meteorological Society, 129, 411-431.

Stull, R. B., 1988. An introduction to boundary layer meteorology. Springer: New York.

Stull, R.B., 1991. Boundary-layer clouds – A case study of cover hours. Journal of Climate, 5, 390-394.

Stull, R., 1992. Impact of boundary-layer clouds – A case study of cover hours. Journal of Climate (Notes and Correspondence), 5, 390-394.

Thompson, W. T., 1981. Determination of vertical temperature profiles in complex terrain. Preprint Second Conf. Mountain Meteor., Steamboat Springs, Amer. Meteor. Soc., 266-269.

Thornton, P. E., S. W. Running, and M. A. White,1997. Generating surfaces of daily meteorological variables over large regions of complex terrain. J. Hydrol., 190, 214-251.

Wagner, A., 1930. Uber die feinstruk des temperaturgradienten längs berghängen. Zeit. Geophys., 6, 310-318.

Wagner, A., 1938. Theorie und Beobachtung der periodischen Gebirgswinde [Theory and observation of periodic mountain winds]. Gerlands Beitr. Geophys., 52, 408-449, English translation: C. D. Whiteman and E. Dreiseitl, 1984. Alpine Meteorology: Translations of classic contributions by A. Wagner, E. Ekhart and F. Defant. Pacific Northwest Laboratory, Richland, Washington, 121 pp. [PNL-5141/ASCOT-84-3].

Wekker, S. F. J. De, and C. D. Whiteman, 2005. On the time scale of nocturnal boundary layer cooling in valleys and basins and over plains. Journal of Applied Meteorology and Climatology, 45, 813-820.

Whistler Blackcomb, 2010. Trail map. Retrieved 4 Feb 2010 from Whistler Blackcomb website: http://www.whistlerblackcomb.com/mountain/maps/index.htm.

Whiteman, C. D., 2000. Mountain meteorology: Fundamentals and applications. Oxford University Press: New York.

Whiteman, C. D., and E. Dreiseitl, 1984. Alpine Meteorology: Translations of classic contributions by A. Wagner, E. Ekhart and F. Defant. Pacific Northwest Laboratory, Richland, Washington, 121 pp. [PNL-5141/ASCOT-84-3].

Whiteman, C. D., K. J. Allwine, L. J. Fritschen, M. M. Orgill, and J. R. Simpson, 1989. Deep valley radiation and surface energy budget microclimates. Part II: Energy budget. Journal of Applied Meteorology, 28, 427-437.

Whiteman, C. D., J. M. Hubbe, and W. J. Shaw, 2000. Evaluation of an inexpensive temperature datalogger for meteorological applications. Journal of Atmospheric and Oceanic Technology, 17, 77-81.

Whiteman, C. D., S. Zhong, W. J. Shaw, J. M. Hubbe, and X. Bian, 2001. Cold pools in the Columbia Basin. Weather and Forecasting, 16, 432-447.

Whiteman., C.D., S.E. Eisenbach, B. Pospichal, and R. Steinacker, 2004. Comparison of vertical soundings and sidewall air temperature measurements in a small alpine basin. Journal of Applied Meteorology, 43, 1635-1647.

Wilber, A. C., D. P. Kratz, and S. K. Gupta, 1999. Surface emissivity maps for use in satellite retrievals of longwave radiation. National Aeronautics and Space Administration, TP-1999-209362.

Wiscombe, W. J., and S. G. Warren, 1980. A model for the spectral albedo of snow: pure snow. Journal of the Atmospheric Sciences, 37, 2712-2733.

Wong, P. Atmospheric Monitoring Division, Environment Canada. Richmond, British Columbia.

World Meteorological Organization, 1996. Guide to Meteorological Instruments and Methods of Observation. WMO-No. 8.

Yarnal, B., 1993. Synoptic climatology in environmental analysis. Belhaven Press: London.

Zhong, S., C. D. Whiteman, X. Bian, W. J. Shaw, and J. M. Hubbe, 2001. Meteorological processes affecting the evolution of a wintertime cold air pool in the Columbia basin. Monthly Weather Review, 129, 2600-2613.

Zhong, S., and J. Fast, 2003. An evaluation of the MM5, RAMS, and Meso-Eta Models at subkilometer resolution using VTMX field campaign data in the Salt Lake Valley. Mon. Wea. Rev., 131, 1301–1322.

Appendix A: Instrument Specifications

Instrument	ID	Range and Accuracy	Logging interval
Hoskins Scientific U23-002 temperature and relative humidity data logger	UBC1, UBC2, UBC3, UBC4, UBC5	Temperature measurement range: -40°C to +70°C Accuracy: -20°C to 0°C: ±0.36°C 0°C to +25°C: ±0.18°C +25°C to +40°C: ±0.2°C	5 minutes (changed to 15 minutes in January 2010)
Campbell Scientific HMP45C temperature and relative humidity sensor	VOB, VOT, VOL, VOA, VOH	Temperature measurement range: -40°C to +60°C Accuracy: -40°C to -20°C: ±0.4°C -20°C to 0°C: ±0.3°C 0°C to +20°C: ±0.2°C +20°C to +40°C: ±0.2°C	15 minutes
Campbell Scientific HMP45CF temperature and relative humidity sensor	WHI	Temperature measurement range: -55°C to +50°C Accuracy: -50°C to -40°C: ±1.0°C -40°C to -30°C: ±0.8°C -30°C to +50°C: ±0.6°C -10°C to +10°C: ±0.3°C	1 minute
Vaisala RS92-SGP radiosonde	VOC	Temperature measurement range: -90 °C to +60 °C Reproducibility in sounding: 1080 to 100 hPa: 0.2 °C, 100 to 20 hPa: 0.3 °C, 20 to 3 hPa: 0.5 °C, Resolution: 0.1 °C	Three times daily (0315, 0915, 1515 PST) for February 2009. Four times daily (0315, 0915 1515, 2115 PST) in February 2010. Two times daily (0315, 1515 PST) for March 2010.

Table A.1: Specifications for all instrumentation used in this study.

Appendix B: Weather Stations

The following provides a description of each weather station site including the slope aspect, elevation, and the general surroundings. Each section also contains a series of photographs and maps to provide a visualization of each station's configuration and its location relative to other stations or topographical features. Stations are described in ascending order.

B.1 Automated Station UBC5

Aspect: Base of a west-facing slope

Elevation: 654 mASL

Since the lowest EC weather station recorded temperatures approximately 130 m above the valley floor, UBC5 (Fig. B.1a) was specifically installed at the base of Whistler Mountain to complete the mountainside profile. Positioned on the first gondola tower, gentle beginner ski trails led skiers down toward the Creekside Village on either side (Fig. B.1b). A broad, flat patio area with nearby hotels and restaurants was located due-west of the sensor. Its location was far enough away from crowds and buildings to avoid unwanted heat sources but close enough to the valley floor to record temperature inversions.

Figure B.1: a) UBC5 temperature and relative humidity sensor, and b) view east (uphill) of tower 1 on the Creekside gondola.

B.2 Automated Station VOT

Aspect: West-facing slope

Elevation: 782 mASL

Venue construction delayed the installation of VOT until February 2009 where it was first installed down-slope from the alpine course finish line. It was then relocated on top of the Olympic judge's platform on the north side of the finish line in December 2009 (Fig. B.2). Here, its 270° exposure on the northwest corner of the building minimized unwanted effects from the buildings below and ensured that the station was well away from crowds and vehicles. Located on a fairly broad, non-forested ski trail with gentle relief, this site provided temperature measurements that were representative of finish line conditions.
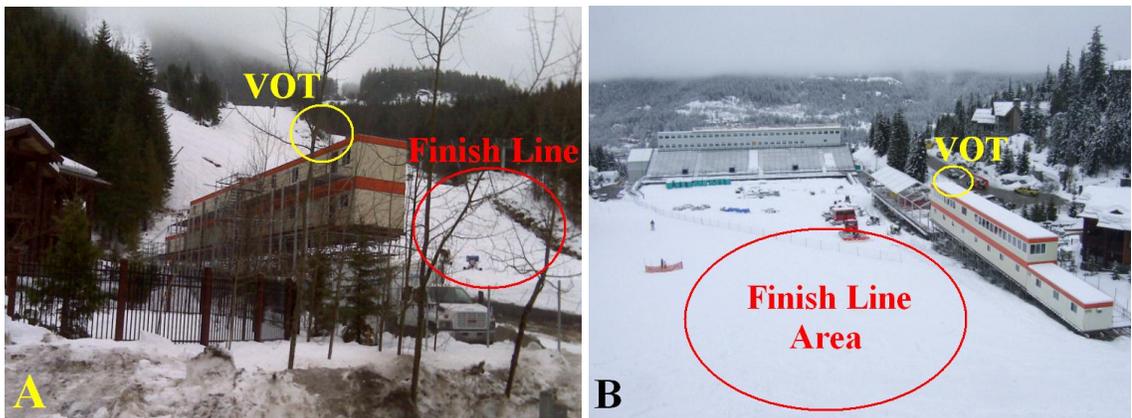

Figure B.2: Location of VOT (had not been installed when these pictures were taken) relative to the finish line with photograph a) taken from behind judge's platform, looking uphill (Photograph courtesy of Drew Pawley, EC), and b) taken on the alpine course, looking downhill at the finish line.

B.3 Automated Station VOB

Aspect: West-facing slope
Elevation: 918 mASL

VOB was located in a small clearing within the forest on a gentle slope between the Lower Dave Murray trail (alpine course) and the Lower Franz's trail (Fig. B.3). It was representative of the lower portion of the Men's and Women's alpine events and its installation in January 2006 (prior to VOT), provided a long temperature record for this portion of the course. Insufficient aspiration of this sensor was possible given the extent of the surrounding forest illustrated in Fig. B.3b, thus it was beneficial to have VOT nearby to better measure temperature on the alpine course and provide comparisons for VOB data.
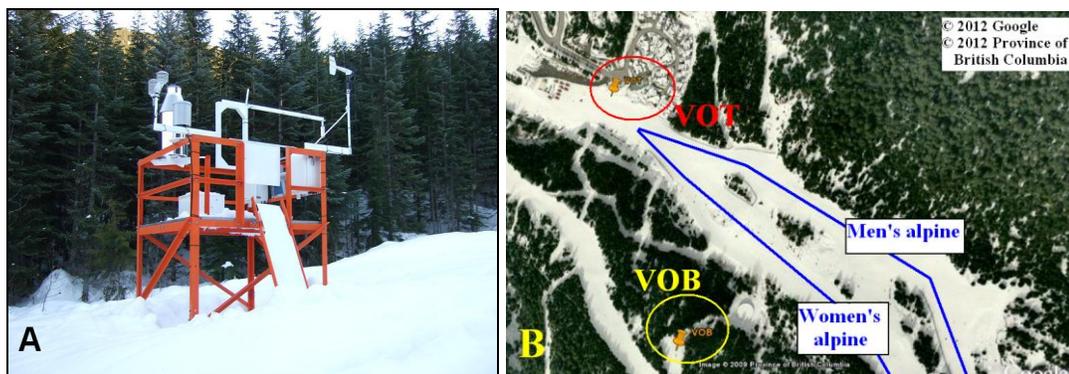
Figure B.3: a) Weather station VOB, and b) location of VOB in relation to alpine courses and VOT (Image courtesy of Google Earth).

B.4 Automated Station UBC4

Aspect: West-facing slope

Elevation: 1040 mASL

UBC4 was mounted on tower 17 of the Creekside Gondola alongside the Dave Murray ski trail (Fig. B.4). Thick forest bordered this sensor to its north with thinner vegetation to its south. A wide swath was clear cut through the trees to make way for the gondola line, exposing this sensor to upslope and downslope flow (Fig. B.4b). A steep cliff was situated upslope (east) of the sensor, and a moderately steep slope dropped down through the trees to its west. The surrounding terrain and vegetation did not appear to have skewed the temperature data.
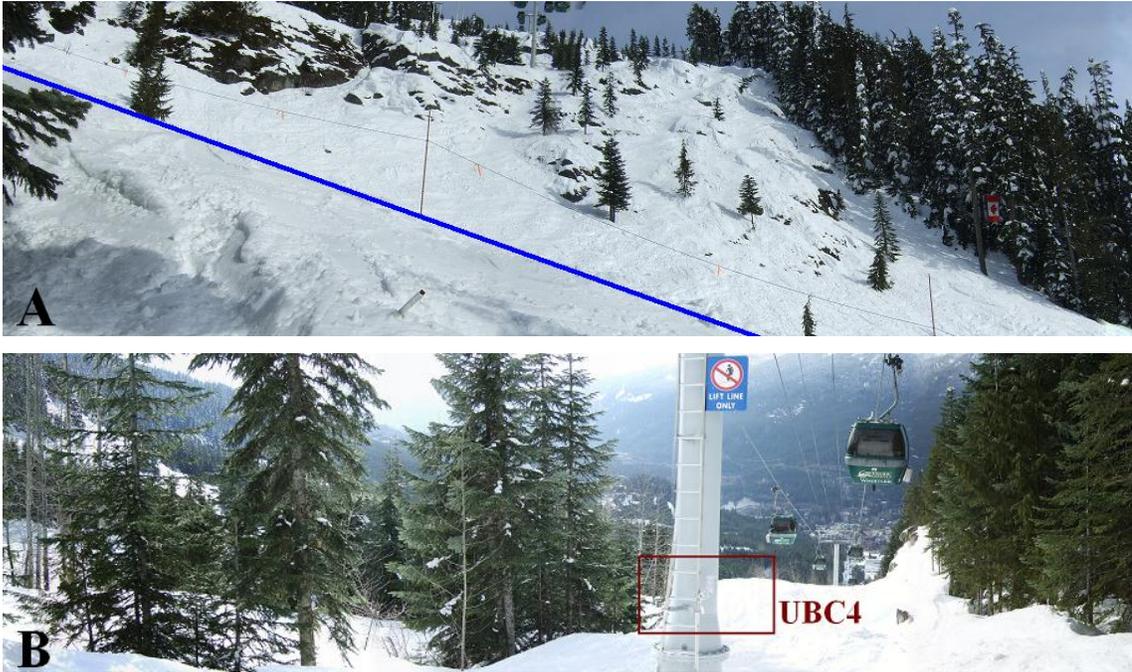
Figure B.4: a) View east (uphill) with the angle of the adjacent Dave Murray ski slope (blue line) shown, and b) view west (downhill) showing UBC4 and its position relative to the surrounding vegetation.

B.5 Automated Station VOL

Aspect: West-facing slope

Elevation: 1300 mASL

VOL, also known as "Mid-Station", was located on a knoll approximately 20 m above the Creekside Gondola lift exchange (Fig. B.5). The Men's and Women's Olympic Downhill courses came down on either side of this site. Although VOL was located in a relatively flat area, the slope quickly dropped away to the west (downhill towards the Creekside Village), with a steep cliff to the east (uphill) and moderately-sloped ski trails that funneled down into this area from the north and south. This site was the least sheltered out of all the mountainside stations.
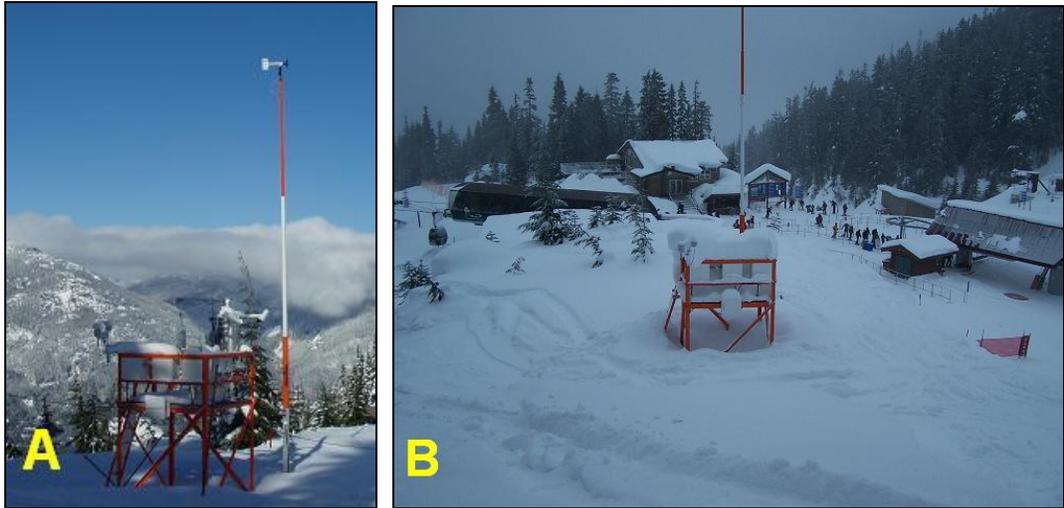
Figure B.5: a) VOL with wind tower, and b) VOL relative to lift exchange (Photographs courtesy of Mark Barton, EC).

B.6 Automated Station UBC3

Aspect: West-facing slope

Elevation: 1462 mASL

Located on tower 9 of the Big Red Express Chair and adjacent to a broad, beginner's ski run (Pony Trail), UBC3 had good exposure to upslope flow from the southwest (Fig. B.6). A path through thin vegetation had been clear cut for the Gondolas exposing the sensor to air flow from the west through northwest directions. The immediate topography was composed of gentle relief from the ski trail and gondola line. Steep cliffs then bordered this area on both the uphill (east) and downhill (west) sides.

Figure B.6: a) View southwest showing UBC3 in relation to the chair lift line (due west) and the Pony Trail, and b) view north illustrating UBC3's exposure to upslope and downslope flow.

B.7 Automated Station UBC2

Aspect: Bench above a west-southwest-facing slope

Elevation: 1599 mASL

UBC2 was mounted on tower 17 (Big Red Express Chair) in a predominantly flat area with sparse vegetation outlining the surrounding ski trails (Fig. B.7). A nearby slope dropped away to the west-southwest and a small mountain ridge blocked it from air flow to the northeast. The concern with this location was that the tower was located in small (in radius) but deep depression. Fortunately, drifting snow filled in the hole, preventing unwanted effects (e.g., cold air pooling) and allowed the sensor to be easily maintained at a height of 1.5 m above the surrounding level ground surface.
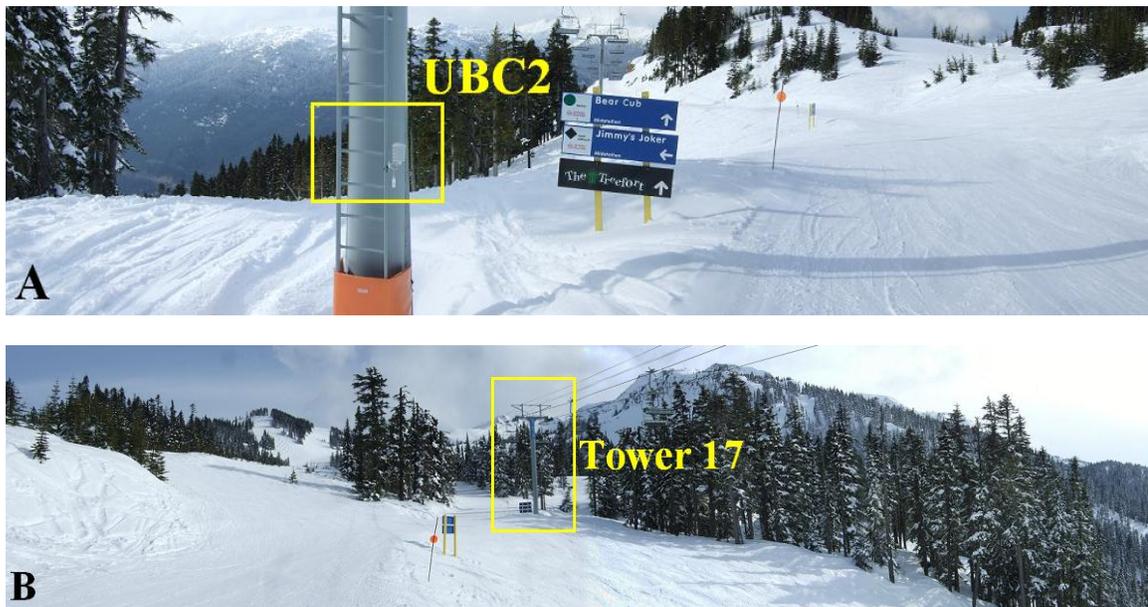
Figure B.7: a) View west showing UBC2's attachment to the ski lift tower, and b) view up-mountain indicating the position of tower 17 of the Big Red Express Chair in relation to the surrounding mellow ski trails.

B.8 Automated Station VOA

Aspect: Northeast-facing slope

Elevation: 1624 mASL

As shown below (Fig. B.8a) VOA was co-located with one of the Whistler Mountain weather stations (Pig Alley – WHIST1). This area was predominantly flat with sparse vegetation to the southwest and thicker forest to the northeast. Surrounding ski trails were gentle beginner slopes with a short, steeper section uphill to the southwest. Located on the other side of the ridge from the alpine course on a northeast-facing slope (Fig. B.8b), the diurnal temperature cycle of VOA differed significantly from nearby stations. Temperature data from VOA was thus omitted from this study.
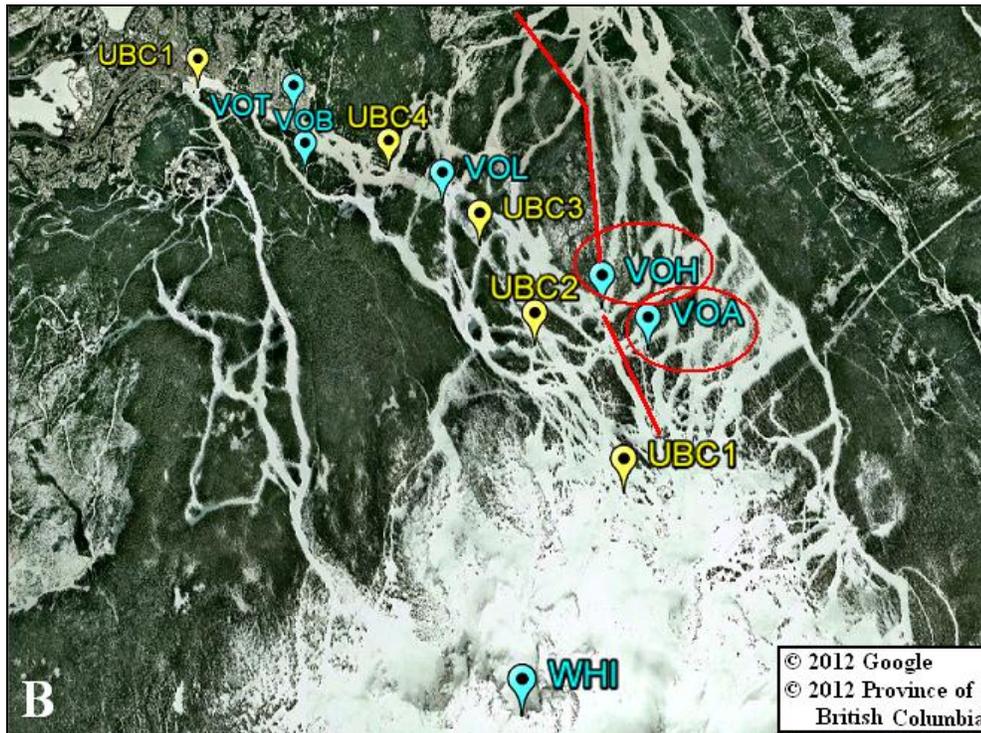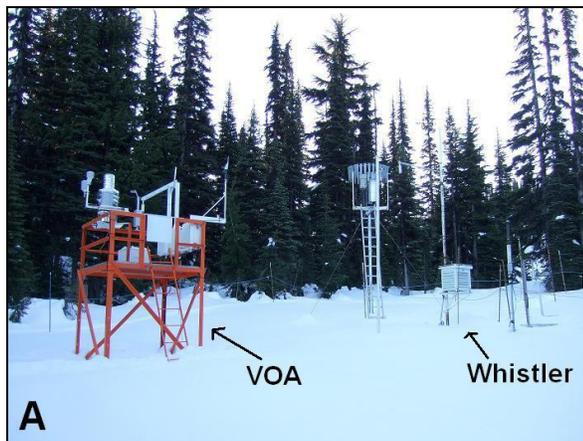
**Figure B.8: a) Weather station VOA co-located with Whistler Mountain weather station, and b) locations of VOA and VOH (red circles) relative to the ridge line (red line) which separates it from the slope where the rest of the stations are located (Image courtesy of Google Earth).**

B.9 Automated Station VOH

Aspect: On a ridge-top separating the northeast- and west-facing slopes

Elevation: 1662 mASL

Located in an open area near the top of the Garbonzo Express Chair, VOH (Fig. B.9) had good exposure in most directions (aside from vegetation to the north-northwest). Approximately 40 m higher than VOA on top of the ridge separating the west slopes of the alpine courses from the rest of the mountain, this station provided more representative temperature measurements for the upper alpine courses.
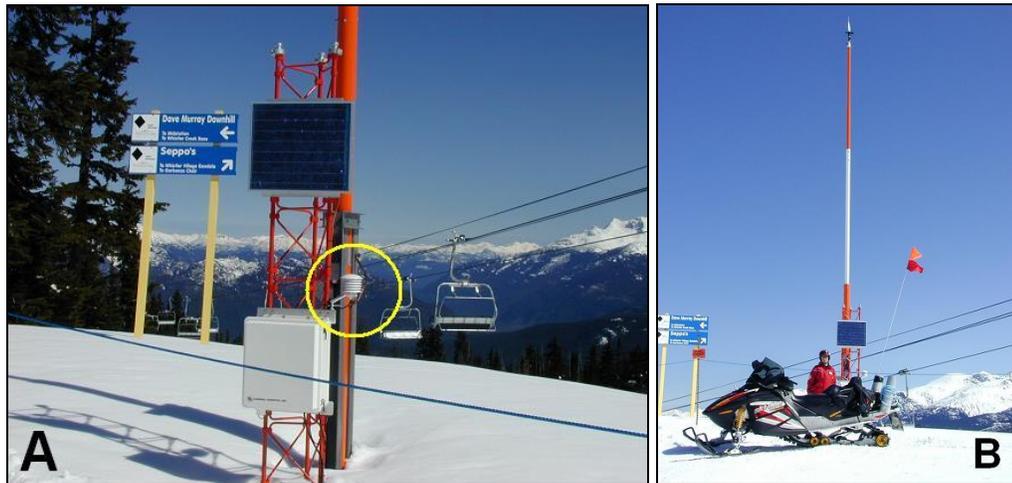
Figure B.9: a) Base of VOH station showing relative humidity and temperature sensor (circled), and b) entire VOH station showing 10-m wind tower (Photographs courtesy of Mark Barton, EC).

B.10 Automated Station UBC1

Aspect: West-facing slope

Elevation: 1763 mASL

UBC1, mounted on tower 28 (Big Red Express Chair), provided temperature measurements representative of the upper west-facing slope. Located just below Roundhouse Lodge, the surrounding slopes were broad, and extremely gentle in all directions (Fig. B.10). Its close proximity to tree line meant that nearby vegetation was sparse. Aside from some blocking from the small ridge to its north-northeast, this sensor had ideal exposure in all other directions.

Figure B.10: a) View west (downhill) showing UBC1's attachment to tower 28, and b) view east (uphill) of the sparse vegetation and surrounding ski trails.

B.11 Automated Station WHI

Aspect: On the peak of Whistler Mountain directly above the west-facing slope
Elevation: 2180 mASL

The WHI station was situated on the west side of the broad, flat peak of Whistler Mountain (Fig. B.11a). Instrumentation is attached to a post on the southwest corner of a building, directly above an extremely steep drop into Whistler Bowl. Blocked by the building to its east through south, the temperature sensor had good exposure in all other directions. This site, however, undergoes frequent riming (Fig. B.11b) which inhibits natural aspiration of the sensor within the radiation shield.

Figure B.11: a) Photograph taken from UBC1 looking southeast towards Whistler Peak, and b) southwest corner of the WHI building illustrating the position of the temperature and relative humidity sensor (yellow box).

B.12 Automated Station VOC/Manned station WAE

Elevation: 651 mASL

Special mention of weather station VOC is given, as it was the site from which radiosondes were launched. VOC was co-located with the manned Whistler weather station (WAE) in the middle of the valley, approximately 1.5 km north of Whistler Village (Fig. B.12). The Sea-to-Sky highway is situated within metres of this enclosed area's eastern fence, with large trees surrounding it from all other directions. Due to its location in the valley, this site was prone to exceptionally cooler nighttime temperatures. Cold air drainage combined with radiative cooling produced valley temperature inversions, a phenomenon seen frequently in the radiosonde profiles.
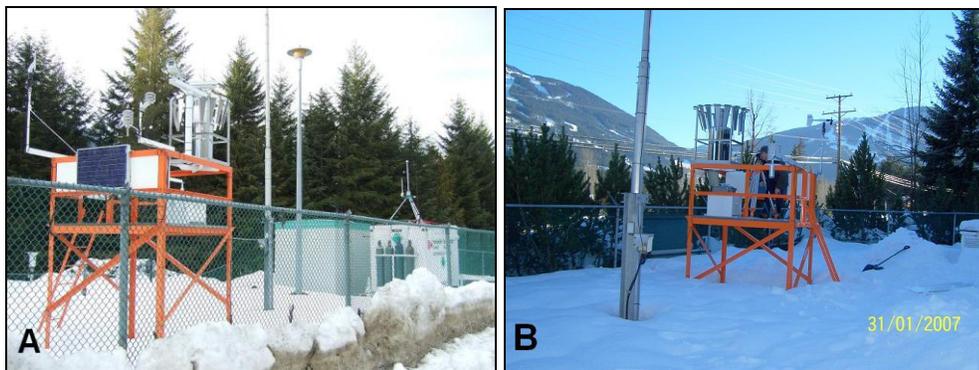

Figure B.12: a) Weather station VOC co-located with the radiosonde launch station, and b) view looking south towards Blackcomb (left) and Whistler (right) (Photographs courtesy of Mark Barton, EC).

Appendix C: Siting Standards for Temperature Measurements

Taken from MSC (2001) the following siting standards are consistent with World Meteorological Organization recommendations, individual instrument manuals, and manufacturer's recommendations.

The site should be located:

    (i)   such that sensors shall be at a distance from vertical obstructions (e.g., trees, buildings, etc.) of at least two times the height of the obstruction for Stevenson screens.

    (ii)   in an area which provides ease of access for the observer.

Locations for sites which shall be avoided are:

(i)   the top of hills

(ii)   in hollows, at the bottom of narrow valleys and near hills, ridges, or cliffs

(iii)   near isolated ponds or streams

(iv)   near roads where snow from snow clearance operations, or dust, can affect the site

(v)   where there is excessive human or animal traffic

(vi)   where excessive drifting snow accumulates

(vii)   near vehicle parking areas

(viii) where heat is exhausted by buildings or vehicles

Appendix D: Scatter Plots of T_{SA} versus T_{FA} Temperature

Scatter plots of SA temperature versus FA temperature (open circles) for all cloud cover categories. Two lines are plotted: a reference line with a slope of 1 (black, dotted), and the linear regression model (red, solid). MBE, MAE, RMSE, adjusted-r^2 were calculated using the equations provided in Appendix E. The average height of Whistler Valley inversions was used to delineate temperature data within the inversion data from that above the inversion.
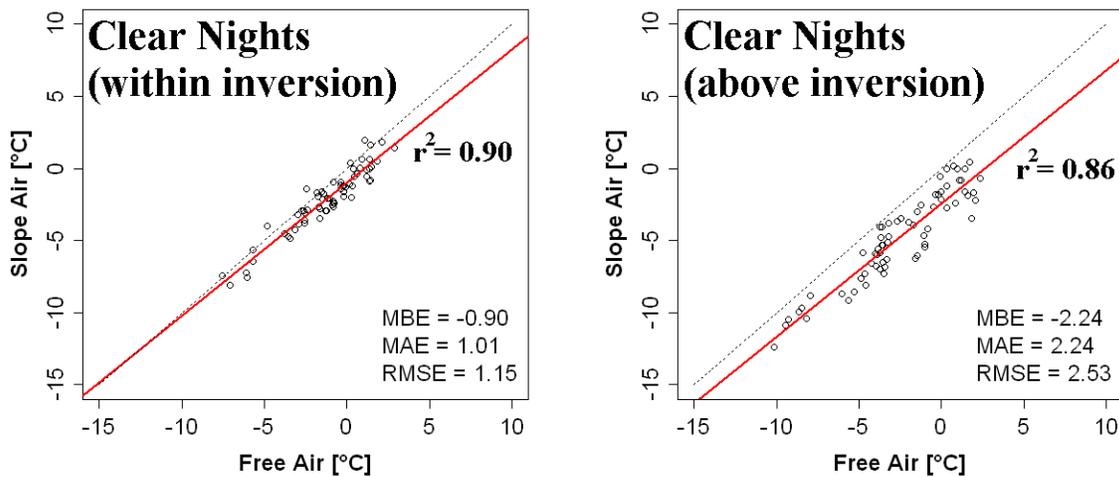

Figure D.1: Scatter plots of SA versus FA temperature for clear nights within and above the inversion.
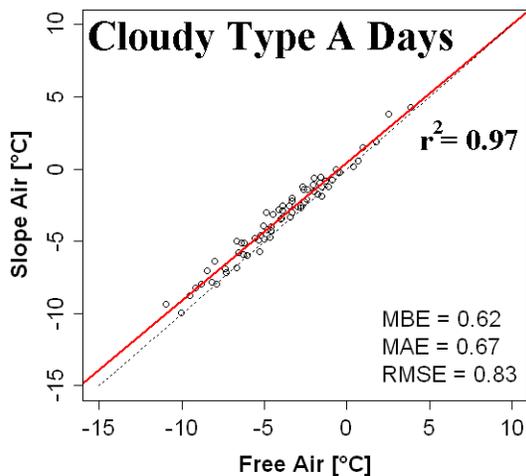

Figure D.2: Scatter plot of SA versus FA temperature for cloudy type A days.
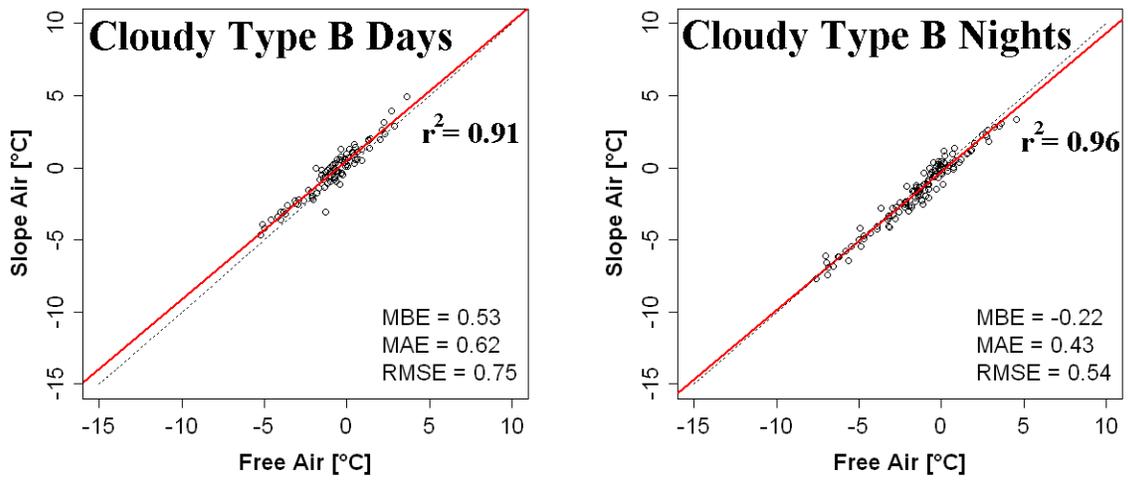
Figure D.3: Scatter plots of SA versus FA temperature for cloudy type B days and nights.

Appendix E: Equations

Equations below modified from Kutner et al., (2004) and Neter et al., (1996).

Mean bias error

$$MBE = \frac{1}{n} \sum_{i=1}^{n} (T_{SA})_i - (T_{FA})_i$$

Mean absolute error

$$MAE = \frac{1}{n} \sum_{i=1}^{n} |(T_{SA})_i - (T_{FA})_i|$$

Root mean square error

$$RMSE = \sqrt{\frac{1}{n} \sum_{i=1}^{n} \left[(T_{SA})_i - (T_{FA})_i \right]^2}$$

r^2, coefficient of determination

$$r^2 = 1 - \frac{SSE}{SSTO}$$

Adjusted-r^2

$$r_a^2 = 1 - \left[\frac{n-1}{n-p} \right] * \frac{SSE}{SSTO}$$

Where:

       p = number of parameters

       n = number of observations

       SSE = error sum of squares

       $SSTO$ = total sum of squares

       MSE = mean square error

Appendix F: Multiple Linear Regression Results

"***" highlights significant terms

Generally, p values <0.001 are significant (Crawley, 2005).

	Coefficients	Standard Error	t value	Pr(>|t|)
Intercept	0.72	0.50	1.44	0.15
T_{FA}	1.04	0.03	41.08	<2e-16 ***
Elevation	-0.0002	0.0004	-0.58	0.57

Table F.1: Multiple linear regression results for clear days.

	Coefficients	Standard Error	t value	Pr(>|t|)
Intercept	-1.34	0.34	-3.91	0.000189 ***
T_{FA}	0.95	0.30	31.47	< 2e-16 ***
Elevation	0.0003	0.0003	0.98	0.33

Table F.2: Multiple linear regression results for clear nights (within inversion).

	Coefficients	Standard Error	t value	Pr(>|t|)
Intercept	-3.48	3.70	-0.94	0.35
T_{FA}	0.89	0.05	18.56	<2e-16 ***
Elevation	0.0003	0.0022	0.15	0.88

Table F.3: Multiple linear regression results for clear nights (above inversion).

	Coefficients	Standard Error	t value	Pr(>|t|)
Intercept	0.26	0.35	0.73	0.47
T_{FA}	0.97	0.03	36.12	<2e-16 ***
Elevation	0.0002	0.0003	0.58	0.56

Table F.4: Multiple linear regression results for type A days.

	Coefficients	Standard Error	t value	Pr(>|t|)
Intercept	0.08	0.43	0.18	0.86
T_{FA}	0.92	0.04	24.57	<2e-16 ***
Elevation	-0.0006	0.0004	-1.76	0.08

Table F.5: Multiple linear regression results for type A nights.

	Coefficients	Standard Error	t value	Pr(>|t|)
Intercept	0.99	0.30	3.36	0.00115 **
T_{FA}	0.90	0.05	19.84	< 2e-16 ***
Elevation	-0.0004	0.0002	-1.71	0.09

Table F.6: Multiple linear regression results for type B days.

	Coefficients	Standard Error	t value	Pr(>|t|)
Intercept	-0.01	0.20	-0.03	0.98
T_{FA}	0.94	0.02	43.04	<2e-16 ***
Elevation	-0.0002	0.0002	-1.36	0.18

Table F.7: Multiple linear regression results for type B nights.